Bachelorarbeit

Zur Erlangung des akademischen Grades Bachelor of Science

Implementation of Spin-polarized Maximally Localized Wannier Functions Within the LAPW+LO Method

eingereicht von: Joris Holger Prinz

Gutachter/innen: Prof. Dr. Claudia Draxl

PD Dr. Denis Usvyat

Eingereicht am Institut für Physik der

Humboldt-Universität zu Berlin

am 17.03.2026

Contents

1 Introduction

Many technological challenges, from sustainable energy to advanced computing, depend on novel materials. Studying such materials requires a deep understanding of the underlying solid-state physics. A significant number of advanced materials contains heavy atoms and are thus strongly impacted by spin-orbit (SO) coupling. Others exhibit peculiar properties when exposed to magnetic fields or when internal electron spins align in specific patterns. The framework of density-functional theory (DFT) has vast success in accurately and quantitatively predicting the (opto-)electronic and mechanical properties of a wide variety of materials from first principles. The fundamental Kohn-Sham (KS) equations of DFT are often treated in reciprocal space in terms of Bloch functions, which in turn can be expanded in a basis. A combination of augmented planewaves (APWs) and local orbitals (LOs) is widely considered as a gold standard for DFT, constituting the basis employed in the LAPW+LO method [28].

Typically, a large number of basis functions is required for the expansion of Bloch orbitals, in order to approach basis completeness. This results in a high computational cost of diagonalizing the KS Hamiltonian, in particular when a dense reciprocal-space sampling is required, as each diagonalization scales with the basis size N as $\mathcal{O}(N^3)$. Additionally, the most accurate DFT calculations employ the class of hybrid exchange-correlation functionals and post-DFT corrections such as the GW method. Both contain terms that increase the computational cost to $\mathcal{O}(N^4)$. Consequently, an efficient interpolation scheme is desirable.

Wannier functions (WFs) [3] are real-space objects and an alternative Hilbert space basis to Bloch functions. WFs can be constructed from Bloch functions, and it is possible to choose them to be maximally localized by exploiting the gauge freedom of Bloch functions. For this reason (and others), maximally localized Wannier functions (MLWFs) are an ideal candidate for a tight-binding basis that can be used in the computationally efficient Slater-Koster interpolation scheme [4].

A recent implementation [34, 38] within the full-potential all-electron LAPW+LO DFT code `exciting` [28, 44] implemented the commonly employed Marzari-Vanderbilt [14] scheme for the construction of MLWFs, giving access to interpolated eigenenergies and single-particle orbitals on fine reciprocal-space grids in terms of the MLWFs. It further features an automated construction of MLWF initial guesses from LOs [43], energy disentanglement procedures [17, 35], and the calculation of diverse quantities via Wannier interpolation. However, it did not yet offer an option for constructing spin-polarized MLWFs. The Marzari-Vanderbilt scheme requires only modest additions to enable a spin-polarized treatment [27]. This work aims at extending the recent implementation to enable the construction of MLWFs from spin-polarized Bloch states within the `exciting` code.

This work begins with a sketch of the DFT method and an introduction to the LAPW+LO method. Then, it covers the treatment of SO coupling and magnetism in the `exciting` code. Next, WFs, the construction of MLWFs according to the Marzari-Vanderbilt scheme, and extensions of the latter are introduced. Subsequently, the Wannier interpolation of single-particle eigenenergies and wave functions is presented. At each conceptual step, the necessary methodological additions for the incorporation of spin-polarized MLWFs are described. In the implementation section, details of the extension of the previous Wannier implementation are covered. The application section shows tests of the performance of this implementation on two simple benchmark systems. Additionally, it is applied to a more complex system, a halide perovskite with broken inversion symmetry. For each material, different utilities of the spin-polarized MLWFs are showcased.

2 Theory and methodology

2.1 Kohn-Sham density-functional theory

One of the main goals of theoretical physics is to develop models and frameworks that explain known physical phenomena, based on assumptions compatible with experimental observations and verified by data acquired from them. A model of high accuracy allows the prediction of these properties in new, unobserved systems with minimal or no experimental input at all. Within the field of theoretical condensed-matter physics, methods of the latter type are called *ab initio* (first-principles) methods, at the core of which lies a many-body system of mutually interacting electrons and nuclei. The following sections up until Sec. 2.1.5 closely follow Chapter 15 of [36].

2.1.1 Many-body Schrödinger equation

The electronic structure of solid materials can only be understood within a quantum mechanical framework, starting from the time-independent many-body Schrödinger equation (yet neglecting electron spin):

$$\hat{H}\Psi_n(\mathbf{r}_1, \mathbf{r}_2, \ldots, \mathbf{r}_N, \mathbf{R}_1, \mathbf{R}_2, \ldots, \mathbf{R}_M) = E_n\Psi_n(\mathbf{r}_1, \mathbf{r}_2, \ldots, \mathbf{r}_N, \mathbf{R}_1, \mathbf{R}_2, \ldots, \mathbf{R}_M) \,, \tag{2.1.1}$$

where $\hat{H}$, Ψ_n, and E_n are the Hamiltonian, its n-th eigenstate (wave function) and corresponding eigenenergy and $\mathbf{r}_i$ ($\mathbf{R}_i$) are the position of the i-th of N electrons (M nuclei) within the system. The many-body Hamiltonian is (in atomic units $e = m_e = \hbar = 1$)

$$\hat{H} = -\sum_{i=1}^{N}\frac{\nabla_i^2}{2} - \sum_{l=1}^{M}\frac{\nabla_l^2}{2M_l} + \frac{1}{2}\sum_{i\neq i'}^{N}\frac{1}{|\mathbf{r}_i - \mathbf{r}_{i'}|} - \sum_{i=1}^{N}\sum_{l=1}^{M}\frac{Z_l}{|\mathbf{r}_i - \mathbf{R}_l|} + \frac{1}{2}\sum_{l\neq l'}^{N}\frac{Z_l Z_{l'}}{|\mathbf{R}_l - \mathbf{R}_{l'}|}. \tag{2.1.2}$$

M_l and Z_l are the mass and charge of the l-th nucleus, while ∇_i^2, ∇_l^2 are the Laplacians acting on electron position i and nucleus position l. This linear partial differential Schrödinger equation involves $3(N + M)$ continuous spatial coordinates and is coupled in all these degrees of freedom through the Coulomb interaction terms of electron-electron repulsion, electron-nucleus attraction, and nucleus-nucleus repulsion. With typical macroscopic systems of interest containing a total number of particles in the order of $\sim 10^{23}$, directly obtaining exact numerical solutions is generally computationally unfeasible. Thus, a number of approximations and simplifications must be introduced for solving the many-body problem.

2.1.2 Born-Oppenheimer approximation

The Born-Oppenheimer approximation assumes the positions of the nuclei $\mathbf{R}_l$ as fixed compared to the electron positions. This can be justified by the much larger masses of nuclei compared to the electron mass, resulting in a comparatively high inertia of nuclei. In consequence, the nucleus-nucleus Coulomb interaction term is reduced to a constant that is dropped (by setting the energy to zero accordingly), and the Laplacian acting on nucleus coordinates always yields zero. The wave functions $\Psi_n(\mathbf{r}, \mathbf{r}_2, \ldots, \mathbf{r}_N)$ are considered for a fixed set of the positions of nuclei $\mathbf{R}_l$ (which are therefore no longer written as arguments of the wave function). Eq. (2.1.2) is then rewritten as

$$\hat{H} = -\sum_{i=1}^{N}\frac{\nabla_i^2}{2} + \frac{1}{2}\sum_{i\neq i'}^{N}\frac{1}{|\mathbf{r}_i - \mathbf{r}_{i'}|} - \sum_{i=1}^{N}\sum_{l=1}^{M}\frac{Z_l}{|\mathbf{r}_i - \mathbf{R}_l|} = \hat{T} + \hat{U} + \hat{V}_{\text{ext}} \,, \tag{2.1.3}$$

identifying $\hat{T}$, $\hat{U}$, and $\hat{V}_{\text{ext}}$ as the kinetic energy of electrons, the electron-electron Coulomb-interaction, and the external potential due to nuclei experienced by individual electrons, respectively. This reduces the many-body problem degrees of freedom to $3N$.

2.1.3 Density-functional theory

In order to further reduce the problem size, the framework of density-functional theory (DFT) has been widely employed. DFT-based methods offer a good balance between physical accuracy and computational efficiency. At the core, DFT methods are based on the electron density

$$n(\mathbf{r}) = N \int \mathrm{d}\mathbf{r}_2 \ldots \mathrm{d}\mathbf{r}_N \, |\Psi_n(\mathbf{r}, \mathbf{r}_2, \ldots, \mathbf{r}_N)|^2 \, . \tag{2.1.4}$$

The ground state electron density can be regarded as the fundamental quantity of a many-electron system's ground state, and it will further make the problem tractable due to two theorems provided by Hohenberg and Kohn [7]: The first theorem (HK1) states, that the external potential $\hat{V}_{\text{ext}}$ is uniquely (up to an additive constant) determined by the ground state electron density $n_0(\mathbf{r})$, which is a function of only three spatial coordinates. It defines an energy functional of the electron density, given an external potential $\hat{V}_{\text{ext}}$ with $\langle \Psi[n] \,|\, \hat{V}_{\text{ext}} \,|\, \Psi[n] \rangle = \int \mathrm{d}\mathbf{r} v_{\text{ext}}(\mathbf{r}) n(\mathbf{r})$:

$$E[n] = \langle \Psi[n] \,|\, \hat{T} + \hat{U} \,|\, \Psi[n] \rangle + \int \mathrm{d}\mathbf{r} \, v_{\text{ext}}(\mathbf{r}) n(\mathbf{r}) \, . \tag{2.1.5}$$

HK2 then proves that the true ground state electron density $n_0(\mathbf{r})$ corresponding to $\hat{V}_{\text{ext}}$ minimizes this energy functional, assuming such a corresponding electron density exists in the first place. The fact that $\hat{V}_{\text{ext}}$ is determined uniquely by the ground state electron density is equivalent to saying that the Hamiltonian and hence the corresponding wave functions and eigenenergies are a functional of the electron density, since $\hat{T}$ and $\hat{U}$ are universal for any system containing N electrons. In consequence, the expectation value of any observable could be calculated if a method for calculating the energy functional Eq. (2.1.5) and a strategy for its minimization are established.

2.1.4 Kohn-Sham equations

Kohn and Sham (KS) proposed to rewrite the energy functional as

$$E[n] = \langle \Psi_S[n] \,|\, T \,|\, \Psi_S[n] \rangle + E_H[n] + \langle \Psi_S[n] \,|\, \hat{V}_{\text{ext}} \,|\, \Psi_S[n] \rangle + E_{xc}[n] \, . \tag{2.1.6}$$

This energy functional is the result of calculating the expectation value of the Hamiltonian with an ansatz for the full many-body wave function as a single Slater determinant $|\Psi_s[n]\rangle$ of non-interacting electron orbitals. These N single-particle KS orbitals $\phi_i(\mathbf{r})$ correspond to an electron density

$$n(\mathbf{r}) = \sum_i f_i |\phi_i(\mathbf{r})|^2 . \tag{2.1.7}$$

f_i is the occupation number of single-particle electron orbital $\phi_i(\mathbf{r})$ and takes values between 0 or 1 if the spin is considered. When spin is not treated explicitly, values between 0 and 2 are possible. Integer numbers correspond to unoccupied or fully occupied orbitals, while fractional values represent partially occupied states. In each case, the occupation numbers sum up to the total number of electrons N, and only occupied (or partially occupied) states contribute to the electron density.

$$E_H[n] = \frac{1}{2} \int \mathrm{d}\mathbf{r} \int \mathrm{d}\mathbf{r}' \, n(\mathbf{r}) \frac{n(\mathbf{r}')}{|\mathbf{r} - \mathbf{r}'|} \tag{2.1.8}$$

is the *Hartree* contribution to the Coulomb interaction energy, representing the analog to the classical Coulomb interaction (compared to the full $\langle \Psi[n] \,|\, \hat{U} \,|\, \Psi[n] \rangle$), which omits the quantum-mechanical electron exchange and correlation interactions.

The approach Kohn and Sham proposed, is to determine the ground state electron density $n_0(\mathbf{r})$ of the system of interacting electrons with the energy functional in Eq. (2.1.6), which contains

only expectation values in terms of a Slater determinant of non-interacting electron orbitals, and an *exchange-correlation energy functional* of the electron density $E_{xc}[n]$. Every contribution to the energy functional of the fully interacting system (Eq. (2.1.5)) missing from the first three terms in Eq. (2.1.6) is incorporated into $E_{xc}[n]$. Through the introduction of $E_{xc}[n]$, without loss of generality, no approximations have been made up to this point in the KS energy functional Eq. (2.1.6), compared to a treatment of the true interacting system with $\Psi(\mathbf{r})$ in Eq. (2.1.5). Exact expressions for the first three terms of Eq. (2.1.6) are available, such that the whole complexity of the many-electron problem is then contained in the exchange-correlation functional $E_{xc}[n]$.

The form of the one "true" exchange-correlation functional is unknown, so it has to be approximated, which is a challenging task due to its generality. A wide variety of increasingly accurate and complex approximations to the true unknown exchange-correlation functional $E_{xc}[n(\mathbf{r})]$ have been proposed in order to achieve so-called "chemical accuracy", which can be categorized according to the "Jacobs ladder" of density-functional theory [16]. These approximations are not further discussed within this work.

The strategy for obtaining the system's ground state is a minimization of the KS energy functional Eq. (2.1.6) with respect to the electron density $n(\mathbf{r})$ by variation, including a Lagrange multiplier to enforce particle conservation. This variation of the energy functional results in the KS equations [8]:

$$\underbrace{\left[-\frac{\nabla^2}{2} + v_{\mathrm{KS}}(\mathbf{r})\right]}_{\equiv \hat{h}_{\mathrm{KS}}} \phi_i(\mathbf{r}) = \epsilon_i \phi_i(\mathbf{r}), \tag{2.1.9}$$

defining the KS Hamiltonian $\hat{h}_{\mathrm{KS}}$ (which acts on non-interacting single-particle orbitals), wherein the KS potential is $v_{\mathrm{KS}}(\mathbf{r})$:

$$v_{\mathrm{KS}}(\mathbf{r}) = v_H(\mathbf{r}) + v_{\mathrm{ext}}(\mathbf{r}) + v_{xc}[n(\mathbf{r})] \,, \tag{2.1.10}$$

with

$$\begin{aligned} v_H(\mathbf{r}) &= \int \mathrm{d}\mathbf{r}' \, \frac{n(\mathbf{r}')}{|\mathbf{r} - \mathbf{r}'|} \,, \\ v_{xc}[n(\mathbf{r})] &= \frac{\delta E_{xc}[n(\mathbf{r})]}{\delta n(\mathbf{r})} \,, \end{aligned} \tag{2.1.11}$$

and $v_{\mathrm{ext}}(\mathbf{r})$ defined by

$$\langle \Psi_S[n] \,|\, \hat{V}_{\mathrm{ext}} \,|\, \Psi_S[n] \rangle = \int \mathrm{d}\mathbf{r} v_{\mathrm{ext}}(\mathbf{r}) n(\mathbf{r}) \,. \tag{2.1.12}$$

Here $v_H(\mathbf{r})$ denotes the Hartree-potential, $v_{xc}[n(\mathbf{r})]$ is called the exchange-correlation potential and v_{ext} the external potential. Eq. (2.1.9) takes the form of a single-particle Schrödinger-like equation. The many-electron problem complexity is then reduced to solving the KS equations for a set of N single-particle orbitals $\phi_i(\mathbf{r})$ with Lagrange multipliers ϵ_i, the former constituting the ground state electron density. These $\phi_i(\mathbf{r})$ and ϵ_i appear as eigenfuctions and eigenvalues to the KS Hamiltonian $\hat{h}_{\mathrm{KS}}$, repectively, in Eq. (2.1.9). Since, however, the KS potential depends on the density, which in turn depends on the $\phi_i(\mathbf{r})$, the set of N equations has to be solved iteratively. Starting from an initial guess for the density, the set of KS equations is solved, and the density is recalculated with the obtained KS orbitals $\phi_i(\mathbf{r})$ (or updated according to a mixing of $n^{\mathrm{in}}(\mathbf{r})$ and $n^{\mathrm{out}}(\mathbf{r})$). The latter two steps are repeated until the differences between consecutive densities vanish. This strategy is called the *self-consistent-field* (SCF) method. It can be refined in order

to improve convergence behavior.

As a last note, the interpretation of the single-particle orbitals $\phi_i(\mathbf{r})$ and corresponding Lagrange multipliers ϵ_i as wave functions and eigenenergies appears intuitive, but needs to be taken with a grain of salt ([36], Chapter 15 p. 391). They are merely auxiliary variables and have no immediate physical meaning. The only fundamental quantity in DFT is the electron density built from the Kohn-Sham (KS) orbitals. Nonetheless, in this work, the $\phi_i(\mathbf{r})$ and ϵ_i are interpreted as wave functions and eigenenergies. Therefore, from now on, the former are written as $\psi_i(\mathbf{r})$.

2.1.5 Bloch's theorem and periodic boundary conditions

Before proceeding, the concept of the *unit cell* and *Brillouin zone* (BZ) shall be introduced. Assuming a periodic crystal structure, the whole crystal volume can be regarded as a number of identical repeating *unit cells*. Choosing three basis vectors of the crystal lattice $(\mathbf{a}_1, \mathbf{a}_2, \mathbf{a}_3)$, every real space lattice vector $\mathbf{R}$ pointing to a unit cell is expressed as $\mathbf{R} = n_1\mathbf{a}_1 + n_2\mathbf{a}_2 + n_3\mathbf{a}_3$, with $n_1, n_2, n_2 \in \mathbb{Z}$. The parallelepiped spanned by real space lattice basis vectors is called the unit cell with a volume of $V_u = |\mathbf{a}_1 \cdot (\mathbf{a}_2 \times \mathbf{a}_3)|$. The *reciprocal space* is the dual space to the real space and contains reciprocal space vectors $\mathbf{k}$. In analogy to the real space equivalents, the reciprocal lattice basis vectors $(\mathbf{b}_1, \mathbf{b}_2, \mathbf{b}_3)$ are defined by $\mathbf{a}_j \cdot \mathbf{b}_i = 2\pi\delta_{ij}$, and reciprocal lattice vectors as $\mathbf{G} = m_1\mathbf{b}_1 + m_2\mathbf{b}_2 + m_3\mathbf{b}_3$ with $m_1, m_2, m_3 \in \mathbb{Z}$ fulfilling $\mathbf{G} \cdot \mathbf{R} = 2\pi n$ with $n \in \mathbb{Z}$. The equivalent to the specific Wigner-Seitz unit cell in reciprocal space is the first BZ [36], which is referred to as just BZ in this work.

When a single electron is moving in a potential due to nuclei arranged in a periodic crystal structure, then $\hat{V}_{\text{ext}}(\mathbf{r}) = \hat{V}_{\text{ext}}(\mathbf{r}+\mathbf{R})$, with a lattice vector $\mathbf{R}$. As a consequence, the Hamiltonian is invariant under a translation with a lattice vector $\mathbf{R}$ [36]. In this work, the external potential and hence the Hamiltonian of all materials are assumed to exhibit this cell-periodicity. Bloch's theorem states, that in this case the electron wave functions take the form $\psi_{\mathbf{k}}(\mathbf{r}) = e^{i\mathbf{k}\cdot\mathbf{r}}u_{\mathbf{k}}(\mathbf{r})$ with a cell-periodic function $u_{\mathbf{k}}(\mathbf{r}) = u_{\mathbf{k}}(\mathbf{r}+\mathbf{R})$ and a reciprocal space vector $\mathbf{k}$. As a consequence, $\psi_{\mathbf{k}+\mathbf{G}}(\mathbf{r})$ is an equally valid wave function, as can be seen when expanding the cell-periodic part as $u_{\mathbf{k}}(\mathbf{r}) = \sum_{\mathbf{G}} a_{\mathbf{G}}(\mathbf{k})e^{i\mathbf{G}\cdot\mathbf{r}}$ [36]. Therefore, restricting reciprocal space vectors $\mathbf{k}$ to the first BZ is sufficient. Further, from Bloch's theorem follows:

$$\psi_{\mathbf{k}}(\mathbf{r}+\mathbf{R}) = e^{i\mathbf{k}\cdot\mathbf{R}}\psi_{\mathbf{k}}(\mathbf{r}) \,, \tag{2.1.13}$$

and

$$\langle\psi_{\mathbf{k}} \,|\, \psi_{\mathbf{k}'}\rangle^{\mathbb{R}^3} = \delta(\mathbf{k}-\mathbf{k}') \,, \tag{2.1.14}$$

which holds when $\mathbf{k}$,$\mathbf{k}'$ are within the first BZ. The superscript $^{\mathbb{R}^3}$ indicates an integration on the domain of $\mathbb{R}^3$. Naturally, within KS DFT, single particle orbitals represent non-interacting electrons, and a cell-periodic potential is assumed. Hence, they are Bloch functions.

For practical numerical calculations, the BZ is sampled by a discrete $N_1 \times N_2 \times N_3$ grid, comprising a number of $N_{\mathbf{k}} = N_1N_2N_3$ points $\mathbf{k}$ in reciprocal space. These BZs are repeated periodically to imitate the full infinite system, according to Born-von-Kármán (BvK) boundary conditions [1, 2]. Under these conditions $\mathbf{k}$ appears as a natural quantum number, and thus single-particle wave functions are denoted by $\psi_{i\mathbf{k}}(\mathbf{r})$, with associated eigenenergies $\epsilon_{i\mathbf{k}}$. Mathematically, the discrete BZ sampling is equivalent to simulating the real-space crystal volume by repeating BvK *supercells* (SCs) comprising $N_1 \times N_2 \times N_3$ unit cells. The `exciting` code does not consider an SC explicitly in real-space integrals and instead calculates them as a sum over discrete $\mathbf{k}$-points of integrals on the domain of the unit-cell. However, the concept of the SC becomes relevant for Wannier functions, since they are real-space objects. In this work, Bloch states are normalized within one unit cell

when employing BvK boundary conditions. From this follows $\langle m\mathbf{k} \,|\, n\mathbf{k}'\rangle^{\mathrm{SC}} = N_{\mathbf{k}}\delta_{mn}\delta_{\mathbf{k},\mathbf{k}'}$, where the superscript $^{\mathrm{SC}}$ indicates the integration domain to be the BvK SC volume.

2.1.6 Basis expansion of Kohn-Sham orbitals

With the simplifications introduced in the previous sections, the approach for solving the many-body problem with a specific material in scope reduces to solving the partial differential KS equations Eq. (2.1.9) self-consistently and thus to finding a set of single-particle orbitals $\psi_{i\mathbf{k}}(\mathbf{r})$ as eigenfunctions to $\hat{h}_{\mathrm{KS}}$ and corresponding eigenvalues $\epsilon_{i\mathbf{k}}$ that result in the ground state density $n_0(\mathbf{r})$. Instead of solving the differential equation directly, it can be convenient to expand the KS wave functions in a basis $\{\varphi_{\kappa\mathbf{k}}(\mathbf{r})\}$ like

$$\psi_{i\mathbf{k}}(\mathbf{r}) = \sum_{\kappa}^{N_B} C^{\mathbf{k}}_{\kappa i}\varphi_{\kappa\mathbf{k}}(\mathbf{r}) \,, \tag{2.1.15}$$

with expansion coefficients $C^{\mathbf{k}}_{\kappa i}$ and a number of N_B basis functions $\varphi_{\kappa\mathbf{k}}(\mathbf{r})$. The expansion coefficients have dimension $(N_B \times N_{\mathrm{KS}})$, at every point in reciprocal space $\mathbf{k}$, where N_{KS} is the number of KS orbitals to calculate, with $N_{\mathrm{KS}} \leq N_B$. Substituting this expansion for wave functions in the KS equations Eq. (2.1.9) and applying basis functions $\langle\varphi_{\kappa'\mathbf{k}}|$ from the left results in the *secular equation*:

$$\begin{aligned} \langle\varphi_{\kappa'\mathbf{k}} \,|\, \hat{h}_{\mathrm{KS}} \,|\, \varphi_{\kappa\mathbf{k}}\rangle C^{\mathbf{k}}_{\kappa i} &= \epsilon_{i\mathbf{k}}\langle\varphi_{\kappa'\mathbf{k}} \,|\, \varphi_{\kappa\mathbf{k}}\rangle C^{\mathbf{k}}_{\kappa i} \\ \Leftrightarrow H^{\mathbf{k}}C^{\mathbf{k}}_i &= \epsilon^{\mathbf{k}}_i S^{\mathbf{k}} C^{\mathbf{k}}_i \,, \end{aligned} \tag{2.1.16}$$

with KS Hamiltonian matrix elements $H^{\mathbf{k}}_{\kappa'\kappa} = \langle\varphi_{\kappa'\mathbf{k}} \,|\, \hat{h}_{\mathrm{KS}} \,|\, \varphi_{\kappa\mathbf{k}}\rangle$ of dimension $(N_B \times N_B)$ in the basis of the $|\varphi_{\kappa\mathbf{k}}\rangle$ and the $(N_B \times N_B)$ basis overlap matrix $S^{\mathbf{k}}_{\kappa'\kappa} \equiv \langle\varphi_{k'\mathbf{k}} \,|\, \varphi_{\kappa\mathbf{k}}\rangle$. Eq. (2.1.16) takes the form of a generalized eigenvalue problem for every column of $C^{\mathbf{k}}$. Therefore, $C^{\mathbf{k}}$ is also called the eigenvector matrix within the scope of this work. Therefore, by choosing a basis $\{\varphi_{\kappa\mathbf{k}}(\mathbf{r})\}$, the partial differential KS equations Eq. (2.1.9) are transformed to a linear algebra problem, which can be efficiently solved numerically with dense linear algebra routines at the cost of $\mathcal{O}(N_B^3)$[1] for every diagonalization of $H^{\mathbf{k}}$ at every $\mathbf{k}$-point for every SCF-iteration.

2.1.7 The LAPW+LO method

One particularly useful basis for expanding the KS orbitals is a combination of augmented planewaves (APWs) and local orbitals (LOs). This basis combination is employed in the linearized augmented planewave (LAPW+LO) method, which is treated within this work and utilized by the full-potential all-electron DFT code `exciting` [28, 44]. Due to their high accuracy in solving the KS equations, methods based on the combined basis of APWs and LOs are widely considered as the gold standard of DFT for extended systems [28]. A brief introduction is given here, while further details are discussed in [28].

For the introduction of the basis functions, the unit cell is partitioned into interstitial region (IR) and muffin-tin (MT) regions, the latter being non-overlapping spheres of radii $R_{\mathrm{MT},\alpha}$ centered around an atom α at position $\mathbf{R}_\alpha$. APWs take planewave form in the IR and are smoothly continued to a spherical harmonics expansion of solutions to the radial KS equations inside the MT spheres, by matching a number of l-channels. Like APWs, LOs are atomic-like in MTs but strictly zero outside, and they are chosen for specific orbital quantum number combinations (l, m) only,

[1] This is the cost for a full diagonalization of the Hamiltonian. In practice, one wants to retrieve only a total number N_{KS} eigenstates, including all occupied states and optionally a limited number of empty states. Usually $N_{\mathrm{KS}} \ll N_{\mathrm{B}}$, and iterative eigensolvers allow for retrieving only a number of N_{KS} eigenstates at lower cost than $\mathcal{O}(N_B^3)$.

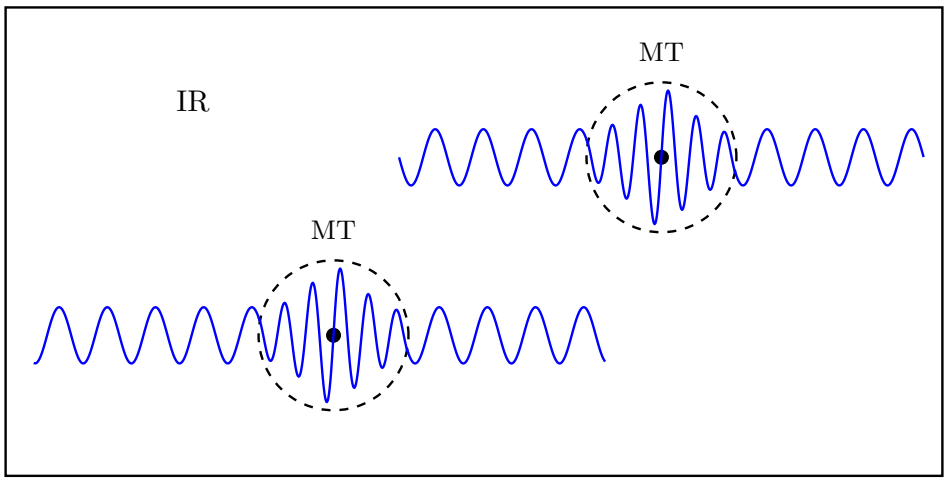

Figure 1: Illustration of the unit cell partitioning employed by the LAPW+LO method. Basis functions are planewaves in the IR. MT spheres are centered around atoms. At the MT sphere boundaries, the planewaves are continued to atomic-like & rapidly oscillating functions. Additional local orbitals can be added inside the MT spheres.

while being associated to specific atoms α. The space partitioning and basis functions employed in the LAPW+LO method are illustrated in Fig. 1.

The APW basis functions utilized in the LAPW framework are defined as

$$\varphi_{\mathbf{G}+\mathbf{k}}(\mathbf{r}) = \begin{cases} \sum_{lm} \sum_{\xi} \left[A_{lm\alpha}^{\xi,\mathbf{G}+\mathbf{k}} u_{l\alpha}^{\xi}(r_\alpha; \epsilon_{l\alpha}) \right] Y_{lm}(\mathbf{r}_\alpha), & r_\alpha \leq R_{\mathrm{MT}} \\ \frac{1}{\sqrt{V_u}} e^{i(\mathbf{G}+\mathbf{k})\cdot\mathbf{r}}, & \mathbf{r} \in \mathrm{IR}\,. \end{cases} \tag{2.1.17}$$

The radial functions $u_{l\alpha}(r_\alpha; \epsilon)$ satisfy the radial Schrödinger equation, which, in principle, depends on the eigenenergies $\epsilon_{i\mathbf{k}}$. This fact results in the KS equations becoming nonlinear. To navigate this problem, radial energies are fixed as parameters to chosen values $\epsilon_{l\alpha}$, such that radial functions are approximated as $u_{l\alpha}(r_\alpha; \epsilon) \approx u_{l\alpha}(r_\alpha; \epsilon_{l\alpha})$. In order to improve upon this approximation, the ξ-th radial function energy derivatives $u_{l\alpha}^{\xi}(r_\alpha; \epsilon_{l\alpha}) = \partial^\xi / \partial \epsilon^\xi u(r_\alpha; \epsilon)\big|_{\epsilon=\epsilon_l}$ can be added, in the spirit of a Taylor-like expansion of radial functions around $\epsilon_{l\alpha}$. It can be shown that in this way, the linearization error induced by fixing radial energies $\epsilon_{l\alpha}$ is reduced to $\mathcal{O}(\epsilon - \epsilon_{l\alpha})^2$ and $\mathcal{O}(\epsilon - \epsilon_{l\alpha})^4$ for band energies and the total energy, respectively [28]. Matching coefficients $A_{lm\alpha}^{\xi,\mathbf{G}+\mathbf{k}}$ to radial functions of order ξ ensure a matching per l-channel to a spherical harmonics expansion of the planewaves in the IR at the MT-boundaries, with explicit expressions available. The spherical harmonics are labeled as $Y_{lm}(\mathbf{r}_\alpha)$. Further $\mathbf{r}_\alpha = \mathbf{r} - \mathbf{R}_\alpha$ and $r_\alpha = |\mathbf{r}_\alpha|$.

Local orbitals are defined by

$$\varphi_L(\mathbf{r}) = \begin{cases} \sum_{\xi} \delta_{\alpha\alpha_L} \delta_{ll_L} \delta_{mm_L} a_L^{\xi} u_{l\alpha}^{\xi}(r_\alpha; \epsilon_{l\alpha}) Y_{lm}(\mathbf{r}_\alpha), & r_\alpha \leq R_{\mathrm{MT}} \\ 0, & \mathbf{r} \in \mathrm{IR}\,, \end{cases} \tag{2.1.18}$$

with coefficients a_L^{ξ} ensuring $\varphi_L(\mathbf{r}) = 0$ at the MT boundaries and $\int_{\Omega_u} \mathrm{d}\mathbf{r} |\varphi_L(\mathbf{r})|^2 = 1$. A LO is non-vanishing only in the MT around atom α and zero elsewhere. LOs need to be optionally and manually chosen in quantum numbers l, m per atom species. Linearization energies $\epsilon_{l\alpha}$ and radial derivative orders ξ can be different from the LAPW choices, and all kinds of parameter choices can be combined. LOs offer a different approach to tackle the problem of linearizing the radial Schrödinger equation, while additionally providing more flexibility for the description of wave functions inside the MT spheres.

The specific basis combination introduced here will be called the LAPW+LO basis in the scope of this work. KS wave functions are expanded in the LAPW+LO basis as

$$\begin{aligned}\psi_{i\mathbf{k}}(\mathbf{r}) &= \sum_{\mathbf{G}} C^{\mathbf{k}}_{\mathbf{G}i}\varphi_{\mathbf{G}+\mathbf{k}}(\mathbf{r}) + \sum_{L} C^{\mathbf{k}}_{Li}\varphi_{L}(\mathbf{r}) \\ &\equiv \sum_{\kappa} C^{\mathbf{k}}_{\kappa i}\varphi_{\kappa\mathbf{k}}(\mathbf{r}) \ ,\end{aligned} \tag{2.1.19}$$

with LAPW expansion coefficients $C^{\mathbf{k}}_{\mathbf{G}i}$ and LO expansion coefficients $C^{\mathbf{k}}_{Li}$. For later purposes, it is convenient to define a combined index $\{\kappa\} = \{\mathbf{G}\} \cup \{L\}$, with

$$\varphi_{\kappa\mathbf{k}}(\mathbf{r}) = \begin{cases} \varphi_{\mathbf{G}+\mathbf{k}}(\mathbf{r}) & \kappa \in \{\mathbf{G}\} \\ \varphi_{L}(\mathbf{r}) & \kappa \in \{L\} \ , \end{cases} \tag{2.1.20}$$

at every point $\mathbf{k}$ individually. For practical calculations, a maximum vector of $\mathbf{G}_{\max}$ is chosen, truncating the sum $\sum_{\mathbf{G}}$, therefore turning the basis incomplete. Including enough basis functions allows to approach a complete basis. With the LAPW+LO basis expansion, the KS equations are transformed into a generalized eigenvalue problem of size $N_{\text{LAPW+LO}} = N_{\mathbf{G}+\mathbf{k}} + N_L$[2] according to Eq. (2.1.16). The overlap matrix $S^{\mathbf{k}}$ is not diagonal, since the LAPW+LO basis functions are not orthogonal. Finally, after specifying a basis, all ingredients for computationally solving the many-electron problem are provided.

As a last note, it should be mentioned that KS orbitals can be classified by their degree of localization around the atom cores. Core states are assumed to be strictly zero outside the MT regions and treated separately, i.e., not included in the KS Hamiltonian in `exciting`. Instead, their wave functions are obtained by numerically solving the Dirac equation in the MT spheres with a spherically averaged KS potential at every SCF step. Importantly, they still contribute to the total electron density. Semi-core states have only little contributions outside the MT regions and are treated with the LAPW+LO basis expansion, just as valence states. In practice, the introduction of LOs is necessary to accurately treat semi-core states in the same Hamiltonian as the valence states [28].

2.1.8 The second variation method

Thus far, the KS Hamiltonian has not explicitly considered the electron spin, and the KS equations have been solved with the LAPW+LO basis described in the previous section. In this formulation, the KS Hamiltonian is invariant under global SU(2) rotations of the electron spin, implying $[\hat{h}_{\text{KS}}, \hat{s}] = 0$, where the single-electron spin operator is $\hat{s} = \hbar/2\,\boldsymbol{\sigma}$ and the vector of Pauli matrices is denoted as $\boldsymbol{\sigma} = (\sigma_x, \sigma_y, \sigma_z)$. In this case, every state is two-fold spin-degenerate. This symmetry is, however, broken when considering different physical effects [36]: (i) breaking of spin symmetry through exchange effects, enabling a lower the total energy, (ii) an external magnetic field, or (iii) the effect of spin-orbit (SO) coupling. The following two sections cover the consideration of these three effects in the `exciting` code.

The rigorous treatment of the electron spin and magnetic effects requires the setup of a KS-DFT framework starting from the full Dirac equation [26]. This comes at a higher computational cost, since operators in a Dirac framework become 4×4 shaped, while single-particle wave functions are then 4-spinors. Further, a generalization of the HK-theorems to the full relativistic case is possible (*current density-functional theory* [25], Chapter 2.6), but includes the 4-current $j^{\mu}(\mathbf{r}) = (cn(\mathbf{r}), \mathbf{j}(\mathbf{r}))$ (with the speed of light c and current density $\mathbf{j}(\mathbf{r})$) that now uniquely determines an

[2] More precisely, in `exciting`, the LAPW+LO basis size is $\mathbf{k}$-dependent. See [28].

external 4-potential $A^{\mu}(\mathbf{r})$ up to a gauge transformation [26].

For practical purposes, the `exciting` code employs the *second-variation* (SV) method ([12], Chapter 5.14), to treat magnetic and spin-orbit (SO) effects. This section presents the spin-treatment in `exciting` according to [28]. Within the SV method, simplifications to the Dirac equations are applied by considering the non-relativistic limit. The Hamiltonian operator dimension is reduced to 2×2 by disregarding the Dirac 4-spinor minor components [11]. Moreover, in `exciting`, orbital magnetic effects are neglected, which originate from rigorous inclusion of the 4-potential (specifically through the vector potential $\mathbf{A}(\mathbf{r})$) and couple to the electron angular momentum. Further, instead of determining the system's ground state via the 4-current, the HK theorems are generalized to encompass the electron density $n(\mathbf{r})$ and additionally parts of the magnetization vector $\mathbf{m}(\mathbf{r})$ (see section Sec. 2.1.9), within the scope of *spin density-functional theory* ([25], Chapter 2.5).

Generally, a first-principles calculation applying the SV method is divided into two steps. In the first variation (FV) step, the KS Hamiltonian or a scalar-relativistic (SR) zero-order regular approximation (ZORA) approximation to the Dirac Hamiltonian excluding SO coupling/magnetism is treated within the LAPW+LO basis (for the case of `exciting`). In the second step, called SV-step, magnetic and/or SO-coupling effects are included into the Hamiltonian [41] like:

$$\hat{h}^{\mathrm{SV}}_{\sigma\sigma'} = \hat{h}^{\mathrm{FV}}\delta_{\sigma\sigma'} + [\hat{h}_B + \hat{h}^{\mathrm{ZORA}}_{\mathrm{SO}}]_{\sigma\sigma'}\,, \tag{2.1.21}$$

where $\sigma \in \{\alpha,\beta\}$ is the 2-spinor index. The full 2×2 SV Hamiltonian is denoted as $\hat{h}^{\mathrm{SV}}$, the diagonal non-relativistic KS or ZORA-SR KS Hamiltonian as $\hat{h}^{\mathrm{FV}}$, and the magnetic (ZORA-SO) contribution as $\hat{h}_B$ ($\hat{h}^{\mathrm{ZORA}}_{\mathrm{SO}}$), respectively. The magnetic Hamiltonian contribution is defined by

$$\hat{h}_B = g_e\frac{\alpha}{4}\boldsymbol{\sigma}\cdot[\mathbf{B}_{\mathrm{ext}}(\mathbf{r}) + \mathbf{B}_{\mathrm{FSM}}(\mathbf{r}) + \mathbf{b}_{\mathrm{xc}}(\mathbf{r})] \tag{2.1.22}$$

and takes the form of a Zeeman coupling term (compare [36], Chapter 17.3). The quantity $\mathbf{B}_{\mathrm{ext}}(\mathbf{r})$ denotes an external magnetic field, $\mathbf{B}_{\mathrm{FSM}}(\mathbf{r})$ a magnetic field used in the fixed spin moment method [12], and $\mathbf{b}_{\mathrm{xc}}(\mathbf{r}) = -\delta E_{\mathrm{xc}}/\delta\mathbf{m}(\mathbf{r})$ the magnetic exchange-correlation field electron interaction term. The fine-structure constant is denoted by α, and g_e denotes the electron g-factor.

The SO Hamiltonian used in `exciting` is defined by

$$\hat{h}^{\mathrm{ZORA}}_{\mathrm{SO}} = \frac{\alpha^2}{(2-\alpha^2 v_0(r))^2}\frac{1}{r}\frac{\partial v_0(r)}{\partial r}\boldsymbol{\sigma}\cdot\hat{\boldsymbol{L}}\,, \tag{2.1.23}$$

where $v_0(r)$ is the spherically averaged KS potential and $\hat{\boldsymbol{L}}$ is the orbital angular momentum operator. $\hat{h}^{\mathrm{ZORA}}_{\mathrm{SO}}$ is a ZORA approximation to the full SO-term. Through the existence of $\boldsymbol{\sigma}$ in both the magnetic and SO-term, the coupling of magnetic fields and the angular momentum operator to the electron spin is evident. Through $\hat{h}_B$ and $\hat{h}^{\mathrm{ZORA}}_{\mathrm{SO}}$ the 2×2-Pauli matrices are introduced into the SV Hamiltonian. Thus, $\hat{h}^{\mathrm{SV}}$ has to be treated with a two-component, spinor-valued wave function. Let these SV-wave functions be defined as spinors

$$\widetilde{\psi}_{n\mathbf{k}}(\mathbf{r}) = \sum_{\sigma=\alpha,\beta}\widetilde{\psi}_{n\mathbf{k}\sigma}(\mathbf{r})|\sigma\rangle\,, \tag{2.1.24}$$

with $\widetilde{\psi}_{n\mathbf{k}}(\mathbf{r})$ a SV-spinor wave function and $\widetilde{\psi}_{n\mathbf{k}\sigma}(\mathbf{r})|\sigma\rangle$ a spinor component. Throughout this work, SV quantities are denoted with a tilde as opposed to FV quantities without a tilde, when it needs to be emphasized that they result from a SV calculation. Applying $\hat{h}^{\mathrm{SV}}$ to SV wave functions

results in the SV Schrödinger equation

$$\sum_{\sigma'=\alpha,\beta} \hat{h}^{\mathrm{SV}}_{\sigma\sigma'} \widetilde{\psi}_{n\mathbf{k}\sigma'}(\mathbf{r}) = \widetilde{\epsilon}_{n\boldsymbol{k}} \widetilde{\psi}_{n\mathbf{k}\sigma}(\mathbf{r})\,. \tag{2.1.25}$$

For solving this equation, a set of spinor component basis functions needs to be specified. Selecting a number $1 \dots N_s$ of FV-orbitals $\psi_{m\mathbf{k}}(\mathbf{r})$ and expanding both SV wave function spinor components in a basis of these as

$$\widetilde{\psi}_{n\mathbf{k}\sigma}(\mathbf{r}) \equiv \sum_{m}^{N_s} \widetilde{C}^{\sigma\mathbf{k}}_{mn} \psi_{m\mathbf{k}}(\mathbf{r})\,, \tag{2.1.26}$$

with SV-expansion coefficients $\widetilde{C}^{\sigma\mathbf{k}}$, is a suitable approach for diagonalizing the SV-Hamiltonian (Eq. (2.1.21)) when magnetic and SO effects are small compared to the other Hamiltonian contributions [12]. In order to converge quantities calculated from an SV calculation (including the total energy for determining the ground state density), a number $N^{\mathrm{FV}}_{\mathrm{unocc}}$ of unoccupied orbitals has to be included in the basis set of FV orbitals, such that $N_s = N^{\mathrm{FV}}_{\mathrm{occ}} + N^{\mathrm{FV}}_{\mathrm{unocc}}$.

The SV approach reduces the SV problem size significantly: If LAPW+LO basis functions were again chosen as spinor component basis functions, one would need to diagonalize a Hamiltonian matrix H^{SV} of size $(2N_{\mathrm{LAPW+LO}} \times 2N_{\mathrm{LAPW+LO}})$, with $N_{\mathrm{LAPW+LO}}$ a significantly higher number of LAPW+LO basis functions compared to N_s. When employing FV-orbitals, the SV-Hamiltonian size reduces to $(2N_s \times 2N_s)$. This greatly impacts the overall computation time, since the diagonalization of square matrices scales as $\mathcal{O}(N^3)$ with problem size N. Further, the FV states provide an orthogonal basis for the SV states. Expressing SV wave functions in the SV Schrödinger equation Eq. (2.1.25) with the expansion given by Eq. (2.1.24) and Eq. (2.1.26), and applying FV KS orbitals $\langle\psi_{j\mathbf{k}}|$ from the left leads to the SV secular equation [41]:

$$\sum_{\sigma' j'} H^{\mathbf{k},\mathrm{SV}}_{\sigma\sigma' jj'} \widetilde{C}^{\sigma'\mathbf{k}}_{j'i} = \widetilde{\epsilon}_{i\mathbf{k}} \widetilde{C}^{\sigma\mathbf{k}}_{ji}. \tag{2.1.27}$$

From this equation, SV expansion coefficients $\widetilde{C}^{\sigma\mathbf{k}}$ are calculated, yielding spinor-valued SV wave functions and SV eigenenergies. The matrix elements $H^{\mathbf{k},\mathrm{SV}}_{\sigma\sigma'}$ are calculated as [41]:

$$\begin{aligned} H^{\mathbf{k},\mathrm{SV}}_{\sigma\sigma' jj'} &= \langle\psi_{j\mathbf{k}}\,|\,\hat{h}_{\sigma\sigma'}\,|\,\psi_{j'\mathbf{k}}\rangle \\ &= \delta_{\sigma\sigma'}\delta_{jj'}\epsilon_{j\mathbf{k}} + \langle\psi_{j\mathbf{k}}\,|\,(\hat{h}_B + \hat{h}^{\mathrm{ZORA}}_{\mathrm{SO}})_{\sigma\sigma'}\,|\,\psi_{j'\mathbf{k}}\rangle\,, \end{aligned} \tag{2.1.28}$$

wherein the calculation of the second term is straightforward by a re-expansion of FV states $\psi_{n\mathbf{k}}(\mathbf{r})$ into the LAPW+LO basis.

2.1.9 Collinear and non-collinear treatment of the electron spin

Within spin density-functional theory, the HK theorems are extended to incorporate different parts of the magnetization

$$\mathbf{m}(\mathbf{r}) = \frac{1}{N_{\mathbf{k}}} \sum_{i} \sum_{\mathbf{k}} f_{i\mathbf{k}} \widetilde{\psi}^{\dagger}_{i\mathbf{k}}(\mathbf{r}) \boldsymbol{\sigma} \widetilde{\psi}_{i\mathbf{k}}(\mathbf{r})\,, \tag{2.1.29}$$

in addition to the electron density for a spinor KS orbital

$$n(\mathbf{r}) = \frac{1}{N_{\mathbf{k}}} \sum_{i} \sum_{\mathbf{k}} f_{i\mathbf{k}} \widetilde{\psi}^{\dagger}_{i\mathbf{k}}(\mathbf{r}) \widetilde{\psi}_{i\mathbf{k}}(\mathbf{r})\,. \tag{2.1.30}$$

Two different types of calculation can be distinguished, depending on which parts of the magnetization are considered.

For the *collinear* case, only the z-component of the magnetization $m_z(\mathbf{r})$ is taken into account, and the density is split into spin-up/down contributions along the z-direction (or along another arbitrary direction related to the z-axis by a SU(2)-rotation). Thus, in collinear calculations, only σ_z instead of the full vector of Pauli matrices is considered in the magnetic Hamiltonian contribution Eq. (2.1.22). Consequently, only the z-component of magnetic fields is considered in collinear calculations. Spin-orbit coupling is, in general, a *non-collinear* effect (see below). Including only σ_z leads to $\hat{h}^{\mathrm{SV}}$ in Eq. (2.1.21) becoming block diagonal. Therefore, α and β components of the spinor SV wave function are decoupled. Furthermore, they are then also eigenstates of the spin-z operator $\hat{s}_z = \hbar/2\,\sigma_z$, and can thus be interpreted as scalar spin $\uparrow/\downarrow$ wave functions. Under these conditions, $m_z(\mathbf{r}) = n_\uparrow(\mathbf{r}) - n_\downarrow(\mathbf{r})$ and $n(\mathbf{r}) = n_\uparrow(\mathbf{r}) + n_\downarrow(\mathbf{r})$. Then, the HK energy functional is considered as a functional of $n(\mathbf{r})$ and $m_z(\mathbf{r})$ (or equivalently $n_\uparrow(\mathbf{r})$ and $n_\downarrow(\mathbf{r})$). Consequently, the same applies to the exchange-correlation functional. This formalism is equivalent to realizing the z-component of the magnetization $m_z(\mathbf{r})$ of the non-interacting KS reference system to equal the respective full interacting system's magnetization z-component [26] (in addition to the electron density).

Band structures, densities of states, or any other quantity resulting from a collinear calculation can be calculated independently for each spinor component, and therefore be interpreted spin-resolved. Magnetic configurations with spin alignments along the z-direction (collinear ferromagnetic, antiferromagnetic, ferrimagnetic) can be realized by inducing a magnetic moment through the application of an initial external magnetic field $B_{\mathrm{ext},z}(\mathbf{r})$ in the z-direction globally, or locally within MTs, and gradually switching it off during the SCF calculation. In this way, an effect equivalent to the spontaneous breaking of spin symmetry through exchange effects can be realized in the final configuration, with the magnetic field switched off. In such calculations, the magnetic exchange-correlation field interaction $b_{\mathrm{xc},z}(\mathbf{r})$ favors spin polarized solutions, while the kinetic energy $\langle \Psi_S[n] \,|\, T \,|\, \Psi_S[n] \rangle$ opposes them. The balance of both terms is deciding for whether a material can achieve a magnetic configuration, or not ([12], Chapter 2).

With a general magnetic field or when SO coupling is considered, the spin treatment becomes *non-collinear*, meaning the magnetization $\mathbf{m}(\mathbf{r})$ can point into any direction at $\mathbf{r}$. The SO and/or magnetic SV Hamiltonian contributions couple α and β Bloch spinor components through the full vector of Pauli matrices $\boldsymbol{\sigma}$, such that an interpretation as pure spin-up and -down-component is incorrect ($\alpha \neq \uparrow$ and $\beta \neq \downarrow$). In the non-collinear spin treatment, it is only possible to realize the magnetization vector's absolute value $|\mathbf{m}(\mathbf{r})|$ of the non-interacting model system to be equal to the full interacting system's value at every $\mathbf{r}$, when the full 4-current $j^\mu(\mathbf{r})$ is not considered [26]. In this case, the HK energy functional encompasses the electron density $n(\mathbf{r})$ and $|\mathbf{m}(\mathbf{r})|$. In turn, the exchange correlation functional becomes a functional of both quantities. The non-collinear spin treatment can also be described as regarding $\mathbf{m}(\mathbf{r})$ to be collinear locally [40], with a varying spin-quantization axis at different $\mathbf{r}$. This can be seen by projecting $\mathbf{m}(\mathbf{r})$ along its local direction, yielding $\mathbf{m}(\mathbf{r}) \cdot \frac{\mathbf{m}(\mathbf{r})}{|\mathbf{m}(\mathbf{r})|} = |\mathbf{m}(\mathbf{r})|$.

2.2 Maximally localized Wannier functions

2.2.1 Wannier functions as tight-binding basis

A different, much simpler approximate approach to solving the many-electron problem, other than DFT, is the *tight-binding* method. It is based on the superposition of atomic tight-binding orbitals $\varphi_n(\mathbf{r} - \mathbf{R})$, localized in real space around single atoms [36]. From these, auxiliary Bloch functions

$\phi^{\text{aux}}_{n\mathbf{k}}(\mathbf{r})$ are constructed like

$$\phi^{\text{aux}}_{n\mathbf{k}}(\mathbf{r}) = \sum_{\mathbf{R}} e^{i\mathbf{k}\cdot\mathbf{R}} \varphi_n(\mathbf{r}-\mathbf{R}) \; . \tag{2.2.1}$$

Strongly localized atomic orbitals are advantageous for the chemical interpretation of bonds and typically provide a small basis when a subspace of the full Hilbert space is considered. Further, it is easy to calculate quantities in reciprocal space with a fine sampling of $\mathbf{k}$ space using these localized orbitals, since Bloch states constructed from them depend on $\mathbf{k}$ only in the phase factor $e^{i\mathbf{k}\cdot\mathbf{R}}$. The auxiliary Bloch states give access to eigenenergies and thus eigenstates after a diagonalization of the Hamiltonian $\langle \phi^{\text{aux}}_{m\mathbf{k}} \,|\, \hat{h}^{\text{KS}} \,|\, \phi^{\text{aux}}_{n\mathbf{k}} \rangle$. With the resulting eigenstates, the BZ-integrals required for many quantities in reciprocal space are easy to compute [36]. The quality of results obtained with the tight-binding method entirely depends on the choices of single atom orbitals $\varphi_n(\mathbf{r}-\mathbf{R})$, and it can easily fail for accurate descriptions of delocalized valence and conduction electrons. Further, the accuracy of the obtained eigenenergies depends on the localization of the $\varphi_n(\mathbf{r}-\mathbf{R})$, when employing BvK boundary conditions (for details see Sec. 2.2.7).

It is, however, possible to construct an orthonormal, minimal, and optimally localized tight-binding basis starting from Bloch states (that are the result of a DFT calculation with a coarse reciprocal-space sampling $\{\mathbf{k}\}$) in terms of Wannier functions (WFs). This Wannier basis is entirely equivalent to the Bloch basis spanning the Hilbert space under consideration. By constructing new auxiliary Bloch functions at arbitrary points $\mathbf{q}$ in reciprocal space from these WFs via Eq. (2.2.1), Hamiltonian eigenfunctions and eigenstates can be interpolated onto a fine reciprocal space grid $\{\mathbf{q}\}$. WFs are more or less localized due to the gauge-freedom of Bloch functions they are constructed from, which can be exploited such that WFs can become maximally localized Wannier functions (MLWFs). These allow access to accurate interpolated eigenenergies when employing BvK boundary conditions.

In the following section, WFs are formally introduced. The subsequent sections will then treat the localization of WFs and the construction of MLWFs. In the section on Wannier interpolation, it will be demonstrated why MLWFs are ideally suited for interpolating eigenenergies and eigenstates of a many-body Hamiltonian. In each section, it will be described how MLWFs and the different quantities related to their construction are affected when calculated from a set of spin-polarized Bloch functions, as described in [27].

2.2.2 Wannier functions and their properties

Gregory H. Wannier defined WFs $w_{n\mathbf{R}}(\mathbf{r})$ by [3]:

$$w_{n\mathbf{R}}(\mathbf{r}) = \frac{V_u}{(2\pi)^3} \int_{\text{BZ}} \mathrm{d}\mathbf{k}\, e^{-i\mathbf{k}\cdot\mathbf{R}} \psi_{n\mathbf{k}}(\mathbf{r}) \; , \tag{2.2.2}$$

with $\mathbf{R}$ a real-space lattice vector and V_u the volume of the unit cell. In bra-ket notation, a WF is represented by $|n\mathbf{R}\rangle$ with $\langle \mathbf{r} \,|\, n\mathbf{R} \rangle = w_{n\mathbf{R}}(\mathbf{r})$, while equivalently a Bloch function $\psi_{n\mathbf{k}}(\mathbf{r})$ is represented by $|n\mathbf{k}\rangle$. The relation in Eq. (2.2.2) holds for each single band, which is part of an isolated group of bands[3]. It is possible to invert relationship Eq. (2.2.2):

$$\psi_{n\mathbf{k}}(\mathbf{r}) = \sum_{\mathbf{R}}^{\infty} e^{i\mathbf{k}\cdot\mathbf{R}} w_{n\mathbf{R}}(\mathbf{r}) \; . \tag{2.2.3}$$

[3] Isolated in the sense that there exists a non-zero gap in energy between the set of bands and all other bands, at every point in the BZ.

The transformation from Bloch functions to WFs takes the form of a "Fourier-like" transformation, where the conjugate pair of variables are continuous crystal-momentum (reciprocal-space) vectors $\mathbf{k}$ and discrete real space lattice vectors $\mathbf{R}$. Definition Eq. (2.2.2) assumes the reciprocal space to be continuous. Using a discrete $\mathbf{k}$-mesh with BvK boundary conditions, the integral in Eq. (2.2.2) is to be replaced by a finite sum over $\mathbf{k}$-points:

$$w_{n\mathbf{R}}(\mathbf{r}) = \frac{1}{N_\mathbf{k}} \sum_{\mathbf{k}}^{N_\mathbf{k}} e^{-i\mathbf{k}\cdot\mathbf{R}} \psi_{n\mathbf{k}}(\mathbf{r}) \ . \tag{2.2.4}$$

WFs are orthonormal when constructed from a set of orthonormal Bloch functions:

$$\begin{aligned} \langle n\mathbf{R} \,|\, n'\mathbf{R}\rangle^{\mathbb{R}^3} &= \frac{V_u^2}{(2\pi)^6} \int_{\mathrm{BZ}} \int_{\mathrm{BZ}} \mathrm{d}\mathbf{k}\, \mathrm{d}\mathbf{k}'\, e^{i\mathbf{k}\cdot\mathbf{R}} e^{-i\mathbf{k}'\cdot\mathbf{R}'} \langle n\mathbf{k} \,|\, n'\mathbf{k}'\rangle^{\mathbb{R}^3} \\ &= \frac{V_u^2}{(2\pi)^6} \int_{\mathrm{BZ}} \int_{\mathrm{BZ}} \mathrm{d}\mathbf{k}\, \mathrm{d}\mathbf{k}'\, e^{i\mathbf{k}\cdot\mathbf{R}} e^{-i\mathbf{k}'\cdot\mathbf{R}'} \delta_{nn'} \delta(\mathbf{k}-\mathbf{k}') \\ &= \frac{V_u}{(2\pi)^3} \int_{\mathrm{BZ}} \mathrm{d}\mathbf{k}\, e^{i\mathbf{k}\cdot(\mathbf{R}-\mathbf{R}')} \delta_{nn'} \\ &= \delta_{nn'} \delta_{\mathbf{R},\mathbf{R}'} \ , \end{aligned} \tag{2.2.5}$$

where in the second line Eq. (2.1.14) has been invoked. Further, WFs obtain a translational property from Bloch functions by making use of Eq. (2.1.13):

$$\begin{aligned} w_{n\mathbf{R}}(\mathbf{r}+\mathbf{R}') &= \frac{V_u}{(2\pi)^3} \int_{\mathrm{BZ}} \mathrm{d}\mathbf{k}\, e^{-i\mathbf{k}\cdot\mathbf{R}} \psi_{n\mathbf{k}}(\mathbf{r}+\mathbf{R}') \\ &= \frac{V_u}{(2\pi)^3} \int_{\mathrm{BZ}} \mathrm{d}\mathbf{k}\, e^{-i\mathbf{k}\cdot(\mathbf{R}-\mathbf{R}')} \psi_{n\mathbf{k}}(\mathbf{r}) \\ &= w_{n\mathbf{R}-\mathbf{R}'}(\mathbf{r}) \ . \end{aligned} \tag{2.2.6}$$

Setting $\mathbf{R} = 0$ and replacing $\mathbf{R}' \to -\mathbf{R}'$, it becomes apparent that a WF of index $\mathbf{R}$ is just a shifted image of the WF associated to the *home unit cell* at $\mathbf{R} = 0$ like

$$w_{n\mathbf{R}}(\mathbf{r}) = w_{n\mathbf{0}}(\mathbf{r}-\mathbf{R}) \ . \tag{2.2.7}$$

WFs span the same Hilbert space as the set of Bloch functions they are constructed from. It is illustrative for this fact to construct the projection operator onto the Hilbert subspace spanned by original Bloch states $\hat{P}$ and express it in WFs [27]:

$$\begin{aligned} \hat{P} &= \frac{V_u}{(2\pi)^3} \sum_n \int_{\mathrm{BZ}} \mathrm{d}\mathbf{k}\, |n\mathbf{k}\rangle\langle n\mathbf{k}| \\ &= \frac{V_u}{(2\pi)^3} \sum_n \sum_{\mathbf{R},\mathbf{R}'} \int_{\mathrm{BZ}} \mathrm{d}\mathbf{k}\, e^{i\mathbf{k}\cdot(\mathbf{R}-\mathbf{R}')} |n\mathbf{R}\rangle\langle n\mathbf{R}'| \\ &= \sum_{n\mathbf{R}} |n\mathbf{R}\rangle\langle n\mathbf{R}| \ , \end{aligned} \tag{2.2.8}$$

where in the third line the identity $\int_{\mathrm{BZ}} \mathrm{d}\mathbf{k} e^{i\mathbf{k}\cdot(\mathbf{R}_2-\mathbf{R}_2)} = (2\pi)^3/V_u \delta_{\mathbf{R}_1,\mathbf{R}_2}$ is used.

All relations above hold when spinor Bloch states are utilized to construct WFs. The latter inherit the spinor nature from Bloch spinors.

2.2.3 Gauge freedom

The tight-binding method is computationally efficient for interpolations only if the employed orbitals are strictly of atomic nature, i.e., strongly localized so that overlaps with shifted images of

larger $\mathbf{R}$ vanish. Invoking a simple 1-dimensional example of a single WF in a crystal of lattice constant a, constructed from a Bloch planewave with $u_k(r) = 1$:

$$\psi_{nk}(x) = \frac{1}{C} e^{ikx} \,. \tag{2.2.9}$$

Then

$$w_{n0}(\mathbf{r}) \propto \int_{-\pi/a}^{\pi/a} \mathrm{d}k\, e^{-ik\cdot 0} e^{ikx} \propto \frac{\sin(\pi x/a)}{x} \,, \tag{2.2.10}$$

which decays algebraically only and thus has considerable overlap with $w_{na}(\mathbf{r})$. This example (though oversimplified for a complex crystal) shows how mathematically, WFs may by default not be sufficiently localized to provide a good tight-binding basis.

However, it is possible to exploit the gauge freedom of Bloch functions in order to construct more localized WFs. For a single isolated band $|n\mathbf{k}\rangle$, replacing

$$\psi_{n\mathbf{k}}(\mathbf{r}) \to \phi_{n\mathbf{k}}(\mathbf{r}) = e^{i\varphi_n(\mathbf{k})} \psi_{n\mathbf{k}}(\mathbf{r}) \tag{2.2.11}$$

does not alter the physical behavior of the system, when $\varphi_n(\mathbf{k})$ is a real function called *phase*, satisfying $\varphi_n(\mathbf{k}+\mathbf{G}) = \varphi_n(\mathbf{k}) + \mathbf{G}\cdot\Delta\mathbf{R}$ with a reciprocal lattice vector $\mathbf{G}$ and a real-space lattice vector $\Delta\mathbf{R}$ [27]. The associated WF is calculated from the altered wave function as

$$\begin{aligned} w_{n\mathbf{R}}(\mathbf{r}) &= \frac{V_u}{(2\pi)^3} \int_{\mathrm{BZ}} \mathrm{d}\mathbf{k}\, e^{-i\mathbf{k}\cdot\mathbf{R}} \phi_{n\mathbf{k}}(\mathbf{r}) \\ &= \frac{V_u}{(2\pi)^3} \int_{\mathrm{BZ}} \mathrm{d}\mathbf{k}\, e^{-i[\mathbf{k}\cdot\mathbf{R} - \varphi_n(\mathbf{r})]} \psi_{n\mathbf{k}}(\mathbf{r}) \,, \end{aligned} \tag{2.2.12}$$

from which it is apparent that the WFs' shape and spread, in general, changes under a gauge transformation of Bloch states described above [27]. This also goes to show that different WFs can have a wide variety of shapes within a given system, other than Bloch states, which are determined in shape up to a phase $\varphi_n(\mathbf{k})$. Due to the nature of the Fourier-like transform in Eq. (2.2.2), the smoother Bloch states are in reciprocal space due to their phase, the more localized the WFs constructed from them become. The gauge freedom can thus be exploited for this purpose.

In the case of an isolated set of J bands, the notion of gauge freedom is generalized by

$$\phi_{n\mathbf{k}}(\mathbf{r}) = \sum_{m=1}^{J} U^{\mathbf{k}}_{mn} \psi_{n\mathbf{k}}(\mathbf{r}) \,, \tag{2.2.13}$$

where $U^{\mathbf{k}}$ is a unitary matrix of size $J \times J$ "rotating" or "mixing" original Bloch functions among each other. While no longer being Hamiltonian eigenstates, these rotated states $\phi_{n\mathbf{k}}(\mathbf{r})$ span the same Hilbert subspace as the original Bloch states. Their quantum number n can meanwhile no longer be interpreted as a band-index referring to a single band. Rather, the new set of rotated states is associated to the set of original bands. The same applies to the WFs constructed from these rotated states:

$$w_{n\mathbf{R}}(\mathbf{r}) = \frac{V_u}{(2\pi)^3} \int_{\mathrm{BZ}} \mathrm{d}\mathbf{k}\, e^{-i\mathbf{k}\cdot\mathbf{R}} \phi_{n\mathbf{k}}(\mathbf{r}) \,. \tag{2.2.14}$$

The rotation of spinor Bloch states with a unitary $\widetilde{U}^{\mathbf{k}}$ is applied to the whole spinor object, in the same fashion as for scalar states [27]. WFs $\widetilde{w}_{n\mathbf{k}}(\mathbf{r})$ (unitary mixing matrices $\widetilde{U}^{\mathbf{k}}$) are written with a tilde, if they are created from (apply to) spin-polarized Bloch states.

2.2.4 Marzari-Vandebilt method for constructing MLWFs

An optimal choice of unitary matrices $U^{\mathbf{k}}_{mn}$ can lead to a set of *maximally localized* Wannier functions (MLWFs)[4]. At this point, it is necessary to introduce a well-defined criterion of WF localization. Marzari and Vanderbilt proposed the following *spread functional*, to measure the total spread of a set of WFs constructed from Eq. (2.2.14) [14]:

$$\Omega = \sum_{n=1}^{J} \left[\langle n\mathbf{0} \,|\, r^2 \,|\, n\mathbf{0} \rangle^{\mathrm{SC}} - \langle n\mathbf{0} \,|\, \mathbf{r} \,|\, n\mathbf{0} \rangle^{\mathrm{SC}^2} \right] , \tag{2.2.15}$$

where $r^2 = \mathbf{r}^2$. Ω quantifies the quadratic spread of the position operator in terms of the WFs $|n\mathbf{0}\rangle$ [27]. This measure of localization is used throughout this work. The spread functional is minimized as a functional of the unitary mixing of Bloch states, from which WFs are constructed, as $\Omega = \Omega[\{U^{\mathbf{k}}\}]$, by variation of the set of $\{U^{\mathbf{k}}\}$. When fully converged, the final set yields optimally rotated states $\phi_{m\mathbf{k}}(\mathbf{r})$ that lead to MLWFs by Eq. (2.2.14). Following [14], Eq. (2.2.15) can be decomposed into three parts like $\Omega = \Omega_I + \Omega_{OD} + \Omega_D$, with the independent, off-diagonal and diagonal contribution Ω_I, Ω_{OD}, and Ω_D, respectively. Together with expressions provided by Blount [6], they are expressed by:

$$\begin{aligned}
\Omega_I &= \frac{1}{N_{\mathbf{k}}} \sum_{\mathbf{k},\mathbf{b}} \mathrm{w}_{\mathbf{b}} \left(J - \sum_{m,n} \left| M^{\mathbf{k},\mathbf{b}}_{mn} \right|^2 \right) \\
\Omega_D &= \frac{1}{N_{\mathbf{k}}} \sum_{\mathbf{k},\mathbf{b}} \mathrm{w}_{\mathbf{b}} \sum_{n} \left(-\mathrm{Im} \ln M^{\mathbf{k},\mathbf{b}}_{nn} - \mathbf{b} \cdot \left[\frac{1}{N_{\mathbf{k}}} \sum_{\mathbf{k}',\mathbf{b}'} \mathrm{w}_{\mathbf{b}'} \mathbf{b}' \mathrm{Im} \ln M^{\mathbf{k}',\mathbf{b}'}_{nn} \right] \right)^2 \\
\Omega_{OD} &= \sum_{\mathbf{k},\mathbf{b}} \mathrm{w}_{\mathbf{b}} \sum_{m \neq n} \left| M^{\mathbf{k},\mathbf{b}}_{mn} \right| ,
\end{aligned} \tag{2.2.16}$$

where $\mathbf{b}$ is a member of a set of vectors connecting $\mathbf{k}$ to its nearest neighbors in reciprocal space. Together with weights $\mathrm{w}_{\mathbf{b}}$, they are used to approximate $\nabla_{\mathbf{k}}$ by finite differences. $\nabla_{\mathbf{k}}$ is used in Blount's relations for the evaluation of the position operator expectation values in Eq. (2.2.15) in reciprocal space. Observing Eq. (2.2.16), it is clear that all Ω-contributions can be calculated from the matrices $M^{\mathbf{k},\mathbf{b}}_{mn}$, which are defined by:

$$M^{\mathbf{k},\mathbf{b}}_{mn} = \langle \phi_{m\mathbf{k}} \,|\, e^{-i\mathbf{b}\cdot\mathbf{r}} \,|\, \phi_{n\mathbf{k}+\mathbf{b}} \rangle^{V_u} . \tag{2.2.17}$$

By substituting Eq. (2.2.13) for the rotated Bloch states, it follows

$$M^{\mathbf{k},\mathbf{b}}_{mn} = \sum_{m'n'} U^{\mathbf{k}*}_{mm'} \underbrace{\langle m'\mathbf{k} \,|\, e^{-i\mathbf{b}\cdot\mathbf{r}} \,|\, n'\mathbf{k}+\mathbf{b} \rangle^{V_u}}_{\equiv \mathcal{M}^{\mathbf{k},\mathbf{b}}_{m'n'}} U^{\mathbf{k}+\mathbf{b}}_{n'n} . \tag{2.2.18}$$

The quantity $\mathcal{M}^{\mathbf{k},\mathbf{b}}_{mn} = \langle m\mathbf{k} \,|\, e^{-i\mathbf{b}\cdot\mathbf{r}} \,|\, n\mathbf{k}+\mathbf{b} \rangle$ shall be referred to as the *planewave* (PW) matrix. It can be calculated once and for all from initial Bloch states $|n\mathbf{k}\rangle$, at the beginning of the Ω-minimization.

When the SV method is utilized, Bloch functions $\widetilde{\psi}_{n\mathbf{k}}(\mathbf{r})$ and hence mixed bands $\widetilde{\phi}_{n\mathbf{k}}(\mathbf{r})$ take spinor form. Then, in the calculation of the SV PW matrix $\widetilde{\mathcal{M}}^{\mathbf{k},\mathbf{b}}$, a sum over spinor components

[4] Wannier functions are still SC-periodic. The notion of maximal localization thus refers to a maximal localization within one SC.

is introduced through the evaluation of the inner product of Bloch spinors [21]:

$$\begin{aligned}\widetilde{\mathcal{M}}^{\mathbf{k},\mathbf{b}}_{mn} &= \langle \widetilde{\psi}_{m\mathbf{k}} \,|\, e^{-i\mathbf{b}\cdot\mathbf{r}} \,|\, \widetilde{\psi}_{n\mathbf{k}+\mathbf{b}} \rangle \\ &= \sum_{\sigma=\alpha,\beta} \langle \widetilde{\psi}_{m\mathbf{k}\sigma} \,|\, e^{-i\mathbf{b}\cdot\mathbf{r}} \,|\, \widetilde{\psi}_{n\mathbf{k}+\mathbf{b}\sigma} \rangle \,.\end{aligned} \tag{2.2.19}$$

In each iteration step of the spread functional minimization, with updates of the $\{U^{\mathbf{k}}\}$, $M^{\mathbf{k},\mathbf{b}}$, and hence all contributions to the spread functional can be calculated from the PW matrix $\mathcal{M}^{\mathbf{k},\mathbf{b}}$. Updates to the $U^{\mathbf{k}}$ are computed from the gradient $G^{\mathbf{k}}$ to the spread functional, w.r.t. components of the different $U^{\mathbf{k}}$, at each $\mathbf{k}$. The gradients are functionals of $M^{\mathbf{k},\mathbf{b}}$, too [14]. With these ingredients, a strategy for minimizing the spread functional of unitary mixing matrices $\Omega[\{U^{\mathbf{k}}\}]$ is laid out, which provides the optimal set $\{U^{\mathbf{k}}\}$ leading to MLWFs at the global minimum. The Marzari-Vanderbilt method for the construction of MLWFs is the foundation of the recent Wannier implementation in `exciting`. The detailed procedure of how to minimize $\Omega[\{U^{\mathbf{k}}\}]$ as a functional is not described within this work. It is a high-dimensional minimization involving $N_{\mathbf{k}}$ matrices $U^{\mathbf{k}}$ of size $J \times J$. Their entries need to be chosen under the constraint that the $U^{\mathbf{k}}$ are from the manifold of unitary matrices. This fact imposes manifold constraints on the gradients of the spread functional and the overall optimization. The reader is referred to [14] for additional information.

It should be mentioned that a good initial guess for MLWFs is required to efficiently converge this high-dimensional minimization. For this purpose, the recent Wannier implementation automatically generates a set of *projection functions* [14] from local orbitals (readily available in the LAPW+LO basis), by using the Aufbau principle [38, 43]. These are then systematically refined to provide a good initial guess for minimizing the spread functional using the *optimized projection function* method [31]. To automatically generate a set of projection functions for spinor MLWFs, the author of [38] extended the generation scheme to spinors. The resulting initial guesses are utilized within this work's spinor adaptation of the `exciting` Wannier implementation.

2.2.5 Entangled energy bands

So far, only isolated sets of bands and WFs calculated from these have been considered. However, many bands, e.g. in metals, do not form such isolated groups. In many cases, there is at least one band that is attached to bands outside the considered energy window at some point $\mathbf{k}$ in reciprocal space. Consequently, the number of these *entangled* bands fully contained in the energy window differs at different points throughout the BZ. This leads to a non-square unitary mixing matrix $\mathcal{U}^{\mathbf{k}}_{mn}$ of different sizes at different $\mathbf{k}$ in the construction of MLWFs, which may also mix bands of very different characters, hindering the smoothness of mixed Bloch states and thus the localization of WFs.

To tackle these problems, Souza, Marzari, and Vanderbilt (SMV) propose an energy *disentanglement* procedure. It aims at disentangling the one J-dimensional subspace from the $\mathcal{J}_{\mathbf{k}} \geq J$ bands, contained in a considered (outer) energy window at each $\mathbf{k}$, which leads to the smallest spread functional contribution Ω_I, compared to all other possible subspaces [17]. This contribution Ω_I is gauge invariant w.r.t. the application of a unitary mixing $U^{\mathbf{k}}$ within the square disentangled subspace of dimension J, but can be interpreted as a measure for the "change of band character" for the case of entangled bands [17]. Minimizing Ω_I should therefore give the "smoothest" subspace for the Wannierization procedure. For the construction of MLWFs from entangled states, they suggest a two-step procedure in which first a set of semi-unitary disentanglement matrices $\{\mathcal{U}^{\mathbf{k}}\}$ of dimension $\mathcal{J}_{\mathbf{k}} \times J$ at each $\mathbf{k}$ is to be optimized for, by minimizing $\Omega_I[\{\mathcal{U}^{\mathbf{k}}\}]$. The spread contribution Ω_I and the gradient to Ω_I w.r.t to the $\mathcal{U}^{\mathbf{k}}$ can be entirely expressed by $\mathcal{U}^{\mathbf{k}}\mathcal{M}^{\mathbf{k},\mathbf{b}}\mathcal{U}^{\mathbf{k}+\mathbf{b}}$, providing a starting point for a minimization procedure (for details see [17]). The disentangled

subspace is composed of J *disentangled* bands $\Phi_{m\mathbf{k}}(\mathbf{r})$ that are calculated from original Bloch states by

$$\Phi_{m\mathbf{k}}(\mathbf{r}) = \sum_{n}^{\mathcal{J}_\mathbf{k}} \mathcal{U}^{\mathbf{k}}_{nm} \psi_{n\mathbf{k}}(\mathbf{r}) \,. \tag{2.2.20}$$

MLWFs are then constructed in a second step, by applying a unitary mixing $U^{\mathbf{k}}$ to the $\Phi_{m\mathbf{k}}(\mathbf{r})$, instead of original $\psi_{m\mathbf{k}}(\mathbf{r})$ (compare Sec. 2.2.4). When employing the SMV disentanglement procedure, the PW matrix update equation Eq. (2.2.18) for this second step is altered by replacing $|\psi_{n\mathbf{k}}\rangle \to |\Phi_{n\mathbf{k}}\rangle$:

$$\begin{aligned} (M^{\mathbf{k},\mathbf{b}}_{mn})^{\mathrm{dis}} &= \sum_{m'}^{\mathcal{J}_\mathbf{k}} \sum_{n'}^{\mathcal{J}_{\mathbf{k}+\mathbf{b}}} U^{\mathbf{k}*}_{mm'} \langle \Phi_{m'\mathbf{k}} \,|\, e^{-i\mathbf{b}\cdot\mathbf{r}} \,|\, \Phi_{n'\mathbf{k}+\mathbf{b}} \rangle^{\mathrm{SC}} U^{\mathbf{k}+\mathbf{b}}_{n'n} \\ \Leftrightarrow (M^{\mathbf{k},\mathbf{b}})^{\mathrm{dis}} &= (U^{\mathbf{k}})^\dagger (\mathcal{U}^{\mathbf{k}})^\dagger \mathcal{M}^{\mathbf{k},\mathbf{b}} \mathcal{U}^{\mathbf{k}+\mathbf{b}} U^{\mathbf{k}+\mathbf{b}} \,, \end{aligned} \tag{2.2.21}$$

where the $\mathcal{U}^{\mathbf{k}}$ are fixed from the disentanglement step for the SMV method and $\mathcal{M}^{\mathbf{k},\mathbf{b}}$ is the PW matrix calculated from original (entangled) Bloch states.

In addition to the *outer* energy window encompassing the entangled states, it is further possible to define an *inner* energy window. In order to reproduce entangled bands exactly inside this inner window, it is demanded that $\mathcal{U}^{\mathbf{k}}_{mm'} = \delta_{mm'}$ for a state $\psi_{m\mathbf{k}}(\mathbf{r})$ whose energy $\epsilon_{m\mathbf{k}}$ lies inside the inner window at $\mathbf{k}$ [17]. This ensures that during the disentanglement step, bands in the inner energy window are fixed, i.e., the corresponding states are not mixed with those outside of it. Let $M_\mathbf{k}$ be the number of states in the inner energy window at $\mathbf{k}$. Then the number J of MLWFs to construct needs to be chosen such that $M_\mathbf{k} \leq J \leq \mathcal{J}_\mathbf{k}$ for all points throughout the BZ. In this case, only the $\mathcal{J}_\mathbf{k} - M_\mathbf{k}$ states that are contained inside the outer but outside the inner energy window can contribute to the minimization of Ω_I at each $\mathbf{k}$ [17]. For later purposes, the energy windows shall be defined. The *outer* energy window is defined as $E^{\mathrm{out}} = [\epsilon^{\mathrm{outer}}_{\mathrm{min}}, \epsilon^{\mathrm{outer}}_{\mathrm{max}}]$. The *inner* energy window is fully contained within the outer energy window and defined as $E^{\mathrm{in}} = [\epsilon^{\mathrm{inner}}_{\mathrm{min}}, \epsilon^{\mathrm{inner}}_{\mathrm{max}}] \subset E^{\mathrm{out}}$ with $\epsilon^{\mathrm{outer}}_{\mathrm{min}} \leq \epsilon^{\mathrm{inner}}_{\mathrm{min}} < \epsilon^{\mathrm{inner}}_{\mathrm{max}} \leq \epsilon^{\mathrm{outer}}_{\mathrm{max}}$ (only one of the two $\leq$ can be equal). Let the *outer-only* window be defined as $E^{\text{out-only}} = E^{\mathrm{out}} \setminus E^{\mathrm{in}}$, containing energies inside the outer, but outside the inner energy window

A more recent disentanglement approach described in [35] supplies a method for the joint optimization for a disentangled subspace and unitary mixing within this subspace in a single combined step, leading to MLWFs of equal or, usually, lower total spread Ω compared to the two-step SMV method. This *full disentanglement* allows for a higher Ω_I if a smaller total spread Ω is thereby achieved. Instead of two consecutive separate minimizations of $\Omega_I[\{\mathcal{U}^{\mathbf{k}}\}]$ and $\Omega[\{U^{\mathbf{k}}\}]$, the total spread is minimized as a functional $\Omega[\{(X^{\mathbf{k}}, Y^{\mathbf{k}})\}]$. $X^{\mathbf{k}}$ is a $J \times J$ matrix and $Y^{\mathbf{k}}$ is a matrix of size $(\mathcal{J}_\mathbf{k} - J) \times (J - M_\mathbf{k})$, defining

$$\widehat{U}^{\mathbf{k}} = \begin{pmatrix} Y^{\mathbf{k}} & \mathbf{0} \\ \mathbf{0} & \mathbf{I}_{M_\mathbf{k}} \end{pmatrix} X^{\mathbf{k}} \tag{2.2.22}$$

such that optimal rotated bands $\phi_{n\mathbf{k}}(\mathbf{r})$ leading to MLWFs result from entangled original Bloch bands directly as[5]

$$\phi_{n\mathbf{k}}(\mathbf{r}) = \sum_{m}^{\mathcal{J}_\mathbf{k}} \widehat{U}^{\mathbf{k}}_{mn} \psi_{m\mathbf{k}}(\mathbf{r}) \,. \tag{2.2.23}$$

[5] In order to match the construction of $\widehat{U}^{\mathbf{k}}$ the initial $\psi_{m\mathbf{k}}(\mathbf{r})$ need to be ordered such the bands in the inner energy window are always counted before others from the outer-only window by index m.

As described in [35], the full disentanglement method can be considered a generalization of the two-step procedure proposed by Souza, Marzari, and Vanderbilt. Compared to the SMV method, it is possible to split $\widehat{U}^{\mathbf{k}} = \mathcal{U}^{\mathbf{k}} U^{\mathbf{k}}$ by identifying

$$\mathcal{U}^{\mathbf{k}} = \begin{pmatrix} Y^{\mathbf{k}} & \mathbf{0} \\ \mathbf{0} & \mathbf{I}_{M_{\mathbf{k}}} \end{pmatrix} \text{ and } U^{\mathbf{k}} = X^{\mathbf{k}} . \tag{2.2.24}$$

For the full disentanglement method, the minimization of the spread functional can therefore be regarded as calculating $\arg\min_{\mathcal{U}^{\mathbf{k}} U^{\mathbf{k}}} \Omega[\{\mathcal{U}^{\mathbf{k}} U^{\mathbf{k}}\}]$. Both methods are implemented within the `exciting` code. In the following sections, the splitting in Eq. (2.2.24) is employed to make adaptations of the SMV and full disentanglement methods comparable. Further, the case of isolated bands can always be retrieved by fixing $\mathcal{U}^{\mathbf{k}} = \mathbf{1}_J$ for both methods.

2.2.6 Collinear spin-pure Wannier functions

When calculating MLWFs from Bloch states that are the result of a collinear SV-calculation, the association of spinor components with spin up and down would be lost when mixing spin-pure ↑- and ↓-states through $U^{\mathbf{k}}_{mn}$. However, since the Hilbert spaces of up- and down-states are decoupled, one can construct two sets of MLWFs separately [27]. The joined set of both spin-up/down MLWFs again spans the same subspace as the set of all original states. When a disentanglement of states is necessary, it can be advantageous to only mix states of the same spin character via $\mathcal{U}^{\mathbf{k}}$ during the disentanglement step, such that the two disentangled subspaces remain spin-pure [27].

Alternatively, in [21], collinear spin-pure MLWFs have been constructed after an energy disentanglement step via the SMV method that included initial DFT states of both spin up/down, thus mixing spins. Effectively spin-pure subspaces were then extracted post-disentanglement, by diagonalizing the matrix representation of the $\hat{s}_z$ operator in the disentangled subspace and assigning states to spin-pure subspaces by S_z eigenvalues close to $+1$ or -1 (units of $\hbar/2$). In practice, for iron, with a magnetic field applied in the z-direction and core electrons treated in a pseudopotential framework considering SO coupling, this yielded eigenvalues $|s| > 0.999$ [21], implying that SO coupling has a weak effect on the valence and conduction bands of iron. Then, with energy-disentangled, spin-pure subspaces retrieved, the full spread-functional minimization was performed in each spin-pure subspace separately, yielding virtually spin-pure MLWFs. While in [21] this method is employed on top of a formally non-collinear DFT calculation considering SO coupling, it could be used on top of an exactly spin-pure collinear DFT calculation, too.

However, the method of Wang et al. is not applicable when employing the full disentanglement method, because the disentanglement and spread-functional optimization within the disentangled subspace are conducted in a joint step. Then, no diagonalization of S_z can be conducted in between the disentanglement step and the spread-functional optimization. Therefore, in this work, these two steps are conducted separately in the subspaces spanned by collinear spin-up/down states resulting from a first-principles DFT calculation. The same procedure is applied when employing the SMV disentanglement method. By conducting the SMV energy disentanglement entirely separately in the spin-up/down subspaces, some flexibility for the minimization of Ω_I may be sacrificed compared to the method in [21]. However, it can be guaranteed that exactly spin-pure MLWFs result for all collinear systems and choices of disentanglement windows.

2.2.7 Wannier interpolation

Several quantum-mechanical material properties of interest require calculations with a dense sampling in reciprocal space, e.g., the density of states (DOS) or optical spectra. For this purpose, a

large number of $\mathbf{k}$ points must be considered for solving the KS/SV secular equation. However, diagonalizing the KS Hamiltonian in the LAPW+LO basis at every point $\mathbf{k}$ in every SCF-cycle step comes at a high computational cost of $\mathcal{O}(N_{\text{iter}}^{\text{SCF}} N_{\mathbf{k}} N_{\text{LAPW+LO}}^3)$. If the SV method is employed, the additional SV-step diagonalization further raises the cost. When quantities require a fine reciprocal space sampling, first a SCF calculation can be conducted on a coarser $\mathbf{k}$-grid. Then, by freezing the obtained ground state density, $H^{\mathbf{k}}$ can be diagonalized non-self-consistently in the LAPW+LO basis, at arbitrary points in reciprocal space $\mathbf{q}$, yielding eigenenergies and wave functions. This approach usually provides good accuracy when the SCF step is conducted on a coarse, but still sufficiently dense $\mathbf{k}$-grid. Nevertheless, (i) it is still expensive due to the LAPW+LO basis size and (ii) the cost of this scheme becomes prohibitive when hybrid exchange-correlation functionals are employed. When these are utilized, the xc-potential contains non-local terms, i.e., $v_{\text{ext}} = v_{\text{ext}}(\mathbf{r}, \mathbf{r}')$. Further, the post-DFT GW method allows for the (perturbative) correction of single particle eigenvalues to obtain quasi-particle energies, but also requires the calculation of the non-local *self-energy* $\Sigma(\mathbf{r}, \mathbf{r}'; \omega)$ [15]. Thus, when employing hybrid exchange-correlation functionals or the GW-method, the cost of each diagonalization of the Hamiltonian scales as $\mathcal{O}(N_B^4)$. Consequently, a more efficient method for interpolating $\mathbf{k}$-dependent quantities from coarse reciprocal-space grids onto dense grids is desired.

Starting from the tight-binding approach, Slater and Koster suggested a method to interpolate quantities in reciprocal space using atomic orbitals [4]. They argued that when overlaps between orbitals centered on different atoms become small, then matrix elements containing these orbitals can be disregarded. Following this argument, the number of matrix elements required for an accurate interpolation can be greatly reduced when atomic orbitals are maximally localized around their parent atoms. MLWFs pose an ideally suited set of atomic-orbital-like functions for the Slater-Koster interpolation scheme, since they (i) span the complete Hilbert space under consideration, are (ii) orthonormal, and (iii) are maximally localized with respect to a localization criterion.

In this section, it will be shown how MLWFs can be used to interpolate energies onto a fine grid, following [27]. Let $\mathbf{q}$ be a vector in reciprocal space that is a member of a fine interpolation grid, or a specific path through the BZ. With a set of finalized $\{U^{\mathbf{k}}\}$ (or $\{\mathcal{U}^{\mathbf{k}} U^{\mathbf{k}}\}$ with disentanglement), MLWFs result from optimally rotated Bloch functions (Eq. (2.2.13)) and a discrete BvK $\mathbf{k}$-grid as

$$w_{n\mathbf{R}}(\mathbf{r}) = \frac{1}{N_{\mathbf{k}}} \sum_{\mathbf{k}}^{N_{\mathbf{k}}} e^{-i\mathbf{k}\cdot\mathbf{R}} \phi_{n\mathbf{k}}(\mathbf{r}) \; . \tag{2.2.25}$$

Inverting this equation for a vector $\mathbf{q}$ instead of $\mathbf{k}$ yields a set of auxiliary Bloch states $\phi_{n\mathbf{q}}^{\text{aux}}(\mathbf{r})$ (which are not Hamiltonian eigenstates):

$$\phi_{n\mathbf{q}}^{\text{aux}}(\mathbf{r}) = \sum_{\mathbf{R}} e^{i\mathbf{q}\cdot\mathbf{R}} w_{n\mathbf{R}}(\mathbf{r}) \; . \tag{2.2.26}$$

Within the gauge of these auxiliary states, Hamiltonian matrix elements are calculated as

$$H_{mn}^{\mathbf{q},\text{aux}} = \langle \phi_{m\mathbf{q}}^{\text{aux}} \,|\, \hat{h} \,|\, \phi_{n\mathbf{q}}^{\text{aux}} \rangle^{V_u} \; . \tag{2.2.27}$$

The KS (or SV for the spinor case) Hamiltonian is abbreviated as $\hat{h}$ in the following. These matrix elements can be calculated as either an integral over one unit cell or over a SC containing $N_{\mathbf{k}}$ unit cells:

$$\langle \phi_{m\mathbf{q}}^{\text{aux}} \,|\, \hat{h} \,|\, \phi_{n\mathbf{q}}^{\text{aux}} \rangle^{V_u} = \frac{1}{N_{\mathbf{k}}} \langle \phi_{m\mathbf{q}}^{\text{aux}} \,|\, \hat{h} \,|\, \phi_{n\mathbf{q}}^{\text{aux}} \rangle^{\text{SC}} \tag{2.2.28}$$

Switching to the SC domain is useful when re-expressing auxiliary states $|\phi_{n\mathbf{q}}^{\text{aux}}\rangle$ in WFs using

Eq. (2.2.26):

$$\langle \phi^{\text{aux}}_{m\mathbf{q}} \,|\, \hat{h} \,|\, \phi^{\text{aux}}_{n\mathbf{q}} \rangle^{\text{SC}} = \sum_{\mathbf{R},\mathbf{R}'} e^{i\mathbf{q}\cdot(\mathbf{R}'-\mathbf{R})} \langle m\mathbf{R} \,|\, \hat{h} \,|\, n\mathbf{R}' \rangle^{\text{SC}} \tag{2.2.29}$$

The RHS matrix elements can be rewritten using Eq. (2.2.6), Eq. (2.2.7), and $\hat{h}(\mathbf{r}+\mathbf{R}) = \hat{h}(\mathbf{r})$:

$$\begin{aligned}
\langle m\mathbf{R} \,|\, \hat{h} \,|\, n\mathbf{R}' \rangle^{\text{SC}} &= \int_{\text{SC}} \mathrm{d}\mathbf{r}\, w^*_{m\mathbf{R}}(\mathbf{r}) \hat{h}(\mathbf{r}) w_{n\mathbf{R}'}(\mathbf{r}) \\
&= \int_{\text{SC}} \mathrm{d}\mathbf{r}\, w^*_{m\mathbf{0}}(\mathbf{r}-\mathbf{R}) \hat{h}(\mathbf{r}) w_{n\mathbf{R}'}(\mathbf{r}) \\
&= \int_{\text{SC}} \mathrm{d}\mathbf{r}'\, w^*_{m\mathbf{0}}(\mathbf{r}') \hat{h}(\mathbf{r}'+\mathbf{R}) w_{n\mathbf{R}'}(\mathbf{r}'+\mathbf{R}) \\
&= \int_{\text{SC}} \mathrm{d}\mathbf{r}'\, w^*_{m\mathbf{0}}(\mathbf{r}') \hat{h}(\mathbf{r}') w_{n\mathbf{R}'-\mathbf{R}}(\mathbf{r}') \\
&= \langle m\mathbf{0} \,|\, \hat{h} \,|\, n\mathbf{R}'-\mathbf{R} \rangle^{\text{SC}} ,
\end{aligned} \tag{2.2.30}$$

with the substitution $\mathbf{r}' = \mathbf{r}+\mathbf{R}$, $\mathrm{d}\mathbf{r}' = \mathrm{d}\mathbf{r}$ in line three. Using this relation, Eq. (2.2.27) yields:

$$\begin{aligned}
H^{\mathbf{q},\text{aux}}_{mn} &= \frac{1}{N_{\mathbf{k}}} \sum_{\mathbf{R},\mathbf{R}'} e^{i\mathbf{q}\cdot(\mathbf{R}'-\mathbf{R})} \langle m\mathbf{0} \,|\, \hat{h} \,|\, n\mathbf{R}'-\mathbf{R} \rangle^{\text{SC}} \\
&= \sum_{\mathbf{R}} e^{i\mathbf{q}\cdot\mathbf{R}} \langle m\mathbf{0} \,|\, \hat{h} \,|\, n\mathbf{R} \rangle^{\text{SC}} .
\end{aligned} \tag{2.2.31}$$

Rearranging the sum to go over only $\mathbf{R}$ is justified, since the set of $\{\mathbf{R}\}$ contains any possible difference $\mathbf{R}'-\mathbf{R}$ of real-space lattice vectors within the BvK SC. For the calculation of $H^{\mathbf{q},\text{aux}}_{mn}$, Eq. (2.2.31) is expressed again for $\mathbf{k}$ instead of $\mathbf{q}$:

$$H^{\mathbf{k},\text{aux}}_{mn} = \langle \phi^{\text{aux}}_{m\mathbf{k}} \,|\, \hat{h} \,|\, \phi^{\text{aux}}_{n\mathbf{k}} \rangle = \sum_{\mathbf{R}} e^{i\mathbf{k}\cdot\mathbf{R}} \langle m\mathbf{0} \,|\, \hat{h} \,|\, n\mathbf{R} \rangle^{\text{SC}} \tag{2.2.32}$$

The inverse Fourier transform is applied to this equation, yielding:

$$\begin{aligned}
\langle m\mathbf{0} \,|\, \hat{h} \,|\, n\mathbf{R} \rangle^{\text{SC}} &= \frac{1}{N_{\mathbf{k}}} \sum_{\mathbf{k}} e^{-i\mathbf{k}\cdot\mathbf{R}} \langle \phi^{\text{aux}}_{m\mathbf{k}} \,|\, \hat{h} \,|\, \phi^{\text{aux}}_{n\mathbf{k}} \rangle \\
&= \frac{1}{N_{\mathbf{k}}} \sum_{\mathbf{k}} e^{-i\mathbf{k}\cdot\mathbf{R}} [U^{\mathbf{k}\dagger} H^{\mathbf{k}} U^{\mathbf{k}}]_{mn} ,
\end{aligned} \tag{2.2.33}$$

where $H^{\mathbf{k}}_{mn} = \langle m\mathbf{k} \,|\, \hat{h} \,|\, n\mathbf{k} \rangle = \epsilon_{n\mathbf{k}} \delta_{mn}$ is the diagonal Hamiltonian matrix expressed in the original eigenstates. In the first line, the following relation for auxiliary Bloch states at $\mathbf{k}$ is used:

$$|\phi^{\text{aux}}_{n\mathbf{k}}\rangle = \underbrace{\frac{1}{N_{\mathbf{k}}} \sum_{\mathbf{R}} e^{i\mathbf{k}\cdot\mathbf{R}} \sum_{\mathbf{k}'} e^{-i\mathbf{k}'\cdot\mathbf{R}}}_{=1} \sum_{m} U^{\mathbf{k}'}_{mn} |\psi_{m\mathbf{k}'}\rangle = \sum_{m} U^{\mathbf{k}}_{mn} |\psi_{m\mathbf{k}}\rangle , \tag{2.2.34}$$

wherein the terms above the underbrace enforce $\mathbf{k} = \mathbf{k}'$, too. When a disentanglement method is employed, $U^{\mathbf{k}}$ needs to be replaced by $\mathcal{U}^{\mathbf{k}} U^{\mathbf{k}}$ in the relations above. The matrix elements $\langle m\mathbf{0} \,|\, \hat{h} \,|\, n\mathbf{R} \rangle^{\text{SC}}$ need to be tabulated only once after obtaining finalized MLWFs (more precisely, the set of $U^{\mathbf{k}}$ leading to MLWFs). Plugging the above expression for $\langle m\mathbf{0} \,|\, \hat{h} \,|\, n\mathbf{R} \rangle^{\text{SC}}$ into Eq. (2.2.31) yields the Hamiltonian matrix elements in the gauge of auxiliary states. Finally, interpolated Hamiltonian eigenstates $\psi_{n\mathbf{q}}(\mathbf{r})$ and eigenenergies $\epsilon_{n\mathbf{q}}$ at $\mathbf{q}$ can be accessed by a diagonalization of $H^{\mathbf{q},\text{aux}}_{mn}$, conveyed through eigenvectors $\mathcal{V}^{\mathbf{q}}$:

$$\begin{aligned}
[\mathcal{V}^{\mathbf{q}\dagger} H^{\mathbf{q},\text{aux}} \mathcal{V}^{\mathbf{q}}]_{mn} &\overset{!}{=} \epsilon_{n\mathbf{q}} \delta_{mn} \\
\Rightarrow \psi_{n\mathbf{q}}(\mathbf{r}) &= \sum_{m} \mathcal{V}^{\mathbf{q}}_{mn} \psi^{\text{aux}}_{m\mathbf{q}}(\mathbf{r}) .
\end{aligned} \tag{2.2.35}$$

Note, that, for points on the interpolation grid/path matching an original grid point $\mathbf{q} \in \{\mathbf{k}\}$, the original eigenenergies and eigenstates are reproduced (inside the inner energy window). The size of $H^{\mathbf{q},\mathrm{aux}}$ is $J \times J$ (with J the number of WFs and auxiliary Bloch states), which is much smaller than the Hamiltonian size when expanded in an LAPW+LO basis. Therefore, the diagonalization conducted for the interpolation from $\{\mathbf{k}\}$ onto $\{\mathbf{q}\}$ is inexpensive in comparison. The Fourier transforms and matrix multiplications required for the Wannier interpolation procedure are cheap, too. As such, the computational cost of a post-DFT Wannier interpolation is dominated by the cost of the construction of MLWFs.

Regarding Eq. (2.2.31), the number of matrix elements $\langle m\mathbf{0} \,|\, \hat{h} \,|\, n\mathbf{R}\rangle^{\mathrm{SC}}$ that can be calculated for a combination (m, n) is limited by the number of vectors $\mathbf{R}$ within the BvK SC, which is equal to $N_{\mathbf{k}}$ (see Sec. 2.1.5). From this fact, it becomes evident how MLWFs are an ideal candidate for the Slater-Koster interpolation scheme: Let the overlap between $|m\mathbf{0}\rangle$ and a WF at the boundary $\mathbf{R}'$ of a large BvK SC $|n\mathbf{R}'\rangle$ be significant. Then the corresponding term in the sum over $\mathbf{R}$ in Eq. (2.2.33) is lost, when a smaller SC in the same system (not containing $\mathbf{R}'$) is considered. Hence, by employing BvK boundary conditions, an error is always introduced in the Wannier interpolation. Through the optimization for MLWFs for a given SC size, a minimal overlap between WFs at different $\mathbf{R}$ is obtained (assuming a suitable localization criterion). Therefore, the contributions lost in the finite sum in Eq. (2.2.31) are also minimized.

The Wannier interpolation method does not require changes, when spinor MLWFs are employed, since the set of $\widetilde{U}^{\mathbf{k}}/\widetilde{\mathcal{U}}^{\mathbf{k}}\widetilde{U}^{\mathbf{k}}$ is just applied to Bloch spinors and no other matrix elements except $\widetilde{H}^{\mathbf{k}}_{mn} = \langle m\mathbf{k} \,|\, \hat{h}^{\mathrm{SV}} \,|\, n\mathbf{k}\rangle = \widetilde{\epsilon}_{n\mathbf{k}}\delta_{mn}$ are required in Eq. (2.2.33).

After the Wannier interpolated Hamiltonian eigenstates have been retrieved, arbitrary cell-periodic single-electron operators $\hat{o}$ with $\hat{o}(\mathbf{r}+\mathbf{R}) = \hat{o}(\mathbf{r})$ can be calculated using MLWFs [22]. The operator's expectation value in the gauge of auxiliary Bloch states is retrieved from MLWFs as

$$O^{\mathrm{aux},\mathbf{q}}_{mn} = \langle \phi^{\mathrm{aux}}_{m\mathbf{q}} \,|\, \hat{o} \,|\, \phi^{\mathrm{aux}}_{n\mathbf{q}} \rangle^{V_u} = \sum_{\mathbf{R}} e^{i\mathbf{q}\cdot\mathbf{R}} \langle m\mathbf{0} \,|\, \hat{o} \,|\, n\mathbf{R}\rangle \;, \tag{2.2.36}$$

and transformed into the Hamiltonian eigen-gauge $O^{H,\mathbf{q}}$ with the eigenvectors $\mathcal{V}^{\mathbf{q}}$ from Eq. (2.2.35) like:

$$O^{H,\mathbf{q}} = \mathcal{V}^{\mathbf{q}\dagger} O^{\mathrm{aux},\mathbf{q}} \mathcal{V}^{\mathbf{q}} \;. \tag{2.2.37}$$

The matrix elements $\langle m\mathbf{0} \,|\, \hat{o} \,|\, n\mathbf{R}\rangle$ are calculated by expressing Eq. (2.2.36) on the original grid $\{\mathbf{k}\}$ and applying the inverse Fourier transform, in analogy to the interpolation of the Hamiltonian Eq. (2.2.33).

3 Implementation

Within the scope of this work, a recent (spin-unpolarized) Wannier implementation [34, 38] within the full-potential all-electron LAPW+LO DFT code `exciting` [28, 44] is extended to the spin-polarized case. This chapter describes the implementation details that enable the creation of spin-polarized MLWFs, and the calculation of quantities in terms of these. The previous implementation enables the automatic construction of spin-polarized MLWFs with a variety of optimization and disentanglement methods. The extension featured by this work heavily relies on the existing code for the minimization of the spread functional Ω (Sec. 2.2.4), disentanglement methods, the calculation of the PW matrix Eq. (2.2.17), and Wannier interpolation (Sec. 2.2.7). It aims at keeping code refactoring minimal, so that existing code is reused where possible.

3.1 Planewave matrix

As described in Sec. 2.2.4 and Sec. 2.2.5, the PW matrix is the starting point for the minimization of $\Omega[\{U^{\mathbf{k}}\}]$ and disentanglement methods. Recollecting Eq. (2.2.19), $\widetilde{\mathcal{M}}^{\mathbf{k},\mathbf{b}}$ picks up a sum over spinor components when calculated in terms of spinor-valued wave functions. In practice, SV wave functions $|\widetilde{\psi}_{n\mathbf{k}}\rangle$ are re-expanded into FV orbitals via Eq. (2.1.26), and the latter re-expanded into the LAPW+LO basis $|\varphi_{\kappa\mathbf{k}}\rangle$ using Eq. (2.1.19):

$$\begin{aligned}
\widetilde{\psi}_{n\mathbf{k}}(\mathbf{r}) &= \sum_{\sigma=\alpha,\beta} \widetilde{\psi}_{n\mathbf{k}\sigma}(\mathbf{r})|\sigma\rangle \\
&= \sum_{\sigma=\alpha,\beta} \sum_{m} \widetilde{C}^{\sigma\mathbf{k}}_{mn} \psi_{m\mathbf{k}}(\mathbf{r})|\sigma\rangle \\
&= \sum_{\sigma=\alpha,\beta} \sum_{\kappa} \left[C^{\mathbf{k}}\widetilde{C}^{\sigma\mathbf{k}}\right]_{\kappa n} \varphi_{\kappa\mathbf{k}}(\mathbf{r})|\sigma\rangle \\
&= \sum_{\sigma=\alpha,\beta} \sum_{\kappa} \widetilde{D}^{\sigma\mathbf{k}}_{\kappa n} \varphi_{\kappa\mathbf{k}}(\mathbf{r})|\sigma\rangle
\end{aligned} \tag{3.1.1}$$

SV and FV eigenvectors matrices $\widetilde{C}^{\sigma\mathbf{k}}/C^{\mathbf{k}}$ are multiplied, defining

$$\widetilde{D}^{\sigma\mathbf{k}} \equiv C^{\mathbf{k}}\widetilde{C}^{\sigma\mathbf{k}} \tag{3.1.2}$$

as SV to LAPW+LO expansion coefficients of size $N_{\text{LAPW+LO}} \times N_s$ for each $\mathbf{k}$ and σ. The SV Bloch states expanded in the LAPW+LO basis are then plugged into the SV PW matrix expression Eq. (2.2.19):

$$\begin{aligned}
\widetilde{\mathcal{M}}^{\mathbf{k},\mathbf{b}}_{mn} &= \sum_{\sigma=\alpha,\beta} \langle \widetilde{\psi}_{m\mathbf{k}\sigma} \,|\, e^{-i\mathbf{b}\cdot\mathbf{r}} \,|\, \widetilde{\psi}_{n\mathbf{k}+\mathbf{b}\sigma} \rangle^{\text{SC}} \\
&= \sum_{\sigma=\alpha,\beta} \sum_{\kappa,\kappa'} \widetilde{D}^{\sigma\mathbf{k}*}_{m\kappa} \langle \varphi_{\kappa\mathbf{k}} \,|\, e^{-i\mathbf{b}\cdot\mathbf{r}} \,|\, \varphi_{\kappa'\mathbf{k}+\mathbf{b}} \rangle \widetilde{D}^{\sigma\mathbf{k}+\mathbf{b}}_{\kappa' n}
\end{aligned} \tag{3.1.3}$$

This expression allows for an easy adaptation of the previous implementation, which in practice calculates the PW matrix by re-expanding scalar orbitals into the LAPW+LO basis. Spinor components are added to LAPW+LO expansion coefficients and sums over spinor components to matrix-element integrals. For the practical computation, the PW matrix elements were previously split into IR and MT-region contributions ([34], Appendix A). Accordingly, SV-spinor component terms in Eq. (2.2.19) are divided as

$$\langle \widetilde{\psi}_{m\mathbf{k}\sigma} \,|\, e^{-i\mathbf{b}\cdot\mathbf{r}} \,|\, \widetilde{\psi}_{n\mathbf{k}+\mathbf{b}\sigma} \rangle = \langle \widetilde{\psi}_{m\mathbf{k}\sigma} \,|\, e^{-i\mathbf{b}\cdot\mathbf{r}} \,|\, \widetilde{\psi}_{n\mathbf{k}+\mathbf{b}\sigma} \rangle^{\text{IR}} + \langle \widetilde{\psi}_{m\mathbf{k}\sigma} \,|\, e^{-i\mathbf{b}\cdot\mathbf{r}} \,|\, \widetilde{\psi}_{n\mathbf{k}+\mathbf{b}\sigma} \rangle^{\text{MT}} \,, \tag{3.1.4}$$

with

$$|\widetilde{\psi}_{n\mathbf{k}\sigma}\rangle^{\mathrm{R}} = \begin{cases} \sum_{\mathbf{G}} \widetilde{D}^{\sigma\mathbf{k}}_{\mathbf{G}n} |\varphi_{\mathbf{G}+\mathbf{k}}\rangle^{\mathrm{MT}} + \sum_{L} \widetilde{D}^{\sigma\mathbf{k}}_{Ln} |\varphi_{L}\rangle^{\mathrm{MT}} & \mathrm{R} = \mathrm{MT} \\ \sum_{\mathbf{G}} \widetilde{D}^{\sigma\mathbf{k}}_{\mathbf{G}n} |\varphi_{\mathbf{G}+\mathbf{k}}\rangle^{\mathrm{IR}} & \mathrm{R} = \mathrm{IR}\,. \end{cases} \tag{3.1.5}$$

Above, the LAPW+LO basis functions $|\varphi_\kappa\rangle^{\mathrm{R}}$ are replaced by their expressions within MTs/IR from Sec. 2.1.7. Note that the expansion coefficients $\widetilde{D}^{\sigma\mathbf{k}}$ in region R pick up a spinor component, compared to the non-spinor coefficients $C^{\mathbf{k}}$ in the previous implementation. The spinor-adapted PW matrix elements can be used in the spread-functional minimization leading to MLWFs, without other changes to the Marzari-Vanderbilt framework. Correspondingly, the majority of the previous Wannier implementation can be reused for the construction of spin-polarized MLWFs.

3.2 Collinear spin-pure MLWFs

This subsection covers additions to the existing Wannier implementation in `exciting`, which enable the construction of collinear spin-pure MLWFs (Sec. 2.2.6). In the following, $\sigma = \uparrow, \downarrow$ labels the spin index of a quantity, and the collinear spinor wave functions are considered as scalar spin-pure wave functions by disregarding the zero component in their spinors (compare Sec. 2.1.9). The tilde over Bloch functions $\widetilde{\psi}^{\sigma}_{i\mathbf{k}}(\mathbf{r})$ again indicates that they are the result of an SV first-principles calculation, and σ is a superscript for the purpose of indicating, that the $\widetilde{\psi}^{\sigma}_{i\mathbf{k}}(\mathbf{r})$ are the full scalar Bloch functions, not just Bloch spinor components.

The existing Wannier implementation assumes the set of input Bloch states to be ordered in energy for setting up variables and calculating the original PW matrix. However, for a collinear first-principles calculation in `exciting`, input states come ordered in energy only within the spin-$\uparrow$ and -$\downarrow$ set, respectively. Therefore, for extending the existing Wannier implementation to the collinear spin-pure case, the two sets are joined and the resulting set is sorted in energy, in order to keep code refactoring minimal. After initial variables are set up, optionally, a collinear Wannier calculation can be triggered. Then, for the construction of spin-pure MLWFs, states are mixed only with others of the same spin during disentanglement and/or the total spread minimization (compare Sec. 2.2.6). This is realized in the following way: Let i index the joined set of states $\{\widetilde{\psi}_{i\mathbf{k}}(\mathbf{r})\}^{\mathrm{sorted}} = \underset{\widetilde{\epsilon}_{i\mathbf{k}}}{\mathrm{sort}}\{\widetilde{\psi}^{\uparrow}_{i\mathbf{k}}(\mathbf{r})\} \cup \{\widetilde{\psi}^{\downarrow}_{i\mathbf{k}}(\mathbf{r})\}$ sorted in energy $\widetilde{\epsilon}_{i\mathbf{k}}$, which are the result of a collinear SV-calculation at $\mathbf{k}$. Define a matrix $V^{\sigma\mathbf{k}}$ of dimension $\mathcal{J}_{\mathbf{k}} \times \mathcal{J}_{\sigma\mathbf{k}}$ that takes the block structure:

$$V^{\sigma\mathbf{k}} = \begin{bmatrix} V^{\sigma\mathbf{k},\mathrm{out}} & V^{\sigma\mathbf{k},\mathrm{in}} \end{bmatrix}, \tag{3.2.1}$$

where $\mathcal{J}_{\sigma\mathbf{k}}$ is the number of states with spin σ in the outer energy window at $\mathbf{k}$. This matrix mediates the extraction of two sets $\sigma = \uparrow, \downarrow$ of spin-pure states $\widetilde{\psi}^{\sigma}_{j\mathbf{k}}(\mathbf{r})$ from the joined, energy-ordered set $\{\widetilde{\psi}_{i\mathbf{k}}(\mathbf{r})\}^{\mathrm{sorted}}$ as

$$\widetilde{\psi}^{\sigma}_{j\mathbf{k}}(\mathbf{r}) = \sum_{i}^{\mathcal{J}_{\mathbf{k}}} V^{\sigma\mathbf{k}}_{ij} \widetilde{\psi}_{i\mathbf{k}}(\mathbf{r})\,. \tag{3.2.2}$$

A new index $j \in [1, \ldots, \mathcal{J}_{\sigma\mathbf{k}}]$ is now ordered such that it counts states contained in the outer-only window first (ordered in energy within), and states contained in the inner energy window (ordered in energy within) after, at each $\mathbf{k}$ in reciprocal space. The blocks in $V^{\sigma\mathbf{k}}$ mediate the extraction of states of spin σ contained in the outer-only energy window ($V^{\sigma\mathbf{k},\mathrm{out}}$) and inner energy window ($V^{\sigma\mathbf{k},\mathrm{in}}$), from the joined and sorted set $\{\widetilde{\psi}_{i\mathbf{k}}(\mathbf{r})\}^{\mathrm{sorted}}$. Each column of $V^{\sigma\mathbf{k},\mathrm{out}}/V^{\sigma\mathbf{k},\mathrm{in}}$ contains only one 1 with all other entries being 0, such that (i) a state of spin σ is picked and (ii) states are assigned to the respective energy window they are associated to, ordered in energy within. Fig. 2

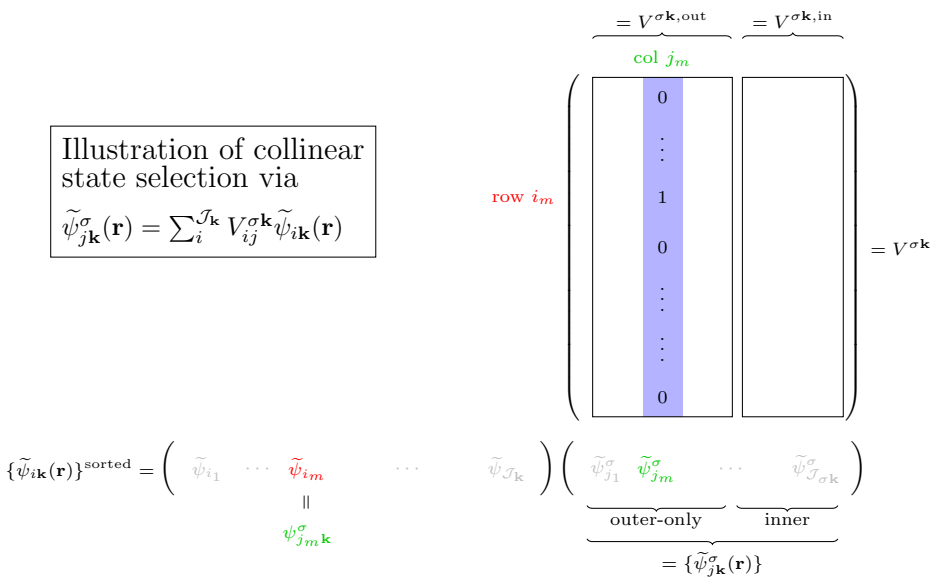

Figure 2: Illustration of Eq. (3.2.2). An example column j_m of $V^{\sigma\mathbf{k}}$, containing one entry of 1 in row i_m and all others 0, is marked in blue. The matrix $V^{\sigma\mathbf{k}}$ transforms the set $\{\widetilde{\psi}_{i\mathbf{k}}(\mathbf{r})\}^{\mathrm{sorted}}$ such that a spin-pure set $\{\widetilde{\psi}^{\sigma}_{j\mathbf{k}}(\mathbf{r})\}$ of states with spin $\sigma =\uparrow,\downarrow$ is picked from it and ordered, so that outer-only window states precede and inner window states follow.

illustrates the state selection process from the joined and sorted set of Bloch states $\{\widetilde{\psi}_{i\mathbf{k}}(\mathbf{r})\}^{\mathrm{sorted}}$ and the construction of $V^{\sigma\mathbf{k}}$. The spin information is retrieved by reversing the sorting.

The collinear disentanglement procedure rotates the extracted spin-pure states. Replacing original Bloch states with these in Eq. (2.2.20), like $\widetilde{\psi}_{n\mathbf{k}}(\mathbf{r}) \to \widetilde{\psi}^{\sigma}_{n\mathbf{k}}(\mathbf{r})$, the SMV disentanglement is expressed as

$$\begin{aligned} \widetilde{\Phi}^{\sigma}_{n\mathbf{k}}(\mathbf{r}) &= \sum_{j}^{\mathcal{J}_{\sigma\mathbf{k}}} \widetilde{\mathcal{U}}^{\sigma\mathbf{k}}_{jn} \widetilde{\psi}^{\sigma}_{j\mathbf{k}}(\mathbf{r}) \\ &= \sum_{i}^{\mathcal{J}_\mathbf{k}} \left[V^{\sigma\mathbf{k}} \widetilde{\mathcal{U}}^{\sigma\mathbf{k}} \right]_{in} \widetilde{\psi}_{i\mathbf{k}}(\mathbf{r}) \, . \end{aligned} \tag{3.2.3}$$

In the 2nd line, Eq. (3.2.2) is invoked, and a spin index is added to $\widetilde{\mathcal{U}}^{\sigma\mathbf{k}}$, yielding spin-pure disentangled subspaces spanned by the $\widetilde{\Phi}^{\sigma}_{m\mathbf{k}}(\mathbf{r})$. At this point, the calculation of MLWFs from two spin-pure sets of disentangled states proceeds by the minimization of $\Omega[\{\widetilde{U}^{\sigma\mathbf{k}}\}]$ via consecutive updates to the PW matrix $\widetilde{\mathcal{M}}^{\mathbf{k},\mathbf{b}}$ from Eq. (3.1.3). The introduction of $V^{\sigma\mathbf{k}}$ propagates into these updates (Eq. (2.2.21)):

$$\begin{aligned} (\widetilde{M}^{\sigma\mathbf{k},\mathbf{b}})^{\mathrm{col,dis}} &= (\widetilde{U}^{\sigma\mathbf{k}})^{\dagger} \langle \widetilde{\Phi}^{\sigma}_{\mathbf{k}} \,|\, e^{-i\mathbf{b}\cdot\mathbf{r}} \,|\, \widetilde{\Phi}^{\sigma}_{\mathbf{k}+\mathbf{b}} \rangle \widetilde{U}^{\sigma\mathbf{k}+\mathbf{b}} \\ &= (\widetilde{U}^{\sigma\mathbf{k}})^{\dagger} (\widetilde{\mathcal{U}}^{\sigma\mathbf{k}})^{\dagger} (V^{\sigma\mathbf{k}})^{\dagger} \widetilde{\mathcal{M}}^{\mathbf{k},\mathbf{b}} V^{\sigma\mathbf{k}+\mathbf{b}} \widetilde{\mathcal{U}}^{\sigma\mathbf{k}+\mathbf{b}} \widetilde{U}^{\sigma\mathbf{k}+\mathbf{b}} \, , \end{aligned} \tag{3.2.4}$$

where $\widetilde{U}^{\sigma\mathbf{k}}$, $\widetilde{\mathcal{U}}^{\sigma\mathbf{k}}$, and $(\widetilde{M}^{\sigma\mathbf{k},\mathbf{b}})^{\mathrm{col,dis}}$ pick up a spin index. $(\widetilde{M}^{\sigma\mathbf{k},\mathbf{b}})^{\mathrm{col,dis}}$ is the PW matrix employing energy disentanglement for the construction of spin-pure MLWFs, in the context of a collinear spin-treatment. The original PW matrix $\widetilde{\mathcal{M}}^{\mathbf{k},\mathbf{b}}$ is calculated from the energy-sorted joined set of original Bloch states $\{\widetilde{\psi}_{i\mathbf{k}}(\mathbf{r})\}^{\mathrm{sorted}}$. For the full disentanglement method, $\widetilde{\mathcal{U}}^{\sigma\mathbf{k}}\widetilde{U}^{\sigma\mathbf{k}}$ applies directly to the extracted spin-pure states in Eq. (3.2.2). The case of isolated bands is retrieved by setting $\mathcal{U}^{\sigma\mathbf{k}} = \mathbf{I}_{\mathcal{J}_{\sigma\mathbf{k}}}$.

In the practical implementation, the (collinear) spin-pure states $\widetilde{\psi}^{\sigma}_{j\mathbf{k}}$ are considered as the starting point of the SMV disentanglement minimizing $\Omega_I[\{\widetilde{\mathcal{U}}^{\sigma\mathbf{k}}\}]$ with a consecutive minimization of

$\Omega[\{\widetilde{U}^{\sigma\mathbf{k}}\}]$, or the joint minimization of $\Omega[\{\widetilde{\mathcal{U}}^{\sigma\mathbf{k}}\widetilde{U}^{\sigma\mathbf{k}}\}]$ within the full disentanglement method. All rotations $\widetilde{\mathcal{U}}^{\sigma\mathbf{k}}$ or $\widetilde{U}^{\sigma\mathbf{k}}$ apply to the $\widetilde{\psi}^{\sigma}_{j\mathbf{k}}$. The contributions to Ω and its gradient are calculated starting from $\widetilde{\mathcal{M}}^{\sigma\mathbf{k},\mathbf{b}} \equiv (V^{\sigma\mathbf{k}})^{\dagger}\widetilde{\mathcal{M}}^{\mathbf{k},\mathbf{b}}V^{\sigma\mathbf{k}+\mathbf{b}}$, which are updated with the $\widetilde{\mathcal{U}}^{\sigma\mathbf{k}}/\widetilde{U}^{\sigma\mathbf{k}}$ (SMV) or $\widetilde{\mathcal{U}}^{\sigma\mathbf{k}}\widetilde{U}^{\sigma\mathbf{k}}$ (full). After the minimization of the spread functional is converged, rotated states that lead to MLWFs are expressed in terms of the initial sorted set of original Bloch states by incorporating the state selection by $V^{\sigma\mathbf{k}}$ into the energy disentanglement like $\widetilde{\mathcal{U}}^{\sigma\mathbf{k}} \to V^{\sigma\mathbf{k}}\widetilde{\mathcal{U}}^{\sigma\mathbf{k}}$. Finalized collinear spin-pure MLWFs of spin σ come out as:

$$\widetilde{w}^{\sigma}_{n\mathbf{R}}(\mathbf{r}) = \frac{1}{N_{\mathbf{k}}}\sum_{\mathbf{k}} e^{-i\mathbf{k}\cdot\mathbf{R}}\left[\sum_{i}^{\mathcal{J}_{\mathbf{k}}}\left[\widetilde{\mathcal{U}}^{\sigma\mathbf{k}}\widetilde{U}^{\sigma\mathbf{k}}\right]_{in}\widetilde{\psi}_{i\mathbf{k}}(\mathbf{r})\right] \text{ with } \widetilde{\psi}_{i\mathbf{k}}(\mathbf{r}) \in \{\widetilde{\psi}_{i\mathbf{k}}(\mathbf{r})\}^{\text{sorted}} \tag{3.2.5}$$

3.3 Construction of spin-polarized MLWFs – Implementation summary

A workflow graph summarizing the construction of spin-polarized MLWFs is presented in Fig. 3. This graph is based on the original workflow graph in [34], which illustrates the construction of (spin-unpolarized) MLWFs with the previous Wannier implementation. Tab. 1 summarizes the states utilized at different workflow steps and compares the calculation of collinear spin-pure to non-collinear spinor MLWFs. The only difference between the two options lies in the creation of spin-pure initial states and the introduction of a spin-index to transformation matrices for the collinear case.

Quantity	spinor case	spin-pure case
original Bloch spinors	$\widetilde{\psi}_{n\mathbf{k}}(\mathbf{r})$	$\widetilde{\psi}_{n\mathbf{k}}(\mathbf{r})$
spin-pure ordered states	n.a.	$\widetilde{\psi}^{\sigma}_{n\mathbf{k}}(\mathbf{r}) = \sum_{n}^{\mathcal{J}_{\mathbf{k}}} V^{\sigma\mathbf{k}}_{mn}\widetilde{\psi}_{m\mathbf{k}}(\mathbf{r})$
disentangled states (SMV)	$\widetilde{\Phi}_{n\mathbf{k}}(\mathbf{r}) = \sum_{m}^{\mathcal{J}_{\mathbf{k}}} \widetilde{\mathcal{U}}^{\mathbf{k}}_{mn}\widetilde{\psi}_{n\mathbf{k}}(\mathbf{r})$	$\widetilde{\Phi}^{\sigma}_{n\mathbf{k}}(\mathbf{r}) = \sum_{m}^{\mathcal{J}_{\sigma\mathbf{k}}} \widetilde{\mathcal{U}}^{\sigma\mathbf{k}}_{mn}\widetilde{\psi}^{\sigma}_{m\mathbf{k}}(\mathbf{r})$
disentangled+rotated states	$\widetilde{\phi}_{n\mathbf{k}}(\mathbf{r}) = \sum_{m}^{J} \widetilde{U}^{\mathbf{k}}_{mn}\widetilde{\Phi}_{m\mathbf{k}}(\mathbf{r})$ (SMV)	$\widetilde{\phi}^{\sigma}_{n\mathbf{k}}(\mathbf{r}) = \sum_{m}^{J_{\sigma}} \widetilde{U}^{\sigma\mathbf{k}}_{mn}\widetilde{\Phi}^{\sigma}_{m\mathbf{k}}(\mathbf{r})$ (SMV)
	$\widetilde{\phi}_{n\mathbf{k}}(\mathbf{r}) = \sum_{i}^{\mathcal{J}} [\widetilde{\mathcal{U}}^{\mathbf{k}}\widetilde{U}^{\mathbf{k}}]_{in}\widetilde{\psi}_{i\mathbf{k}}(\mathbf{r})$ (full)	$\widetilde{\phi}^{\sigma}_{n\mathbf{k}}(\mathbf{r}) = \sum_{m}^{\mathcal{J}_{\sigma\mathbf{k}}} [\widetilde{\mathcal{U}}^{\sigma\mathbf{k}}\widetilde{U}^{\sigma\mathbf{k}}]_{mn}\widetilde{\psi}^{\sigma}_{m\mathbf{k}}(\mathbf{r})$ (full)
MLWFs	$\widetilde{w}_{n\mathbf{R}}(\mathbf{r}) = \frac{1}{N_{\mathbf{k}}}\sum_{\mathbf{k}} e^{-i\mathbf{k}\cdot\mathbf{R}}\phi_{n\mathbf{k}}(\mathbf{r})$	$\widetilde{w}^{\sigma}_{n\mathbf{R}}(\mathbf{r}) = \frac{1}{N_{\mathbf{k}}}\sum_{\mathbf{k}} e^{-i\mathbf{k}\cdot\mathbf{R}}\phi^{\sigma}_{n\mathbf{k}}(\mathbf{r})$

Table 1: Comparison between the construction of *spinor* and *spin-pure* MLWFs. The calculation of the states utilized during different workflow steps is presented.

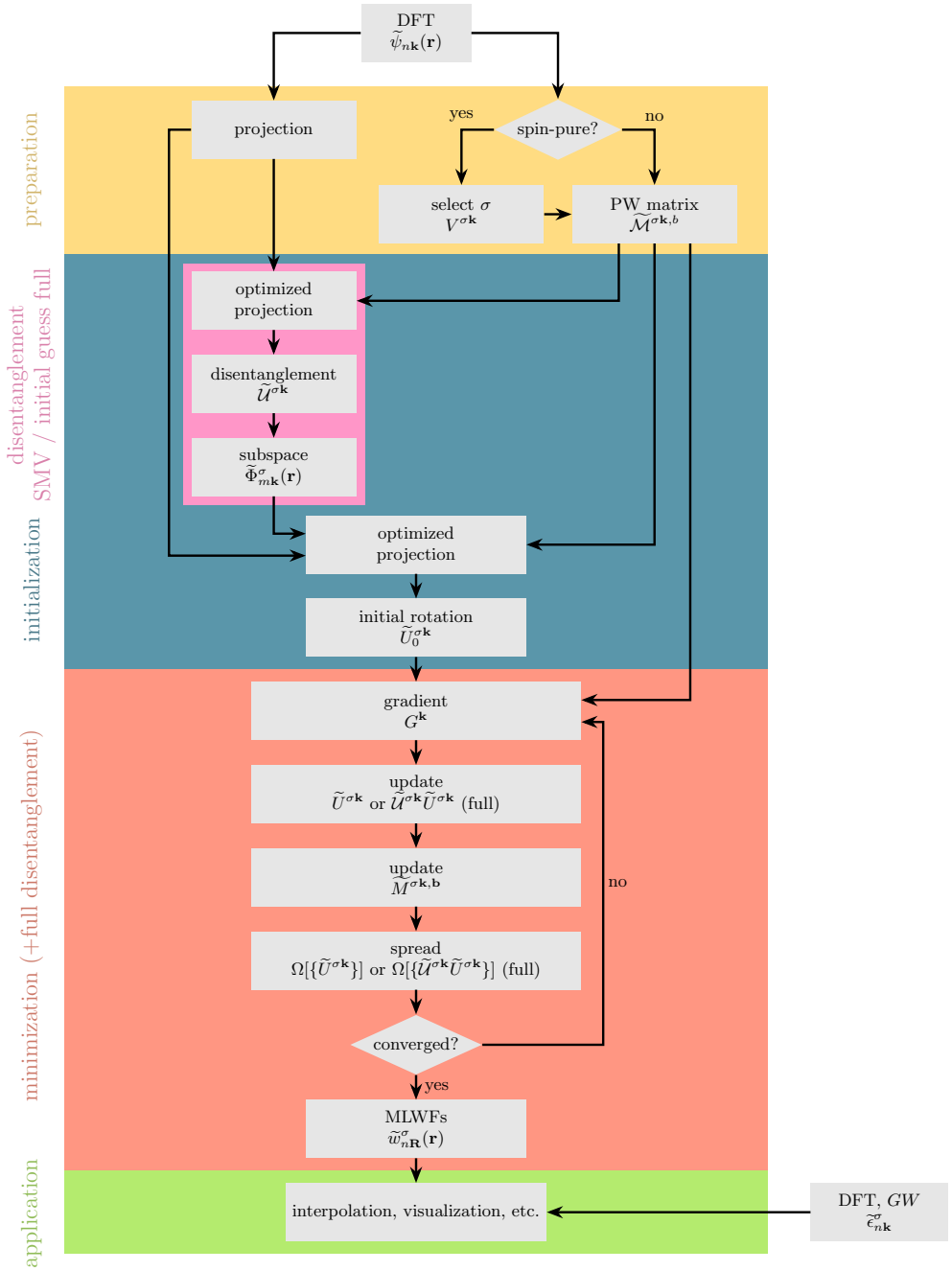

Figure 3: Workflow for the construction of spinor MLWFs or spin-pure MLWFs. The spin index $\sigma = \uparrow, \downarrow$ is only required for the construction of spin-pure MLWFs and dropped for the construction of spinor MLWFs.

3.4 Wannier interpolation

3.4.1 Band structure and density of states

In the previous `exciting` Wannier implementation, Hamiltonian eigenenergies can be interpolated according to the procedure in Sec. 2.2.7, also providing access to interpolated eigenstates. From the eigenenergies, an interpolated band structure can be obtained, and a density of states (DOS) can be calculated. The necessary changes to the previous implementation for a Wannier starting from spinor MLWFs are mostly trivial as stated in Sec. 2.2.7, except for some quantities.

For the general non-collinear spinor case, the energy interpolation procedure laid out in Sec. 2.2.7 needs no adaptation, since the spinor character of original Bloch states is contained in the original SV Hamiltonian matrix elements $\widetilde{H}^{\mathbf{k}}$ during the construction of interpolated states. For an SV calculation, $\widetilde{H}^{\mathbf{k}}$ is again diagonal in the basis of SV states. When employing collinear spin-pure MLWFs, the transformation of $\widetilde{H}^{\mathbf{k}}$ in Eq. (2.2.33) can be conducted separately for states of spin up/down. This is done by replacing the transforms by their corresponding final collinear transforms in Eq. (3.2.5), such that $\mathcal{U}^{\mathbf{k}}U^{\mathbf{k}} \to \widetilde{\mathcal{U}}^{\sigma\mathbf{k}}\widetilde{U}^{\sigma\mathbf{k}}$ in Eq. (2.2.33). The resulting interpolated eigenvalues $\widetilde{\epsilon}^{\sigma}_{i\mathbf{q}}$ allow for a spin-resolved interpretation of interpolated band structures.

Calculating eigenvalues on a fine interpolation grid $\mathbf{q}$ also provides access to a more accurate DOS. The DOS is defined as

$$D(E) = \frac{1}{N_{\mathbf{q}}} \sum_{\mathbf{q}} \sum_{i} \delta(E - \epsilon_{i\mathbf{q}}) \, , \tag{3.4.1}$$

and needs no adaptation for the non-collinear case, for the same reasons as above. Interpolated SV eigenvalues $\widetilde{\epsilon}_{i\mathbf{q}}$ are simply used in Eq. (3.4.1). For the case of collinear spin-pure MLWFs, the DOS may again be calculated from the two sets of $\widetilde{\epsilon}^{\sigma}_{i\mathbf{q}}$ separately. A spin-resolved DOS $\widetilde{D}^{\sigma}(E)$ obtained from eigenenergies on a fine grid $\{\mathbf{q}\}$ is the result.

The previous implementation also allowed for the calculation of band derivatives and effective masses based on the Wannier interpolation scheme. Using MLWFs, an analytical expression for band derivatives can be derived, therefore not relying on finite-difference approximations [27]. This is due to the Wannier interpolated Hamiltonian $H^{\mathbf{q},\mathrm{aux}}$ depending on $\mathbf{q}$ only in the Fourier phase factor (compare Eq. (2.2.31)). As such, effective masses at arbitrary $\mathbf{q}$ can be calculated analytically, based on the Wannier interpolation scheme. It is further possible to retrieve band extrema by an optimization using the analytical band derivatives. The previous implementation featured this option, and the calculation of effective masses [38]. No changes for the accommodation of spinor-valued MLWFs are necessary for calculating these quantities, for the reasons described above. Again, quantities can be calculated separately for $\sigma = \uparrow / \downarrow$ from collinear spin-pure MLWFs.

3.4.2 Band characters and partial densities of states

In the previous implementation, orbital-resolved band characters or partial contributions of certain l-channels to the density of states can be calculated. To adapt these features to the spin-polarized MLWFs case, some minor additions are necessary. In the non-spinor case, band characters can be calculated by expanding original KS orbitals $\psi_{n\mathbf{k}}(\mathbf{r})$ in the MTs of atom α into radial functions and spherical harmonics [34] (which is straightforward in the LAPW+LO framework). These wave functions can be interpolated according to the procedure described in Sec. 2.2.7. Comparing the spherical harmonics expansion of non-spinor KS orbitals on the original grid $\{\mathbf{k}\}$,

$$\psi^{\alpha}_{n\mathbf{k}}(\mathbf{r}) = \sum_{l} \sum_{m=-l}^{l} \varphi^{\alpha}_{n,lm,\mathbf{k}}(r_\alpha) Y_{lm}(\mathbf{r}_\alpha) \, , \tag{3.4.2}$$

with an expansion of spinor orbitals carried out for spinor components $\sigma = \alpha, \beta$ separately as

$$\begin{aligned}\widetilde{\psi}^{\alpha}_{n\mathbf{k}\sigma}(\mathbf{r}) &= \sum_{l}\sum_{m=-l}^{l} \varphi^{\alpha\sigma}_{n,lm,\mathbf{k}}(r_\alpha) Y_{lm}(\mathbf{r}_\alpha) \\ \widetilde{\psi}^{\alpha}_{n\mathbf{k}}(\mathbf{r}) &= \sum_{\sigma=\alpha,\beta} \widetilde{\psi}^{\alpha}_{n\mathbf{k}\sigma}(\mathbf{r})|\sigma\rangle,\end{aligned} \tag{3.4.3}$$

radial expansion functions $\varphi^{\alpha\sigma}_{n,lm,\mathbf{k}}(r_\alpha)$ ought to carry a spinor component index σ compared to the non-spinor expansion. In the following, the derivation of band characters in terms of MLWFs from [34] is adapted for the spinor MLWFs case. While closely following the conceptual steps of this work, the necessary changes for the spinor adaptation are marked in green. The non-spinor case from [34] is retrieved by removing expressions/their parts in green, or replacing them with their non-SV equivalent.

Band characters result from considering the partial electron density contribution $n_{n\mathbf{k}}(\mathbf{r})$ of state n at $\mathbf{k}$, in the MT sphere α:

$$\begin{aligned}\int_{\mathrm{MT}_\alpha} \mathrm{d}\mathbf{r}\, n_{n\mathbf{k}}(\mathbf{r}) &= \int_{\mathrm{MT}_\alpha} \mathrm{d}\mathbf{r} |\widetilde{\psi}^{\alpha}_{n\mathbf{k}}(\mathbf{r})|^2 \\ &= \sum_{l} \sum_{\sigma=\alpha,\beta} \sum_{m=-l}^{l} \int_0^{R_\alpha} \mathrm{d}r\, r^2 |\varphi^{\alpha\sigma}_{n,lm,\mathbf{k}}(r_\alpha)|^2 \\ &= \sum_{l} b^{\alpha}_{nl\mathbf{k}}\,.\end{aligned} \tag{3.4.4}$$

The band character $b^{\alpha}_{nl\mathbf{k}}$ represents the contribution of an orbital component l for a KS electron with band index n, at reciprocal space point $\mathbf{k}$, in MT α to the total density. Compared to the previous non-spinor implementation, a sum over spinor components of the radial expansion functions is introduced. Radial expansion functions $\varphi^{\alpha\sigma}_{n,lm,\mathbf{k}}(r_\alpha)$ are easily identified, when expanding spinor-components of SV KS orbitals $\widetilde{\psi}^{\alpha}_{n\mathbf{k}\sigma}(\mathbf{r})$ back into the LAPW+LO basis in MTs α via Eq. (3.1.1):

$$\widetilde{\psi}^{\alpha}_{n\mathbf{k}\sigma}(\mathbf{r}) = \sum_{lm} \underbrace{\left[\sum_{\mathbf{G}} \widetilde{D}^{\sigma\mathbf{k}}_{\mathbf{G}n} \sum_{\xi} A^{\xi,\mathbf{G}+\mathbf{k}}_{lm\alpha} u^{\xi}_{l\alpha}(r_\alpha;\epsilon_{l\alpha}) + \sum_{L} \delta_{\alpha\alpha_L}\delta_{ll_L}\delta_{mm_L} \widetilde{D}^{\sigma\mathbf{k}}_{Ln} f^{L}_{l_L}(r_\alpha)\right]}_{=\varphi^{\alpha\sigma}_{n,lm,\mathbf{k}}(r_\alpha)} Y_{lm}(\mathbf{r}_\alpha)\,, \tag{3.4.5}$$

wherein the sum over LO radial derivative orders ξ_L in Eq. (2.1.20) is compactly expressed by defining

$$f^{L}_{l_L}(r_\alpha) \equiv \sum_{\xi_L} a^{\xi_L}_{L} u^{\xi_L}_{l\alpha}(r_\alpha, \epsilon_{l\alpha})\,. \tag{3.4.6}$$

The radial expansion functions $\varphi^{\alpha\sigma}_{n,lm,\mathbf{k}}(r_\alpha)$ are rewritten like

$$\varphi^{\alpha\sigma}_{n,lm,\mathbf{k}}(r_\alpha) \equiv \sum_{\lambda} B^{\alpha\mathbf{k}\sigma}_{n,lm,\lambda} g^{\alpha}_{\lambda l}(r_\alpha)\,. \tag{3.4.7}$$

The index λ counts either LAPW matching orders ξ or LO indices L. The radial expansion coefficients $B^{\alpha,\mathbf{k}\sigma}_{n,lm,\lambda}$ depend on λ as

$$B^{\alpha\mathbf{k}\sigma}_{n,lm,\lambda} = \begin{cases} \sum_{\mathbf{G}} A^{\xi,\mathbf{G}+\mathbf{k}}_{lm\alpha} \widetilde{D}^{\sigma\mathbf{k}}_{\mathbf{G}n} & \lambda = \xi \\ \delta_{\alpha\alpha_L}\delta_{ll_L}\delta_{mm_L} \widetilde{D}^{\sigma\mathbf{k}}_{Ln} & \lambda = L. \end{cases} \tag{3.4.8}$$

Further in Eq. (3.4.7), $g^{\alpha}_{\lambda l}(r_\alpha)$ is either an LAPW radial function $u^{\xi}_{l\alpha}(r_\alpha;\epsilon_{l\alpha})$ for $\lambda=\xi$, or $f^{L}_{l_L}(\mathbf{r})$ for $\lambda=L$. The non-spinor case is retrieved when replacing $\widetilde{D}^{\sigma\mathbf{k}}_{\kappa n}$ by LAPW+LO eigenvectors $C^{\mathbf{k}}_{\kappa n}$ from Eq. (2.1.19). By expressing radial expansion functions in Eq. (3.4.4) using Eq. (3.4.7), band characters result as

$$b^{\alpha}_{nl\mathbf{k}} = \sum_{\sigma=\alpha,\beta}\sum_{m=-l}^{l}\sum_{\lambda,\lambda'}(B^{\alpha\mathbf{k}\sigma}_{n,lm,\lambda})^{*}B^{\alpha\mathbf{k}\sigma}_{n,lm,\lambda'}\int_0^{R_\alpha}\mathrm{d}r\, r^2 g^{\alpha}_{\lambda l}(r_\alpha)g^{\alpha}_{\lambda' l}(r_\alpha). \tag{3.4.9}$$

In this expression, the $\mathbf{k}$-independent radial integrals are to be evaluated once and for all. The final band characters then result from linear algebra involving the radial expansion coefficients $B^{\alpha\mathbf{k}\sigma}_{n,lm,\lambda'}$. As Wannier interpolated band characters on a grid $\{\mathbf{q}\}$ are of interest, the combined transformations necessary for interpolating KS wave functions (see Sec. 2.2.7) are applied to the radial functions $\varphi^{\alpha\sigma}_{n,lm,\mathbf{k}}(r_\alpha)$ on the original grid $\{\mathbf{k}\}$ [34], yielding

$$\varphi^{\alpha\sigma}_{n,lm,\mathbf{q}}(r_\alpha) = \sum_{\lambda}\sum_{n'}\mathcal{V}^{\mathbf{q}}_{n'n}\sum_{\mathbf{R}}e^{i\mathbf{q}\cdot\mathbf{R}}\frac{1}{N_k}\sum_{\mathbf{k}}e^{-i\mathbf{k}\cdot\mathbf{R}}\sum_{j}[\widetilde{\mathcal{U}}^{\mathbf{k}}\widetilde{U}^{\mathbf{k}}]_{jn'}B^{\alpha\mathbf{k}\sigma}_{j,lm,\lambda}g^{\alpha}_{\lambda}(r_\alpha) \tag{3.4.10}$$

Though this expression for the radial expansion functions is lengthy, it only involves linear algebra and discrete Fourier transforms, giving easy access to all $\varphi^{\alpha\sigma}_{n,lm,\mathbf{q}}(r_\alpha)$ at $\mathbf{q}$.

In practice, the interpolation of band characters starts by first calculating all $B^{\alpha\mathbf{k}\sigma}_{n,lm,\lambda}$ according to Eq. (3.4.8). After that, the original procedure described in [34] is applied unaltered. The interpolated coefficients $B^{\alpha\mathbf{q}\sigma}_{m,lm,\lambda}$ can be extracted from Eq. (3.4.10). With these, the interpolated band character at $\mathbf{q}$ is obtained by Eq. (3.4.9).

Given all ingredients for the calculation of spinor-adapted, interpolated band characters $b^{\alpha}_{nl\mathbf{q}}$ via spinor-valued MLWFs, the calculation of the *partial density of states* (PDOS) becomes straightforward. The PDOS describes the contributions to the total DOS of each l-channel, from an MT sphere associated with atom α. The l-channel resolved PDOS $D^{\alpha}_{l}(E)$ associated to atom α is defined via l-resolved band characters by

$$D^{\alpha}_{l}(E) = \frac{1}{N_{\mathbf{q}}}\sum_{\mathbf{q}}\sum_{i}b^{\alpha}_{il\mathbf{q}}\delta(E-\epsilon_{i\mathbf{q}})\,, \tag{3.4.11}$$

and can be calculated spin-polarized using the previous implementation, but with spinor-adapted band characters as input. Again, when employing collinear spin-pure MLWFs, the extended implementation allows for the calculation of an l-resolved PDOS and l-resolved band characters separately in the spin-up/down channel.

4 Application

4.1 Spin-orbit splitting in GaAs

As a simple test case for the present spinor-adapted Wannier implementation, bulk gallium arsenide (GaAs), including SO coupling, is considered. GaAs exhibits a pronounced splitting of valence bands near the Fermi level around the Γ point due to SO effects. It is a useful material for comparing the construction of spinor MLWFs to the spin-unpolarized case, since the band structure away from Γ is very similar in both cases. A DFT calculation for a lattice constant of $10.683\,a_0$ is performed with `exciting` employing an LAPW+LO basis determined by $R_{\mathrm{MT,min}} \cdot |G+k|_{\max} = 9.0$, corresponding to a planewave cut-off of $|G|_{\max} = 16.0\,a_0^{-1}$ and using a $12\times12\times12$ Monkhorst–Pack $\mathbf{k}$-grid [9]. Exchange-correlation effects are modeled by the semilocal generalized-gradient approximation (GGA) PBE functional[6] [13]. SO coupling is considered, and a number of $N^{\mathrm{FV}}_{\mathrm{unocc}} = 200$ unoccupied states are included in order to converge the mean energy difference of the valence band splitting due to SO effects and the total energy in terms of the SV treatment.

14 MLWFs are then generated based on this DFT calculation using the converged FV- and SV-basis by employing the full disentanglement method. The inner energy window is chosen as $[-8.16, 2.72]$ eV and the outer energy window as $[-8.16, 13.61]$ eV (relative to the Fermi level). The inner window fully encompasses the first two conduction bands and the six highest valence bands. The spread functional is considered minimized when the norm of its gradient $G = \sqrt{\sum_{\mathbf{k}} ||\nabla_{U^{\mathbf{k}}}\Omega[\{U^{\mathbf{k}}\}]||^2}$ reaches a value of $10^{-6}\,a_0^2$.

4.1.1 Wannier band interpolation

The GaAs band structure is calculated with DFT, and also Wannier interpolated, in each case with the same band path sampling, and based on the $12\times12\times12$ $\mathbf{k}$-grid first-principles DFT calculation from the previous section. Fig. 4 compares the DFT band structure with the Wannier-interpolated bands. The interpolated bands are displayed with half-open empty circles. The two different symbols for Wannier bands allow for the distinction of two (different) spinor-associated bands, which might be pairwise close in energy, at some point in the BZ. At these points, (i) the difference in the impact of SO coupling on the respective bands might be small, or (ii) they might be energy degenerate (up to numerical precision) due to symmetries. In a spin-unpolarized calculation, such a band pair may be treated as a single spin-degenerate band. In the inner energy window, the Wannier bands are in excellent agreement with the DFT reference. Outside of the inner window, the interpolated bands are not expected to reproduce the DFT equivalents exactly, and band features may be unphysical (compared to the DFT reference). From panel b), it is evident that the spinor Wannier interpolation accurately captures the SO-splitting of the highest valence bands. In a spin-unpolarized calculation for GaAs, the three highest valence bands would be threefold-degenerate at Γ. For the calculation considering SO coupling presented here, this degeneracy is lifted and the highest valence bands split into a $j = 3/2$ quartet (light- and heavy-hole bands) and $j = 1/2$ doublet (split-off bands). Away from Γ, the 6 highest valence bands and the first two conduction bands remain almost pairwise degenerate. The Dresselhaus-splitting of bands due to the bulk inversion asymmetry of the zinc-blende structure is more prominent only between Γ and K. The successful capture of the mentioned effects hints at the robustness of the Wannier interpolation scheme for the spinor case. This is to be expected, since the interpolation procedure itself did not need any adaptation for the incorporation of spinor wave functions.

[6] The GGA PBE functional realizes a non-collinear spin treatment by the "locally collinear approach" [40] (compare Sec. 2.1.9)

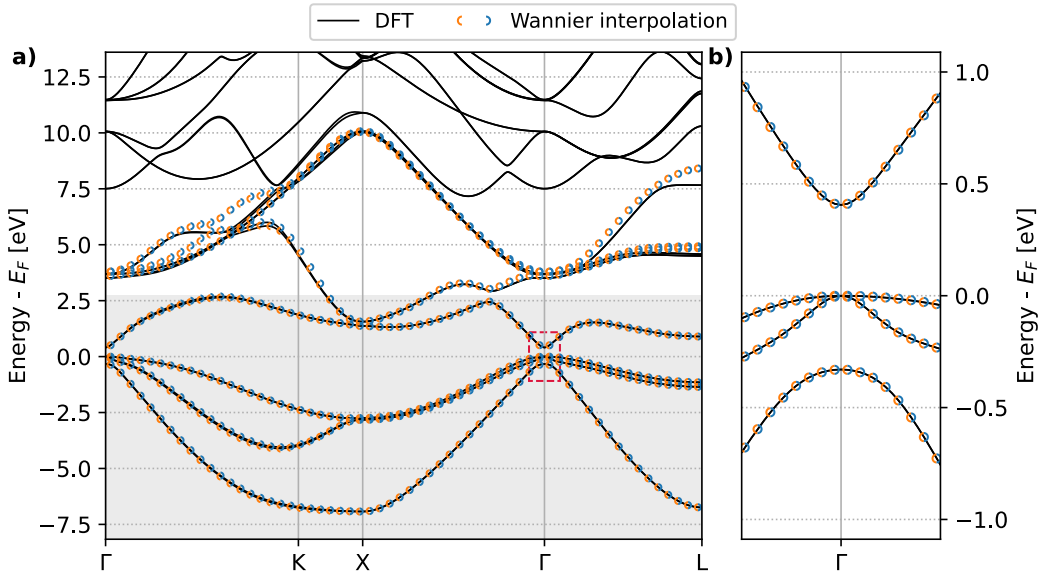

Figure 4: Bulk GaAs band structure obtained from DFT (solid lines) and Wannier interpolation (half-open circles). The blue and orange symbols allow for distinguishing two different spinor-associated Wannier bands, which are close in energy at some point in the BZ. Panel a) displays all interpolated Wannier bands. The inner disentanglement window is indicated by the gray area. Panel b) zooms into the band-gap area (dashed red outline in panel a). The SO splitting of valence bands at the Γ point is correctly reproduced by Wannier interpolation.

Next, the spin-polarized Wannier interpolation is directly compared to the previous spin-unpolarized implementation for the example of bulk GaAs. For this purpose, in addition to the spin-polarized run considering SO effects, MLWFs are calculated from a spin-unpolarized DFT calculation with the same $12 \times 12 \times 12$ **k**-sampling. MLWFs are constructed employing the full disentanglement method, choosing the same energy windows as before, with a similar convergence cut-off of $10^{-6}\ a_0^2$ for the spread-functional minimization. The spin-unpolarized band structure is calculated with DFT and Wannier-interpolated based on the same first-principles DFT calculation.

In order to compare the accuracy to the previous implementation, the root-mean-square error (RMSE) per band is calculated with a band path sampling of 600 points **q**:

$$\delta_n^{\mathrm{RMSE}} = \sqrt{\frac{1}{N_{\mathbf{q}}} \sum_{\mathbf{q}} (\epsilon_{n\mathbf{q}}^{\mathrm{DFT}} - \epsilon_{n\mathbf{q}}^{\mathrm{W}})^2}, \tag{4.1.1}$$

where $\epsilon_{n\mathbf{q}}^{\mathrm{W}}$ are the Wannier-interpolated energies and $\epsilon_{n\mathbf{q}}^{\mathrm{DFT}}$ are the DFT values. RMSEs are

RMSE per band [meV]			
band (band pair)	spin-unpolarized	spin-polarized band 1	spin-polarized band 2
1	2.449	2.256	2.222
2	1.328	0.821	1.080
3	1.684	1.892	1.890
4	7.171	7.523	7.244

Table 2: Root-mean-square error (RMSE) of Wannier interpolated band energies compared to DFT bands in GaAs, for a spin-unpolarized calculation and spin-polarized calculation including SO coupling. The RMSE for the 3 (6) highest valence bands 1-3 and the lowest conduction band(s) 4 are shown. All bands are fully contained within the inner disentanglement window throughout the BZ.

calculated only for bands fully contained in the inner energy window throughout the BZ. These are the 3 (6) highest valence bands and the lowest (lowest 2) conduction bands for the spin-unpolarized run (spin-polarized run including SO coupling). Tab. 2 compares the RMSE results. Over both runs, RMSEs are between 0.8 meV and 7.6 meV and as such quite small. In each run, the RMSE is up ≈ 4 (≈ 9.3) times larger for the conduction band (pair) (4), than for the valence bands (1-3) in both runs. This behavior is expected for Wannier-interpolated bands at the inner window edge, when they hybridize with bands from the outer-only window. All RMSE values of spin-polarized results are of similar magnitude compared to the spin-unpolarized ones. This further supports the robustness of the Wannier interpolation scheme for the spinor adaptation.

4.1.2 Convergence of the spread functional

While the quality of the Wannier interpolation of bands remains comparable between the previous and the new extended implementation, there is a noticeable difference in the convergence behavior of the spread functional during the construction of spin-polarized MLWFs for GaAs. For a reliable comparison, all calculations have been carried out on the same machine (AMD Ryzen 7 5800H CPU and 16 Gb of DDR4 RAM) using 8 OMP threads.

For the spin-unpolarized run, the minimization of the spread functional $\Omega[\{U^{\mathbf{k}}\}$ post-disentanglement converges in 686 iterations (48.3 s run-time). By contrast, the spin-polarized run requires 16 692 iterations with a total run time of 5187.8 s to reach the same gradient norm cut-off. The average run-times per iteration, t_{it} = total run-time/# iterations, are 70.4 ms and 310.8 ms, respectively, differing by a factor of ≈ 4.4. This indicates that the scaling of the average run-time remains roughly quadratic with the size of the unitary mixing matrices $U^{\mathbf{k}}$ at each $\mathbf{k}$ (two spinor states for every spin-degenerate spin-unpolarized state). Thus, the spinor nature of the underlying wave functions has only a small impact on the computational cost of a single iteration. The total run-time is, however, $\approx$ 106 times larger for the spin-polarized run, since

Figure 5: Convergence behavior of the $\Omega[\{\mathcal{U}^{\mathbf{k}}U^{\mathbf{k}}\}]$ minimization for bulk GaAs, employing the full-disentanglement method. Panel a) displays the norm of gradients to the total spread at different iterations during minimization for the spin-polarized run (orange) and spin-unpolarized run (black). Panel c) displays the gradient norm at the first 1200 iterations (gray area in a). Panel b) shows $(\Omega - \Omega_{\text{min}})/\Omega_{\text{min}}$ at different iterations (log scale) for the spin-polarized and unpolarized run, respectively.

RMSE per band [meV]				
	cut-off $10^{-5}\,a_0^2$		cut-off $10^{-6}\,a_0^2$	
band pair	band 1	band 2	band 1	band 2
1	2.161	2.159	2.256	2.222
2	0.759	1.183	0.821	1.080
3	1.898	1.740	1.892	1.890
4	7.606	7.383	7.523	7.244

Table 3: RMSE for Wannier band interpolation w.r.t. a DFT reference for spin-polarized calculations of GaAs using different gradient-norm cut-offs for converging the spread functional $\Omega[\{U^{\mathbf{k}}\}]$. Values are displayed for the 6 highest SO-split valence bands (band pairs 1-3) and the lowest 2 conduction bands (band pair 4).

it takes ≈ 24 times more iterations to converge the spread functional to a gradient-norm cut-off of $10^{-6}\ a_0^2$, compared to the spin-unpolarized run. This considerable increase in run-time and iterations might necessitate a more efficient optimizer for high-throughput calculations with strict cut-offs. However, such a strict convergence criterion may not be necessary for achieving a good energy interpolation accuracy, as will be discussed in the next paragraphs.

In panel a) of Fig. 5, the norm of the spread functional gradient G at different iterations is displayed. Gradient-norms initially decrease similarly rapidly in both runs, but diverge after ≈ 300 iterations (see panel c). The spin-unpolarized gradient continues to decay rapidly until the cut-off is met. On the other hand, the decrease of the spin-polarized gradient-norm quickly slows down, and it starts oscillating. The envelope of these oscillations seems to reach a plateau, where the gradient takes values between just above $10^{-6}\,a_0^2$ and $10^{-3}\,a_0^2$ for a large number of iterations. Nonetheless, the envelope slowly decreases overall, such that the target gradient cut-off is reached after 16 692 iterations, yielding a spread functional value of $\Omega_{10^{-6}a_0^2} = 131.118593\,a_0^2$.

Relaxing the convergence criterion on the norm of the gradient of Ω allows for reaching the convergence cut-off significantly faster, as can be seen in panels a) and c). A cut-off of $5 \cdot 10^{-6}\,a_0^2$ is first reached after 2859 iterations, while a cut-off of $10^{-5}\,a_0^2$ is met after 1040 iterations already. Choosing the latter yields a spread $\Omega_{10^{-5}a_0^2} = 131.118636\,a_0^2$, which has an absolute difference of only $\Delta_\Omega = 4.3 \cdot 10^{-5}\ a_0^2$ compared to the spread functional value obtained with the strict cut-off. At the same time, the increase in run-time for the spread-minimization is reduced to a factor of ≈ 6.4, compared to the spin-unpolarized run. Panel b) shows that the relative change of the spread functional w.r.t. the minimum value at the strict cut-off is below 10^{-6} after only 79 iterations. A Wannier interpolation with the relaxed cut-off of $10^{-5}\,a_0^2$ yields the interpolation RMSE per band values displayed in Tab. 3. All RMSEs per band with the relaxed cut-off are essentially identical to the values for a cut-off of $10^{-6}\ a_0^2$. A lower cut-off might thus be considered sufficient for a computationally efficient construction of spinor MLWFs, without a sacrifice in energy-interpolation accuracy, exemplified for GaAs.

4.1.3 Analysis of real-space Hamiltonian

The Wannier interpolation scheme yields accurate interpolated energies only if the real-space Hamiltonian matrix elements $H^{\mathbf{R}}_{mn} = \langle m\mathbf{0} \,|\, \hat{h} \,|\, n\mathbf{R}\rangle^{\mathrm{SC}}$ decay sufficiently fast with increasingly large $\mathbf{R}$ (compare Sec. 2.2.7). An approximation of the infinite sum over $\mathbf{R}$ in Eq. (2.2.31) by a finite sum over SC lattice vectors $\mathbf{R}$ is valid only if this condition is met. To quantitatively compare this decay between spin-polarized and spin-unpolarized MLWFs, the Frobenius norm of the real space Hamiltonian $||H^{\mathbf{R}}||_F$ is analyzed as a function of the norm of lattice vectors $|\mathbf{R}|$, fitting a power law to the data. The SC size is fixed by the $12 \times 12 \times 12$ $\mathbf{k}$-sampling during the first-principles DFT calculation. Fits and data are shown in Fig. 6. While the spin-polarized real-space

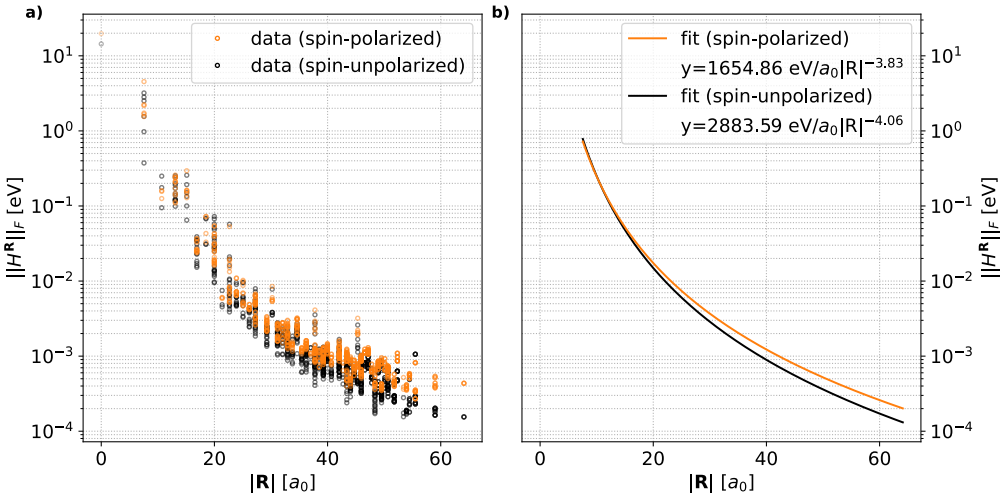

Figure 6: Decay of the real space Hamiltonian matrix, for spin-polarized and spin-unpolarized MLWFs in GaAs Panel a) shows the Frobenius norm $||\langle m\mathbf{0}\,|\,\hat{h}\,|\,n\mathbf{R}\rangle^{\mathrm{SC}}||_F$ as a function of lattice-vector norms $|\mathbf{R}|$ on a log-linear scale. Data points correspond to the spin-polarized (black) and spin-unpolarized (orange) matrix elements. Panel b) displays power-law fits to the data, with exponents $p_{\mathrm{spin}} = -3.83$ and $p_{\mathrm{no\text{-}spin}} = -4.06$.

Hamiltonian decays slightly slower, the overall decay is very similar for both calculations, with the matrix elements decaying to values below 0.5meV for the largest lattice vectors included. This value lies below the interpolation RMSEs per band (see previous sections), indicating that the sum-truncation is not the primary source of interpolation error. The exponents from power-law fits are also very similar ($p_{\mathrm{spin}} = -3.83$ vs. $p_{\mathrm{no\text{-}spin}} = -4.06$). Consequently, for bulk GaAs, the computation of spinor MLWFs does not require an increase in **k**-point density compared to the spin-unpolarized case to achieve comparable interpolation accuracies.

4.1.4 Wannier function shape

For further evaluating the spinor MLWF adaptation, iso-surface plots of the non-collinear spinor MLWFs' square modulus for the valence bands in the inner window from spin-polarized and spin-unpolarized results are compared in Fig. 7. For all plots, a common iso-value is chosen. In the first case, the six valence states share a spread of $\Omega \approx 8.704$, compared to an equivalent spread of $\Omega = 8.712$ for the three valence states in the second case.

The valence states centered on As atoms exhibit p-character. From visual inspection, no differences in shape are apparent, except for the direction of orbitals (which is somewhat arbitrary but related by symmetry operations). In GaAs, SO coupling has a strong effect mostly around the Γ point, while at other points throughout the BZ, the band dispersion remains largely unaffected. Consequently, the differences in the shapes of the WFs introduced through the consideration of SO coupling are small.

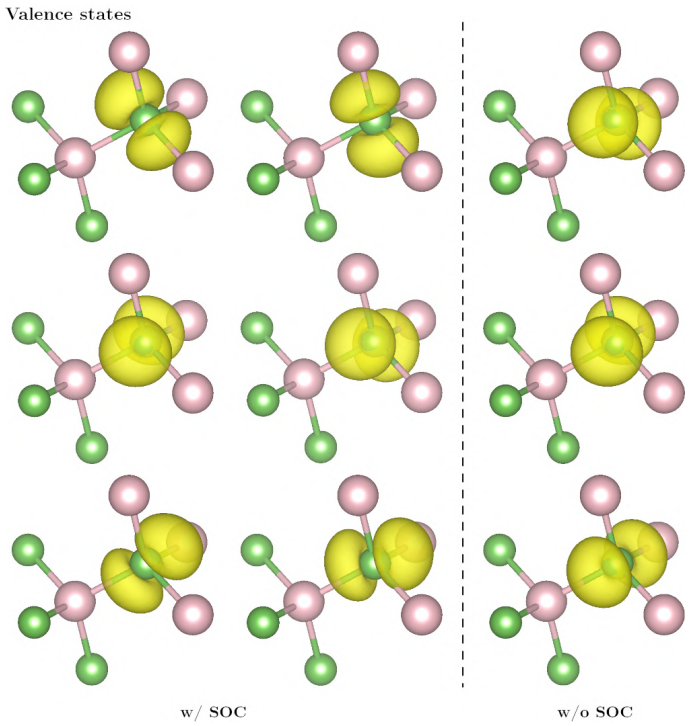

Figure 7: Square modulus of a MLWF (yellow) corresponding to the 6 (3) highest valence states for bulk GaAs considering (not considering) SO coupling. As (Ga) atoms are depicted in green (pink).

4.2 Collinear ferromagnetic FeAl

FeAl is a material exhibiting high resistance to corrosion and to aggressive chemical compounds up to high temperatures [42]. This material contains two atoms per primitive unit cell and can reach a ferromagnetic phase in the ideal fully ordered B2 configuration [19]. Therefore, it provides a simple candidate for testing the construction of collinear spin-pure MLWFs and the corresponding MLWF-based spin-resolved calculation of quantities.

A DFT calculation is performed with a lattice constant of $a = 5.44\,a_0$ on an 8×8×8 Monkhorst–Pack $\mathbf{k}$-grid, with $R_{\mathrm{MT,min}} \cdot |\mathbf{G}+\mathbf{k}|_{\max} = 8.0$, corresponding to a planewave cut-off of $|G|_{\max} = 14.0\,a_0^{-1}$. A collinear ferromagnetic phase is realized by including an initial external magnetic field in the z-direction $B_z(\mathbf{r}) = -4.0$ a.u. and gradually switching it off by halving its magnitude in each iteration (compare Sec. 2.1.9). Exchange-correlation effects are modeled by the GGA PBEsol functional [23]. 40 unoccupied states are included in the FV step for expanding the SV states. The procedure from Sec. 3.2 is then used to create two sets of spin-pure MLWFs ($J^{\uparrow} = J^{\downarrow} = 35$) on top of the first-principles calculation. For each set, the full disentanglement method is employed, choosing an inner energy window of $E^{\mathrm{in}} = [-12.2, 29.9]$ eV, including a total number of six fully occupied and a high number of 40 partly occupied or empty bands. The outer window $E^{\mathrm{out}} = [-12.2, 76.2]$ eV includes the highest unoccupied state considered in the first-principles calculation.

4.2.1 Convergence of the spread functional

The spread-functional optimization is again considered converged when the gradient norm reaches a cut-off of $10^{-6}\,a_0^2$, which is achieved after 6381 (6260) iterations for the spin-up (spin-down) set. For comparison, $J = 35$ MLWFs are calculated for the same windows based on an equivalent spin-unpolarized DFT calculation. In this run, the spread functional is converged to the same cut-off after 10 575 iterations, which means a factor of ≈ 1.7 more compared to both collinear spin-polarized calculations. Evidently, a collinear spin-pure MLWF calculation does not require a similar

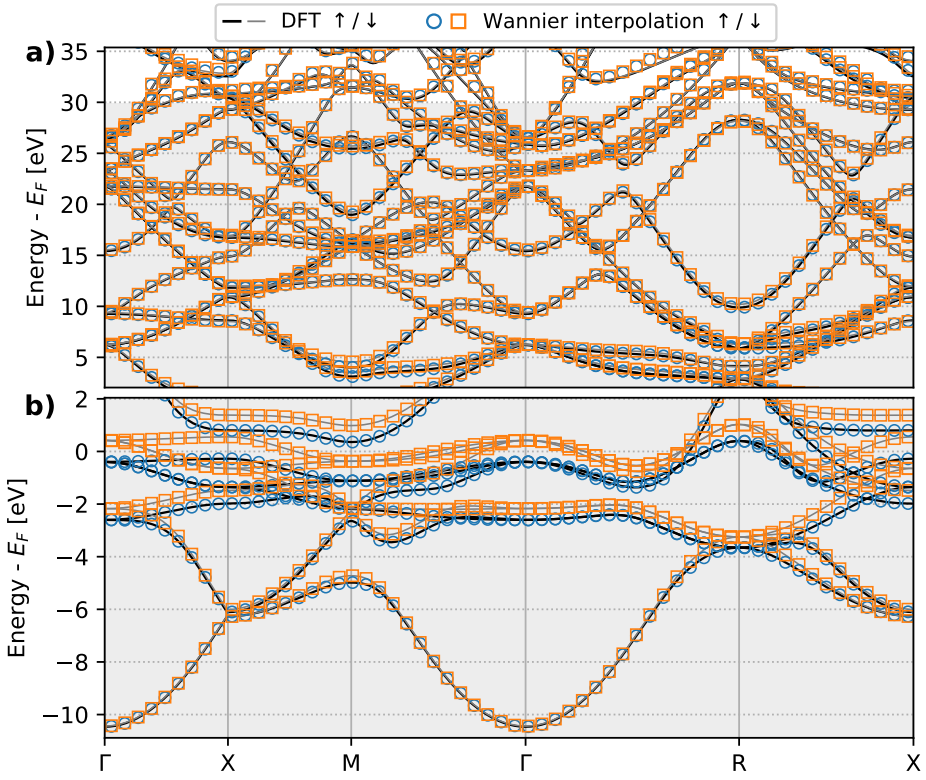

Figure 8: Band structure of collinear ferromagnetic FeAl in the B2 structure, comparing a DFT calculation with Wannier interpolation. Spin-up (Spin-down) bands are displayed as black (gray) lines. Wannier interpolated spin-up (spin-down) bands are shown as blue circles (orange squares). The plot range covers the inner energy window (gray area) while the full outer window is not displayed. Panel a) displays bands at higher energies, while panel b) shows the region around the Fermi level.

increase in the number of iterations as the non-collinear calculation for GaAs, presumably since the decoupling of the spin components simplifies the underlying manifold complexity considerably. Instead, the construction of spin-polarized MLWFs in FeAl exhibits a faster convergence of the spread functional than the spin-unpolarized run. However, for spin-unpolarized FeAl, the increase in the number of iterations for reaching convergence is far smaller than the factor of ≈ 22 observed for GaAs including SO coupling. In spin-unpolarized FeAl, the convergence might have been unfavorable.

4.2.2 Spin-resolved band interpolation

With the two constructed spin-pure sets of MLWFs, a spin-resolved band structure is interpolated and compared to a DFT reference in Fig. 8, in each case with the same band path sampling, and based on the first-principles DFT calculation on a coarse $8 \times 8 \times 8$ $\mathbf{k}$-grid above. Visually, Wannier bands closely match DFT bands throughout the inner energy window. The spin-splitting of bands is successfully captured, particularly visible near the Fermi level. The spin-down bands are shifted up with a different energy at each $\mathbf{q}$, compared to the spin-up bands. At higher energies, the spin-splitting appears to be less pronounced. For a quantitative evaluation of the interpolation, the RMSE values per band (Eq. (4.1.1)) are again calculated for both spin channels, with a band path sampling of 600 points $\mathbf{q}$. Interpolated band energies $\widetilde{\epsilon}^{\sigma}_{i\mathbf{q}}$ of band i are only included in the RMSE calculation when they are inside the inner energy window at $\mathbf{q}$. The results are displayed in Tab. 9. For both spins, bands 1-16 (counting from the lowest valence band in Fig. 8) are fully contained within E^{in} throughout the band-path, while higher bands are outside the inner window at some $\mathbf{q}$. The RMSE values of the former are in the range of $\approx 1.3 - 12.1\,\text{meV}$ and

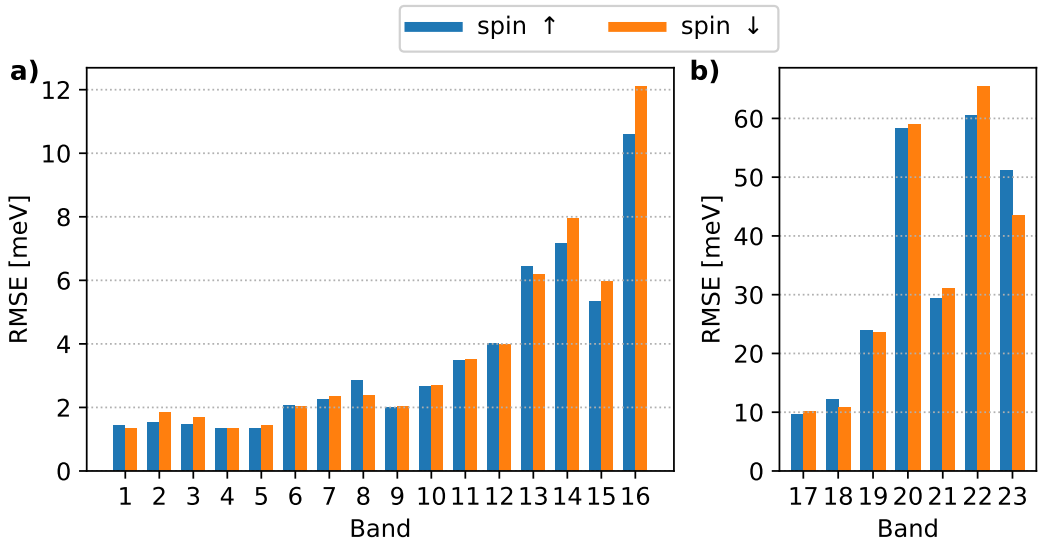

Figure 9: RMSE per band for a spin-resolved Wannier band interpolation for collinear ferromagnetic FeAl, with DFT band energies as a reference. Panel a) shows RMSEs for Bands fully contained within the inner energy window (1-16). Panel b) shows RMSEs for Bands outside of the inner window at some points in the BZ (17-23).

thus comparable to the values obtained for GaAs. No substantial difference between the spin-up and down group is noticeable. The interpolation errors increase towards the edge of the inner energy window, and bands mostly outside it, quickly exhibit larger RMSE values $> 10\,\text{meV}$. In conclusion, for FeAl, the extended spin-polarized Wannier implementation in `exciting` successfully provides access to accurate spin-resolved band structures via a Wannier interpolation with collinear spin-pure MLWFs.

4.2.3 Spin-resolved DOS, PDOS, and band characters from MLWFs

In addition to the band structure, the total DOS, orbital l-channel resolved PDOS (Eq. (3.4.11)), and orbital l-channel resolved band-characters (Eq. (3.4.9)) are calculated. Each quantity is obtained spin-resolved from the respective set of MLWFs. The PDOS and band characters are calculated atom-resolved, while the total DOS is calculated over both atoms. For the calculation of the DOS and PDOS, a dense interpolation grid of $50 \times 50 \times 50$ points $\mathbf{q}$ is considered. The corresponding results for the iron and aluminium atoms are displayed in Figs. 10 and 11, respectively. The total DOS of the two spin channels appears very similar in shape, but with energy shifted with respect to each other. The flat iron-derived bands in the range of ± 5 eV around the Fermi level exhibit strong d-orbital character in both spin channels and provide the by far largest contribution to the total DOS in this range. An asymmetry between the up and down contributions is visible. Going to higher energies, the d-channels become less dominant, such that contributions from p- and f-states are noticeable in the PDOS and the band-character plots. At higher energies, these empty bands contain equal contributions from Al d- and p-states compared to Fe. The different orbital contributions from MTs associated with Al atoms also exhibit some spin asymmetry, noticeably around the Fermi level. d- and p-channels dominate throughout the whole energy window in the aluminium PDOS, but rarely exceed the iron contributions. The lowest valence bands within the considered energy window show a parabolic dispersion around the Γ point, being dominated by s-orbital character from both atomic species for both spin channels. We conclude that for the collinear ferromagnetic configuration, spin-pure Wannier interpolation proves a useful tool for the spin-resolved analysis of band characters and densities of states.

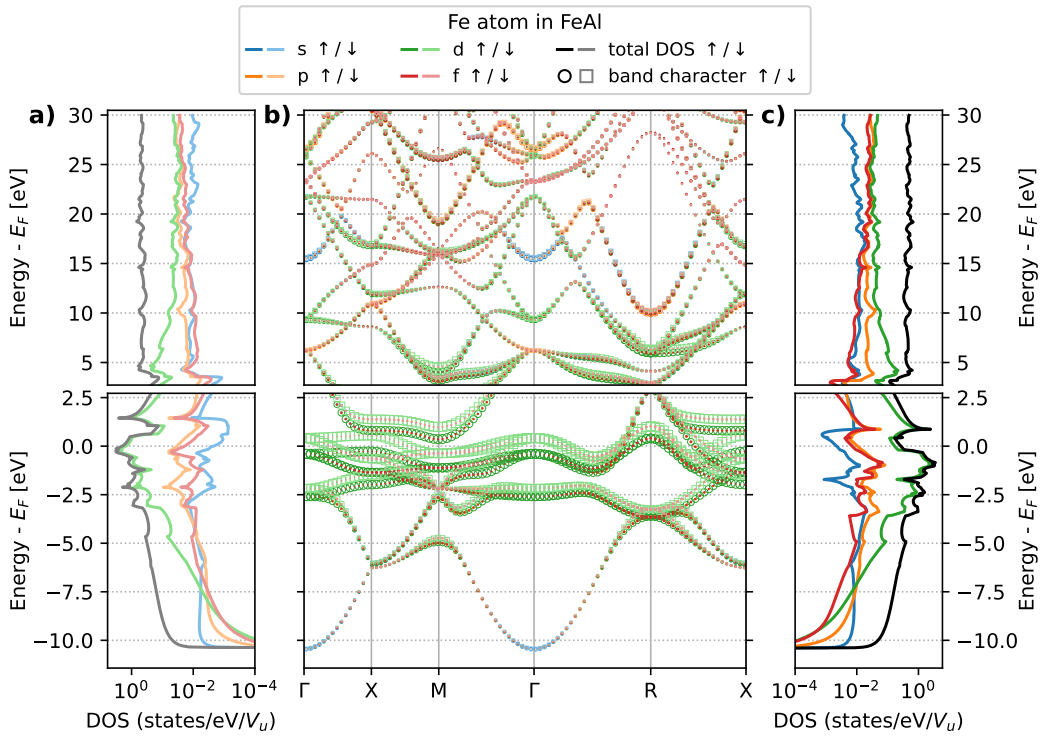

Figure 10: Band-structure of collinear ferromagnetic FeAl (middle panels). The l-resolved band character for the Fe atom, obtained from Wannier interpolation for spin-up (down) electrons is shown by circles (squares), which is proportional to the marker's size. Colors encode orbital l-channels. Corresponding total DOS (over both atoms) and l-resolved PDOS (a, c) for the spin-down and up directions, respectively. The PDOS is shown for the Fe atom contribution. The top panels present the high energy range, while the lower panels magnify the area around the Fermi level.

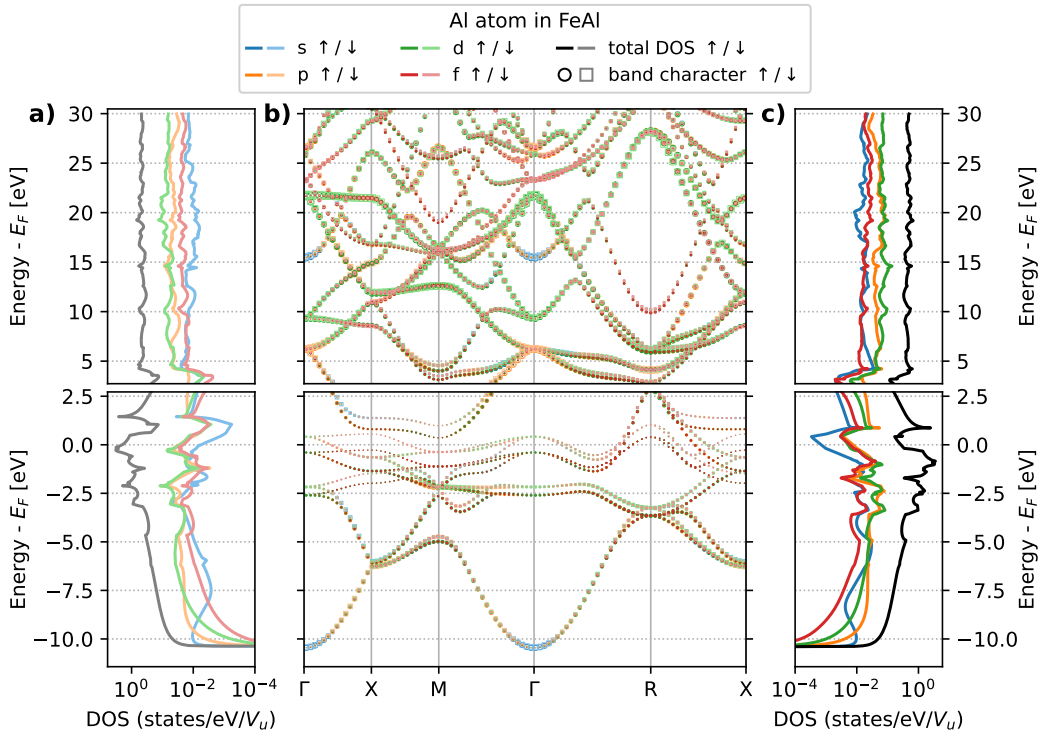

Figure 11: Same as Fig. 10 but for the Al atom.

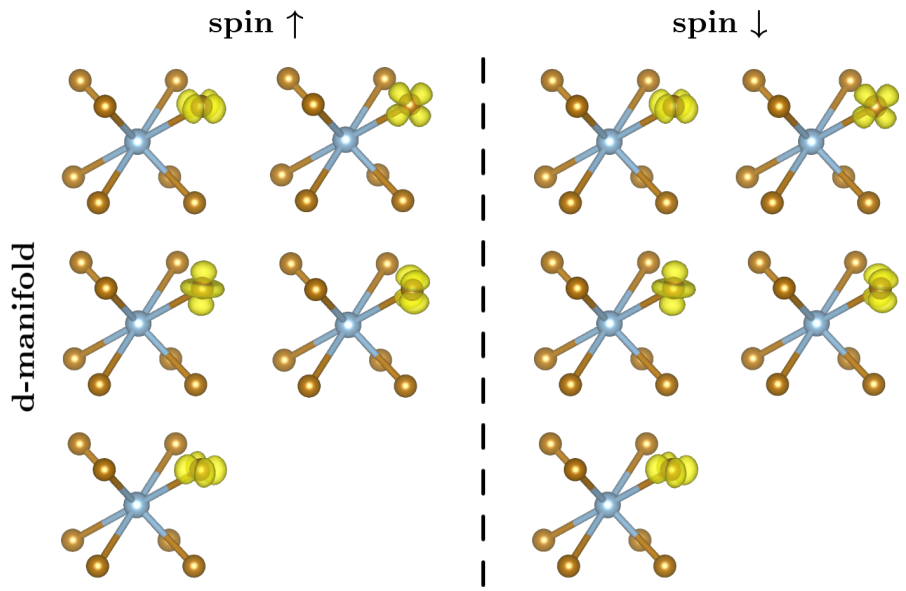

Figure 12: Collinear ferromagnetic FeAl: d-character spin ↑/↓ MLWF square modulus (yellow). Al (Fe) atoms are displayed in blue (brown).

4.2.4 Wannier function shape

In order to further compare the two spin channels, iso-plots of the spin-pure MLWFs are generated. In Fig. 12, the d-manifold states with energies around the Fermi level and centered on iron atoms are shown, with a common iso-value choice. These 5 MLWFs per spin channel all share a common spread of $\Omega \approx 1.0$ (rounded to 1 decimal), which is the lowest in each respective spin group, in accordance with the narrowness of d-bands (compare Fig. 10). In each spin channel, the complete un-hybridized d-manifold is found, with no visual difference between spin-up/down MLWFs.

4.3 Model CsPbI-based halide perovskite

Halide perovskites (HaP), particularly hybrid organic-inorganic candidates, have attracted research interest as they are a cost-efficient option for high-performance photovoltaic applications [32]. 2D HaPs are more stable compared to their 3D counterparts [29]. As HaPs contain heavy elements, e.g., I and Pb, their electronic structure is strongly impacted by SO coupling. There is significant structural diversity in HaPs, and many of them also lack inversion symmetry [39]. When both broken inversion symmetry and strong SO coupling are present, Rashba and/or Dresselhaus effects [5, 10] induce a pronounced SO splitting around the band gap. The Dresselhaus effect is associated with bulk inversion asymmetry, while the Rashba effect is related to structure inversion asymmetry. A recent publication [39] studied the origin of Rashba and Dresselhaus effects in model 2D and 3D HaPs composed of Cs, Pb, and I. For modeling a lattice distortion, the Pb atoms were displaced in different directions in order to break the inversion symmetry of the crystal. The strength of the Rashba/Dresselhaus-induced spin-splitting at the band gap is analyzed at different displacements of the Pb atoms [39]. In this work, it shall be demonstrated that spinor MLWFs are a useful tool in the analysis of band structures and spin-splitting energies for materials affected by Rashba and/or Dresselhaus effects. As a model system with few atoms per unit cell, bulk $CsPbI_3$ with a Pb displacement is considered.

The structure is set up with a primitive cubic lattice and a lattice constant of $a = 11.91\,a_0$ as described in [39]. Subsequently, the Pb atom is displaced in the diagonal in-plane direction [110], w.r.t. to the Pb-I bonds, breaking both bulk- and structure-inversion symmetry. For inducing a significant Rashba/Dresselhaus-splitting, a displacement of $0.43\,\text{Å} = 0.81\,a_0$ is chosen. A DFT

calculation is performed on a $7 \times 7 \times 7$ Monkhorst–Pack $\mathbf{k}$-grid, using $R_{\mathrm{MT,min}} \cdot |\mathbf{G} + \mathbf{k}|_{\max} = 9.0$, corresponding to a planewave cut-off of $|G|_{\max} = 16.0\, a_0^{-1}$. Exchange-correlation effects are considered by the GGA PBEsol functional [23]. 1000 unoccupied states are included for the SV expansion. The calculation serves as a proof of concept and is thus not fully converged in the number of unoccupied states, w.r.t. the spin-splitting at the band gap.

Based on this calculation, spinor MLWFs are generated via the full disentanglement method with energy windows $E^{\mathrm{in}} = [-5.44, 5.44]\,\mathrm{eV}$, $E^{\mathrm{out}} = [-5.44, 13.61]\,\mathrm{eV}$ relative to the Fermi level. A gradient norm cut-off of $10^{-6}\, a_0^2$ is used as convergence criterion for the spread-functional minimization, which is achieved after 11 803 iterations. This supports the claim that a spinor character of Bloch states has a large impact on the convergence behavior when constructing spinor MLWFs.

4.3.1 Wannier band interpolation

The resulting spinor MLWFs are used to interpolate the band structure shown in Fig. 13, and compared to a DFT reference in panel b), in each case based on the first-principles DFT calculation on a coarse $7 \times 7 \times 7$ $\mathbf{k}$-grid above. The Rashba/Dresselhaus splitting of the lowest conduction bands is visible as shifted parabolas at the points A and $A_1 = T$. From panel b), it is apparent that the Wannier interpolated bands are in excellent agreement with the DFT reference, again. For this material, the DFT calculation of the band structure becomes expensive, as many LAPW+LO basis functions are considered (523 for GaAs vs. 1399 for $CsPbI_3$) and the FV basis for the SV step includes a considerable number of empty states (200 for GaAs vs. 1000 for $CsPbI_3$). MLWFs provide an efficient interpolation procedure in this case. Consequently, for this example, the band path sampling has been chosen much finer for the Wannier interpolation than for the DFT reference. For this reason, the Wannier functions are drawn as lines, and the DFT reference as gray circles.

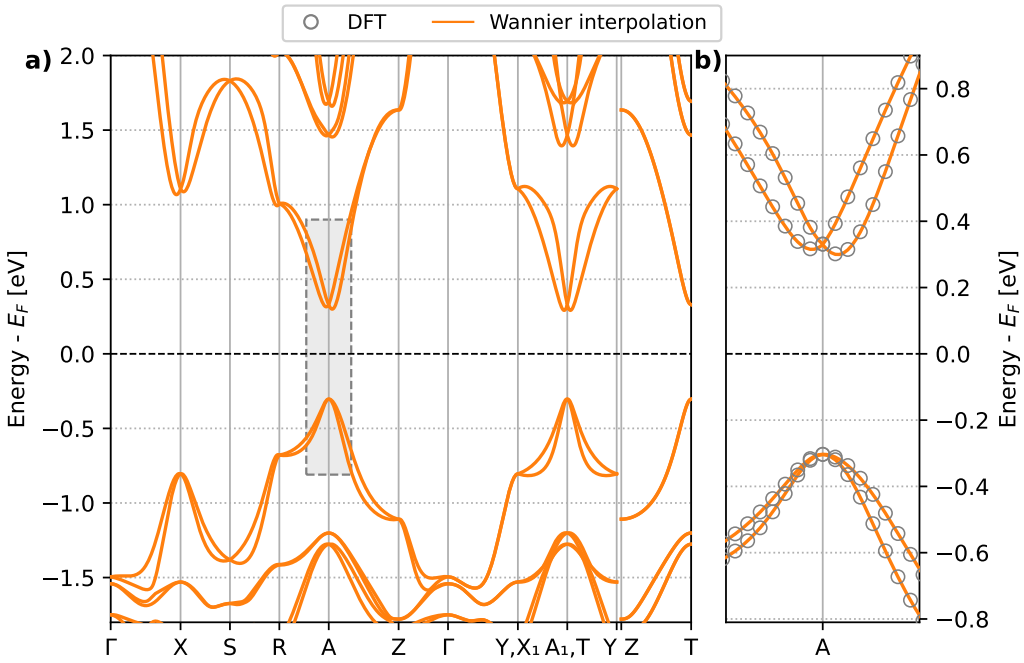

Figure 13: a) Wannier-interpolated band structure (orange) for bulk $CsPbI_3$ with displaced Pb considering SO coupling. Panel b) magnifies the area around the A-point (gray rectangle in panel a) and additionally displays DFT bands with a less dense band-path sampling (gray circles) for comparison.

4.3.2 Rashba/Dresselhaus spin-splitting and effective mass

MLWFs are a useful tool for determining the conduction band spin-splitting at the band gap. This splitting is defined at the conduction band minimum (CBm) location $\mathbf{q}_{\mathrm{CBm}}$ in reciprocal space as

$$\Delta E_{\mathrm{CBm}} = \widetilde{\epsilon}_{\mathrm{CBm}+1} - \widetilde{\epsilon}_{\mathrm{CBm}} \,. \tag{4.3.1}$$

Since the Rashba/Dresselhaus effects shift the conduction band minimum not only in energy but also in reciprocal space, the band gap is indirect. With the Wannier interpolation scheme, an analytical expression for band derivatives is available, and it is thus possible to retrieve the exact position of band extrema (see Sec. 3.4). This option was already implemented in the previous Wannier code [38]. Applying it to the $CsPbI_3$ spinor MLWFs, the CBm is obtained at $\mathbf{q}_{\mathrm{CBm}} = (0.264, -0.264, -0.248)\, a_0^{-1}$, which is close to the $A_1 = T$ point, along the high symmetry path segment $Y/X_1 \to A_1/T$. At the CBm, a spin-splitting of $\Delta E^{\mathrm{MLWF}}_{\mathbf{q}_{\mathrm{CBm}}} = 149.6\,\mathrm{meV}$ results. The spin-splitting energy is also calculated by simply finding the CBm along a band path sampling of 600 points $\mathbf{q}$. This way, a spin-splitting of $\Delta E^{\mathrm{path}}_{\mathbf{q}_{\mathrm{CBm}}} = 140.2\,\mathrm{meV}$ is obtained. The spin-splitting energy obtained by both methods is in agreement with each other, within the magnitude of interpolation RMSEs obtained in the previous applications. This implies that the CBm can be captured along high-symmetry directions for $CsPbI_3$ with displaced Pb. However, the optimization method employing analytical MLWF-based band derivatives does not rely on capturing the CBm along the band-path sampling. It might therefore prove superior when Rashba/Dresselhaus effects shift the CBm location away from high-symmetry directions [38].

At the retrieved CBm, the conduction band effective mass tensor can be calculated with MLWF-based analytical band derivatives (see Sec. 3.4), yielding

$$\mathbf{m}^*_{\mathrm{CBm}} = \begin{pmatrix} 0.878 & 0 & -0.0112 \\ 0 & 0.138 & 0 \\ 0.0112 & 0 & 0.107 \end{pmatrix} m_0 \,. \tag{4.3.2}$$

This effective mass tensor is dominated by diagonal terms. The off-diagonal components are < 2 orders of magnitude smaller. On the diagonal, the x-direction exhibits a high effective electron mass ($m_{xx} = 0.878\, m_0$) and thus a flat band dispersion, while the other two directions ($m_{yy} = 0.138\, m_0$, $m_{zz} = 0.107\, m_0$), show a similarly strong (though not equal) dispersion. Consequently, the electron transport becomes essentially 2-dimensional along the plane spanned by the two light-mass directions.

5 Discussion and outlook

This work has extended an existing implementation of Wannier functions in the full-potential LAPW+LO code `exciting` with respect to the spin degrees of freedom. With the extended implementation, MLWFs can be constructed either from collinear spin-pure or non-collinear spinor Bloch states. This work implemented the necessary changes that enable computationally cheap access to band structures, DOS, PDOS, and band characters with fine reciprocal space samplings, in terms of these spin-polarized MLWFs. In the collinear case, quantities can optionally be calculated spin-resolved with the spin-polarized Wannier implementation.

It could be shown for GaAs including SO coupling and collinear ferromagnetic FeAl, that eigenenergies can be Wannier-interpolated up to high accuracies of a few meV, with similar interpolation errors as with spin-unpolarized MLWFs. A band structure, DOS, and further the l-channel resolved PDOS and band-characters with fine reciprocal space samplings have successfully been calculated in collinear ferromagnetic FeAl, in each case spin-resolved.

When constructing spinor MLWFs for GaAs including SO coupling, the compute time per spread functional minimization iteration scaled with a factor of ≈ 4.4, which is slightly higher than the expected increase of 4 from the doubling of problem size alone ($\mathcal{O}(n^2)$). On the other hand, a considerably higher number of iterations ($\approx$ 24 fold increase) is required in order to reach the same strict gradient-norm cut-off of $10^{-6}\ a_0^2$, compared to the construction of spin-unpolarized MLWFs. A similar total number of iterations is required when constructing spinor MLWFs in bulk $CsPbI_3$ including SO coupling. The number of iterations remains comparable between the spin-polarized and spin-unpolarized runs for FeAl. However, in GaAs including SO coupling, a slightly relaxed cut-off of $10^{-5}\ a_0^2$ gives the same accuracy for the interpolation of band energies. This reduces the increase in necessary iterations to a factor of ≈ 1.5, compared to the spin-unpolarized case. The vicinity of the global minimum is still reached quickly, as the relative change of the spread functional w.r.t. the strict cut-off minimum value is below 10^{-6} after only 79 iterations. This indicates a flat manifold structure around the global minimum. Regarding the construction of spinor MLWFs, a systematic investigation of the (Marzari-Vanderbilt) spread functional convergence may be interesting.

A Wannier interpolation can only be accurate for a given SC size, if the real-space Hamiltonian matrix elements $H^{\mathbf{R}}$ expressed in MLWFs have decayed sufficiently for the largest lattice vectors $\mathbf{R}$ inside the SC. The SC size is fixed by the $\mathbf{k}$-grid sampling employed during the initial DFT calculation. For GaAs including SO coupling, these Hamiltonian matrix elements exhibit a slightly slower but otherwise similar decay with $|\mathbf{R}|$, compared to the spin-unpolarized case. A power-law fit to this decay yields exponents $p_{\text{spin}} = -3.83$ and $p_{\text{no-spin}} = -4.06$. Consequently, for the construction of spin-polarized MLWFs in GaAs, similar initial DFT $\mathbf{k}$-grid densities may be considered compared to the spin-unpolarized case, for achieving a comparable Wannier interpolation accuracy.

Spinor MLWFs prove a particularly useful tool for analyzing materials without inversion symmetry and strong with SO coupling. In such materials, the band extrema may be shifted away from high-symmetry directions and/or high-symmetry points due to Rashba/Dresselhaus effects. By employing spinor-MLWF-based analytical band derivatives, the CBm could reliably be found in bulk $CsPbI_3$ with displaced Pb atoms. Also, the effective mass tensor can easily be computed analytically at arbitrary points in reciprocal space, using the same MLWF-based band derivatives.

In the future, spin-polarized MLWFs constructed with the spinor-adapted Wannier implementation in `exciting` may be used to calculate physical effects and quantities that either require a spin-polarized treatment or change qualitatively when a spin-polarized treatment is employed.

Some of these calculations require a dense sampling in reciprocal space, whereas others involve expressions that are conveniently formulated in terms of WFs. For example, the spin-operator expectation value $\langle \hat{\mathbf{s}} \rangle$ (called spin texture [30]) could be Wannier interpolated onto arbitrary $\mathbf{q}$, potentially offering detailed insights on, e.g., the composition of Rashba/Dresselhaus effects in halide perovskites. The Wannier code `wannier90` [37] supplies an option for this calculation. The joint density of states offers insights into the availability of electronic transitions and observes different features when the electron spin is explicitly considered. Like the DOS and PDOS, it can be calculated from fine grids using Wannier functions. Further, the anomalous Hall conductivity [21] or spin Hall conductivity [33] can be expressed by the Berry curvature and Berry connection, which in turn have convenient expressions in terms of WFs [27]. Spinor MLWFs have previously also been used for calculating the orbital magnetization of periodic insulators [20]. By employing a spin-resolved analysis based on collinear spin-pure MLWFs, the mechanisms of ferroelectric effects have been investigated in multiferroic perovskites in the past [24]. They were further a useful tool for investigating the different insulating magnetic behavior of $La_4Ba_2Cu_2O_{10}$ and $Nd_4Ba_2Cu_2O_{10}$ in [18].

As an alternative disentanglement procedure for the construction of spin-polarized MLWFs, a SMV disentanglement with a consecutive S_z matrix diagonalization in the disentangled subspace was conducted in [21]. Wang et al. applied this disentanglement to ferromagnetic iron including SO coupling. They obtained a set of "almost spin-pure" MLWFs, even though the Bloch states are technically non-collinear spinors in this case. In the future, this method could allow a quasi-spin-resolved MLWF-based analysis of materials exhibiting very weak SO coupling. The same method could be applied to the construction of (almost) spin-pure MLWFs from exactly spin-pure collinear Bloch states. It might find a lower overall Ω_I than the fully separate energy disentanglement in the spin-up/-down subspace implemented in this work. In this case, a higher Wannier interpolation accuracy may be achieved when starting from lower first-principles $\mathbf{k}$-grid densities.

Within the scope of this work, spin-polarized MLWFs were constructed from Bloch states that result from a SV calculation in the DFT framework. For many materials, the SV Bloch states need to be expanded with a large number of FV states to obtain converged calculations. In [41], a more computationally efficient extension of the SV method was suggested, adding a number LOs explicitly to the basis for the SV step, in combination with a lower required number of FV states compared to the conventional SV method. With this *second variation with local orbitals* (SVLO) approach, which is also implemented in `exciting`, the flexibility of the basis is increased, particularly close to atom sites where SO coupling has a strong influence. Therefore, the basis size can be decreased, in addition to significantly lowering the computational cost for DFT calculations including SO coupling [41]. The spin-polarized Wannier implementation featured by this work would require minimal changes for the explicit incorporation of LOs into the SV step basis, for constructing spin-polarized MLWFs on top of a SVLO DFT calculation. The SV LO coefficients could easily be added to the SV to (FV) LAPW+LO basis expansion coefficients $\widetilde{D}^{\sigma\mathbf{k}}$. Such an incorporation would, however, require an extension of the spin-polarized automated MLWF initial guess construction, which was not covered within this work.

List of Abbreviations

BZ	first Brillouin zone
BvK	Born-von-Kármán
CBm	Conduction band minimum
DFT	Density-functional theory
DOS	Density of states
FV	First variation
HaP	Halide perovskites
HK	Hohenberg-Kohn
IR	Interstitial region
LAPW	Linearized augmented planewave
LO	Local orbital
LAPW+LO	Linearized augmented planewave + local orbital
MLWF	Maximally localized Wannier function
MT	Muffin tin (region)
PDOS	Partial density of states
PW	planewave (matrix)
SC	(BvK) Supercell
SCF	Self-consistent-field (cycle)
SMV	Souza Marzari Vanderbilt (disentanglement)
SO	Spin-orbit
SR	Scalar-relativistic
SV	Second variation
SVLO	Second variation with local orbitals
TB	Tight-binding
WF	Wannier function
ZORA	Zeroth-order regular approximation (to the Dirac Hamiltonian)

References

1. Born, M. & von Karman, T. Über Schwingungen im Raumgittern. German. *Physikalische Zeitschrift* **13,** 297–309 (1912).
2. Von Karman, T. & Born, M. Zur Theorie der spezifischen Wärme. German. *Physikalische Zeitschrift* **14.** On the theory of the specific heat, 15–19 (1913).
3. Wannier, G. H. The Structure of Electronic Excitation Levels in Insulating Crystals. *Physical Review* **52.** Publisher: American Physical Society, 191–197. https://link.aps.org/doi/10.1103/PhysRev.52.191 (2024) (Aug. 1937).
4. Slater, J. C. & Koster, G. F. Simplified LCAO Method for the Periodic Potential Problem. *Physical Review* **94.** Publisher: American Physical Society, 1498–1524. https://link.aps.org/doi/10.1103/PhysRev.94.1498 (2025) (June 15, 1954).
5. Dresselhaus, G. Spin-Orbit Coupling Effects in Zinc Blende Structures. *Physical Review* **100,** 580–586 (1955).
6. Blount, E. I. in *Solid State Physics* (eds Seitz, F. & Turnbull, D.) 305–373 (Academic Press, Jan. 1, 1962). https://www.sciencedirect.com/science/article/pii/S0081194708604592 (2025).

7. Hohenberg, P. & Kohn, W. Inhomogeneous Electron Gas. *Physical Review* **136.** Publisher: American Physical Society, B864–B871. https://link.aps.org/doi/10.1103/PhysRev.136.B864 (2025) (Nov. 9, 1964).
8. Kohn, W. & Sham, L. J. Self-Consistent Equations Including Exchange and Correlation Effects. *Physical Review* **140.** Publisher: American Physical Society, A1133–A1138. https://link.aps.org/doi/10.1103/PhysRev.140.A1133 (2025) (Nov. 15, 1965).
9. Monkhorst, H. J. & Pack, J. D. Special points for Brillouin-zone integrations. *Physical Review B* **13.** Publisher: American Physical Society, 5188–5192. https://link.aps.org/doi/10.1103/PhysRevB.13.5188 (2026) (June 15, 1976).
10. Bychkov, Y. A. & Rashba, E. I. Oscillatory effects and the magnetic susceptibility of carriers in inversion layers. *Journal of Physics C: Solid State Physics* **17,** 6039. https://doi.org/10.1088/0022-3719/17/33/015 (Nov. 1984).
11. Lenthe, E. v., Baerends, E. J. & Snijders, J. G. Relativistic regular two-component Hamiltonians. *The Journal of Chemical Physics* **99,** 4597–4610. ISSN: 0021-9606. https://doi.org/10.1063/1.466059 (2024) (Sept. 15, 1993).
12. Singh, D. J. *Planewaves, Pseudopotentials and the LAPW Method* ISBN: 978-1-4757-2312-0. http://link.springer.com/10.1007/978-1-4757-2312-0 (2023) (Springer US, Boston, MA, 1994).
13. Perdew, J. P., Burke, K. & Ernzerhof, M. Generalized Gradient Approximation Made Simple. *Physical Review Letters* **77.** Publisher: American Physical Society, 3865–3868. https://link.aps.org/doi/10.1103/PhysRevLett.77.3865 (2025) (Oct. 28, 1996).
14. Marzari, N. & Vanderbilt, D. Maximally localized generalized Wannier functions for composite energy bands. *Phys. Rev. B* **56,** 12847–12865. https://link.aps.org/doi/10.1103/PhysRevB.56.12847 (20 Nov. 1997).
15. Aryasetiawan, F. & Gunnarsson, O. The GW method. *Reports on Progress in Physics* **61,** 237. ISSN: 0034-4885. https://doi.org/10.1088/0034-4885/61/3/002 (2026) (Mar. 1998).
16. Perdew, J. P. & Schmidt, K. Jacob's ladder of density functional approximations for the exchange-correlation energy. *AIP Conference Proceedings* **577,** 1–20. ISSN: 0094-243X. https://doi.org/10.1063/1.1390175 (2025) (July 6, 2001).
17. Souza, I., Marzari, N. & Vanderbilt, D. Maximally localized Wannier functions for entangled energy bands. *Physical Review B* **65.** Publisher: American Physical Society, 035109. https://link.aps.org/doi/10.1103/PhysRevB.65.035109 (2023) (Dec. 19, 2001).
18. Ku, W., Rosner, H., Pickett, W. E. & Scalettar, R. T. Microscopic analysis of insulating magnetism of La4Ba2Cu2O10 and Nd4Ba2Cu2O10. *Journal of Solid State Chemistry. Proceedings from the 23rd Rare Earth Research Conference UC Davis Campus, July 13-16, 2002* **171,** 329–333. ISSN: 0022-4596. https://www.sciencedirect.com/science/article/pii/S0022459602002128 (2026) (Feb. 15, 2003).
19. Smirnov, A. V., Shelton, W. A. & Johnson, D. D. Importance of thermal disorder on the properties of alloys: Origin of paramagnetism and structural anomalies in bcc-based $Fe_{1-x}Al_x$. *Physical Review B* **71.** Publisher: American Physical Society, 064408. https://link.aps.org/doi/10.1103/PhysRevB.71.064408 (2026) (Feb. 18, 2005).
20. Thonhauser, T., Ceresoli, D., Vanderbilt, D. & Resta, R. Orbital Magnetization in Periodic Insulators. *Physical Review Letters* **95.** Publisher: American Physical Society, 137205. https://link.aps.org/doi/10.1103/PhysRevLett.95.137205 (2026) (Sept. 22, 2005).
21. Wang, X., Yates, J. R., Souza, I. & Vanderbilt, D. Ab initio calculation of the anomalous Hall conductivity by Wannier interpolation. *Physical Review B* **74.** Publisher: American Physical Society, 195118. https://link.aps.org/doi/10.1103/PhysRevB.74.195118 (2023) (Nov. 2006).

22. Yates, J. R., Wang, X., Vanderbilt, D. & Souza, I. Spectral and Fermi surface properties from Wannier interpolation. *Physical Review B* **75.** Publisher: American Physical Society, 195121. https://link.aps.org/doi/10.1103/PhysRevB.75.195121 (2024) (May 21, 2007).
23. Perdew, J. P. *et al.* Generalized gradient approximation for solids and their surfaces. *Physical Review Letters* **100,** 136406. ISSN: 0031-9007, 1079-7114. arXiv: 0707.2088[cond-mat]. http://arxiv.org/abs/0707.2088 (2026) (Apr. 4, 2008).
24. Picozzi, S. *et al.* Microscopic mechanisms for improper ferroelectricity in multiferroic perovskites: a theoretical review. *Journal of Physics: Condensed Matter* **20,** 434208. ISSN: 0953-8984. https://doi.org/10.1088/0953-8984/20/43/434208 (2026) (Oct. 2008).
25. Engel, E. & Dreizler, R. M. *Density Functional Theory: An Advanced Course* ISBN: 978-3-642-14090-7. http://link.springer.com/10.1007/978-3-642-14090-7 (2026) (Springer, Berlin, Heidelberg, 2011).
26. Jacob, C. R. & Reiher, M. Spin in density-functional theory. *International Journal of Quantum Chemistry* **112,** 3661–3684. ISSN: 0020-7608, 1097-461X. https://onlinelibrary.wiley.com/doi/10.1002/qua.24309 (2025) (Dec. 5, 2012).
27. Marzari, N., Mostofi, A. A., Yates, J. R., Souza, I. & Vanderbilt, D. Maximally localized Wannier functions: Theory and applications. *Reviews of Modern Physics* **84,** 1419–1475. ISSN: 0034-6861, 1539-0756. arXiv: 1112.5411[cond-mat]. http://arxiv.org/abs/1112.5411 (2024) (Oct. 10, 2012).
28. Gulans, A. *et al.* exciting: a full-potential all-electron package implementing density-functional theory and many-body perturbation theory. *Journal of Physics: Condensed Matter* **26,** 363202. https://dx.doi.org/10.1088/0953-8984/26/36/363202 (Aug. 2014).
29. Smith, I. C., Hoke, E. T., Solis-Ibarra, D., McGehee, M. D. & Karunadasa, H. I. A Layered Hybrid Perovskite Solar-Cell Absorber with Enhanced Moisture Stability. *Angewandte Chemie International Edition* **53.** _eprint: https://onlinelibrary.wiley.com/doi/pdf/10.1002/anie.201406466, 11232–11235. ISSN: 1521-3773. https://onlinelibrary.wiley.com/doi/abs/10.1002/anie.201406466 (2026) (2014).
30. Manchon, A., Koo, H. C., Nitta, J., Frolov, S. M. & Duine, R. A. New perspectives for Rashba spin–orbit coupling. *Nature Materials* **14.** Publisher: Nature Publishing Group, 871–882. ISSN: 1476-4660. https://www.nature.com/articles/nmat4360 (2026) (Sept. 2015).
31. Mustafa, J. I., Coh, S., Cohen, M. L. & Louie, S. G. Automated construction of maximally localized Wannier functions: Optimized projection functions method. *Physical Review B* **92.** Publisher: American Physical Society, 165134. https://link.aps.org/doi/10.1103/PhysRevB.92.165134 (2025) (Oct. 30, 2015).
32. Brenner, T. M., Egger, D. A., Kronik, L., Hodes, G. & Cahen, D. Hybrid organic—inorganic perovskites: low-cost semiconductors with intriguing charge-transport properties. *Nature Reviews Materials* **1.** Publisher: Nature Publishing Group, 15007. ISSN: 2058-8437. https://www.nature.com/articles/natrevmats20157 (2026) (Jan. 11, 2016).
33. Qiao, J., Zhou, J., Yuan, Z. & Zhao, W. Calculation of intrinsic spin Hall conductivity by Wannier interpolation. *Physical Review B* **98.** Publisher: American Physical Society, 214402. https://link.aps.org/doi/10.1103/PhysRevB.98.214402 (2026) (Dec. 3, 2018).
34. Tillack, S. *Implementation and Application of Maximally Localized Wannier Functions within the (L)APW+lo Method* MA thesis (Humboldt-Universität zu Berlin, 2018).
35. Damle, A., Levitt, A. & Lin, L. Variational Formulation for Wannier Functions with Entangled Band Structure. *Multiscale Modeling & Simulation* **17.** Publisher: Society for Industrial and Applied Mathematics, 167–191. ISSN: 1540-3459. https://epubs.siam.org/doi/abs/10.1137/18M1167164 (2024) (Jan. 2019).
36. Girvin, S. M. & Yang, K. *Modern Condensed Matter Physics* en. ISBN: 9781316480649 Publisher: Cambridge University Press. https://www.cambridge.org/highereducation/

books/modern-condensed-matter-physics/F0A27AC5DEA8A40EA6EA5D727ED8B14E (2025) (Cambridge University Press, Feb. 2019).

37. Pizzi, G. *et al.* Wannier90 as a community code: new features and applications. *Journal of Physics: Condensed Matter* **32,** 165902. https://doi.org/10.1088/1361-648X/ab51ff (Jan. 2020).
38. Tillack, S., Gulans, A. & Draxl, C. Maximally localized Wannier functions within the (L)APW+LO method. *Physical Review B* **101.** Publisher: American Physical Society, 235102. https://link.aps.org/doi/10.1103/PhysRevB.101.235102 (2023) (June 1, 2020).
39. Maurer, B., Vorwerk, C. & Draxl, C. Rashba and Dresselhaus effects in two-dimensional Pb-I-based perovskites. *Physical Review B* **105.** Publisher: American Physical Society, 155149. https://link.aps.org/doi/10.1103/PhysRevB.105.155149 (2025) (Apr. 22, 2022).
40. Pu, Z. *et al.* Noncollinear density functional theory. *Physical Review Research* **5.** Publisher: American Physical Society, 013036. https://link.aps.org/doi/10.1103/PhysRevResearch.5.013036 (2026) (Jan. 24, 2023).
41. Vona, C., Lubeck, S., Kleine, H., Gulans, A. & Draxl, C. Accurate and efficient treatment of spin-orbit coupling via second variation employing local orbitals. *Physical Review B* **108.** Publisher: American Physical Society, 235161. https://link.aps.org/doi/10.1103/PhysRevB.108.235161 (2024) (Dec. 20, 2023).
42. Kauffmann, A. *IAM - Werkstoffkunde Forschung - Physical Metallurgy - Materials Development - B2 FeAl* Archive Location: KIT Publisher: Alexander Kauffmann. https://www.iam.kit.edu/wk/3164.php (2026).
43. Tillack, S. & Draxl, C. Automatic Generation of Maximally Localized Wannier Functions via Optimized Projection Functions and Self-projections. arXiv.org. https://arxiv.org/abs/2502.03213v2 (2026) (Feb. 5, 2025).
44. Raya-Moreno, M. *et al. An exciting approach to theoretical spectroscopy* Feb. 9, 2026. arXiv: 2601.11388[cond-mat]. http://arxiv.org/abs/2601.11388 (2026).

Selbstständigkeitserklärung

Ich erkläre hiermit, dass ich die vorliegende Arbeit selbstständig verfasst und noch nicht für andere Prüfungen eingereicht habe. Sämtliche Quellen einschließlich Internetquellen, die unverändert oder abgewandelt wiedergegeben werden, insbesondere Quellen für Texte, Grafiken, Tabellen, Bilder sowie die Nutzung von Künstlicher Intelligenz für die Erstellung von Texten und Abbildungen, sind als solche kenntlich gemacht. Mir ist bekannt, dass bei Verstößen gegen diese Grundsätze ein Verfahren wegen Täuschungsversuchs bzw. Täuschung eingeleitet wird.

Berlin, 17.03.2026